UNIVERSITÉ DE SHERBROOKE

Faculté de génie

Département de génie civil

NUMERICAL SIMULATION OF SHEET METAL FORMING PROCESSES AND LOCALIZED DEFORMATION PHENOMENA FOR FCC POLYCRYSTALS

SIMULATION NUMÉRIQUE DE LA MISE EN FORME DES MÉTAUX ET LES PHÉNOMÈNES DE LOCALISATION POUR LES POLYCRISTAUX CFC

Thèse de doctorat

Spécialité : génie civil

Kaan A. INAL

Sherbrooke (Québec) Canada

Décembre 2001

Acknowledgements

I would like to express my deepest appreciation to my supervisor Professor Kenneth W. Neale and my co-supervisor Dr. Peidong Wu who both introduced me to the exciting area of solid mechanics and crystal plasticity. This thesis could not have been completed without their guidance, invaluable advice, helpful discussions and constant encouragement. I am also most grateful to Dr. Neale for his help in making my settling in Canada a reality.

This thesis was conducted as part of a collaborative research program with Dr. Stuart MacEwen's group of Alcan International's Kingston Research and Development Centre. The scientific input of Dr. MacEwen and his colleagues has been extremely valuable, and I am grateful for the many stimulating discussions that we have had during the coarse of this research.

I am deeply grateful to my uncle Pirol Tugcu for the constant support and encouragement that he has given me not only during my thesis but throughout my whole life. Special thanks go to Ms. Lise Dutrisac for the kindness and friendship that she has shown since my first day in Canada.

Many thanks go to all my colleagues and friends in the Department of Civil Engineering of the Université de Sherbrooke. Their encouragement, friendship and support during the period of my doctoral studies were extremely valuable to me.

I gratefully acknowledge the Natural Sciences and Engineering Research Council of Canada (NSERC) and the Alcan International Kingston Research and Development Centre for their financial support of this work.

Finally, I would like to express my profound and eternal gratitude to my beloved parents, my father Ayhan and my mother Yasar, and to my younger brother Gorkem, who made all my studies possible both morally and materially.

Abstract

In this thesis, finite element analyses based on a rate-dependent Taylor-type polycrystal model have been developed to simulate sheet metal forming processes and localized deformation phenomena. This formulation can be applied to nonhomogeneous boundary-value problems for FCC polycrystals subjected to large deformations. The analysis inherently accounts for initial textures as well as deformation-induced anisotropies due to texture evolution. Both plane strain and plane stress finite element (FE) codes incorporating parallel computing algorithms have been developed so that simulations could be performed for applications requiring fairly large numbers of elements.

Using the finite element codes which have been developed, instability and localization phenomena for the rolled aluminum sheet alloy AA3004-H19 under tension have been studied. The effects of various parameters on the formation of localized deformation bands have been investigated. These include initial texture and its evolution, strain hardening, material strain-rate sensitivity, loading direction, mesh sensitivity, geometric imperfections, and boundary conditions Instability criteria have been defined for both necking and shear banding.

The large strain behaviour of the rolled aluminum sheet alloy AA3004-H19 under planar simple shear has also been simulated numerically using both the plane strain and the plane stress polycrystal FE codes. The effects of the shearing direction on the overall shear stress–shear deformation curves and deformation patterns have been investigated. The initiation and propagation of shear bands have been studied in detail.

Finally, the plane strain FE code was employed to simulate earing during the deep drawing of the rolled aluminum sheet alloys AA6111-T4 and AA5754-0. Simulations based on both the polycrystal model and a phenomenological constitutive law were performed where only the flange area of the sheet was analyzed. The effects of these textures were examined, and comparisons were made with experimental data.

Résumé

Une formulation par éléments finis pour les polycristaux, basée sur l'hypothèse de Taylor pour un matériau sensible au taux de déformation, a été appliquée pour analyser la mise en forme des métaux et les phénomènes de localisation. Cette formulation s'applique aux problèmes de conditions aux limites non homogènes des métaux polycristallins sous grandes déformations. Elle tient également compte des textures initiales ainsi que des anisotropies induites par la déformation causée par l'évolution de la texture. Des codes d'éléments finis basés sur les hypothèses de déformations planes et de contraintes planes incorporant des algorithmes de calcul parallèle ont été élaborés.

En utilisant les codes d'éléments finis établis, les instabilités et les phénomènes de localisation dans l'alliage d'aluminium AA3004-H19 sous tension ont alors été étudiés. Les effets de divers paramètres tels que la texture initiale et son évolution, l'écrouissage, la sensibilité au taux de déformation du matériau, la direction du chargement, la sensibilité du maillage, les imperfections géométriques et les conditions limites sur la formation des déformations locales ont été traités. Un critère d'instabilité a été défini pour la striction et la formation des bandes de cisaillement.

Le comportement à grandes déformations pour l'alliage d'aluminium AA3004-H19, sous cisaillement simple, a aussi été simulé numériquement en utilisant les codes d'éléments finis. Les effets des directions du cisaillement sur les courbes de contrainte–déformation et les morphologies des déformations ont été étudiés. L'initiation et la propagation des bandes de cisaillement ont aussi été examinées en détail.

Finalement, l'emboutissage profond des alliages d'aluminium AA6111-T4 et AA5754-0 a été modélisé en utilisant à la fois le modèle polycristallin et un modèle phénoménologique où seulement la zone de « flange » a été analysée. Les effets de ces textures ont été examinés et les résultats obtenus ont été comparés avec les données expérimentales.

Table of Contents

CHAPTER 1

INTRODUCTION

1.0 INTRODUCTION

Sheet metal forming has, for a long time, been one of the most common metal processing operations. In many manufacturing areas such as the automotive, aerospace, packaging and electronic industries, the optimization of sheet metal processes has become a key factor to reduce product development time and final cost. In general, sheet metal forming involves large strains due to stretching, drawing, bending or various combinations of these basic deformation modes. From the view point of mechanics, the analysis of sheet metal working involves nonlinearities in geometry, material and contact. In an effort to better understand sheet forming processes, various research works have been carried out using diverse technologies involving experimental, analytical and computational methods.

Accurate simulations of sheet metal forming operations requires a good understanding of the deformation mechanisms involved and the proper use of deformation models of metal forming. The common metals of industrial practice are polycrystalline aggregates which consist of single crystals or individual grains with lattice structures. The mechanical properties of a polycrystalline metal depend on many attributes of its microstructure; consequently, considerable efforts have been devoted to the study of micromechanics. These studies indicate that, among the factors which result in the plastic deformation of single crystals and polycrystals, crystallographic slip occurring by the migration across the slip planes of atomic defects, termed dislocations, is the dominant one.

Crystallographic slip induces lattice rotations which result in a non-random distribution of the crystal orientations in polycrystals. The textures developed during forming processes is a macroscopic average of such non-random orientations. Research indicates that texture occurs in many metal forming processes such as drawing, extrusion, rolling and sheet metal forming. These textures not only have profound effects on the mechanical and thermal properties of metals, but also have great influence on subsequent fabrication processes as well as on the quality of the products. Thus, it is obvious that accurate simulations of sheet metal forming should consider initial texture and its evolution, as well as the anisotropy induced by the evolution of microstructure and microscopic properties.

Essentially two classes of models have been developed for numerical simulations of sheet metal forming operations: phenomenological (macroscopic) models and polycrystal (microscopic) models. The theory of phenomenological plasticity is generally initiated from hypotheses and assumptions of a macroscopic character based on certain experimental observations. In the past, the constitutive laws that were used to model metal forming processes were almost exclusively phenomenological in nature. Although such phenomenological models are acceptable for many applications, they do not explicitly include the basic physics of plastic deformation. They are inherently incapable of predicting the effects of material microstructure and its evolution with deformation on metal performance, nor can they link mechanical properties to evolving microstructures and textures.

To model processes such as texture evolution and its influence on deformation-induced anisotropy, micromechanically based models of plastic behaviour are required. In particular, constitutive relations formulated on the concepts of crystal plasticity must be adopted. Since Taylor's pioneering work in 1938, the prediction of the deformation behaviour of polycrystalline solids from the response of their single crystal constituents has been the focus of many investigations. Thus, many crystal plasticity models have been proposed or modified to simulate the behaviour of polycrystalline metals during plastic deformation from the response of their single crystal constituents.

The mathematical modelling of material behaviour is a very effective way of reducing time and costs involved in optimizing manufacturing processes. Indeed, numerous complex forming operations have been simulated using numerical methods in order to predict critical parameters. Among these methods, the finite element method (FEM), has been widely applied to the study of metal forming because of its flexibility, accuracy and efficiency. Considering the rapid advancement of computer capabilities, the finite element method has become a powerful tool in modelling metal forming operations.

Up to the 1980's, most applications involving the finite element method have been based on phenomenological constitutive models since microscopic models involve significantly more demanding computations. However the introduction of parallel computers has rendered metal

forming modelling based on crystal plasticity feasible since they offer more computational power and storage than serial computer architectures. With proper parallelization techniques, realistic applications based on crystal plasticity can be performed on parallel computers such as the IBM SP3.

The objective of the present work is to develop crystal plasticity based finite element models to simulate sheet metal forming processes, and to investigate localized deformation phenomena in metals. A rate-sensitive Taylor-type polycrystal model is implemented in our nonlinear numerical analyses. Both plane strain and plane stress finite element codes based on a large-strain Lagrangian formulation have been developed. These codes incorporate parallel computing algorithms enabling simulations with realistic models. Various forming operations and localized deformation phenomena are simulated for rolled aluminum sheets.

In Chapter 2, the deformation characteristics of single crystals and polycrystals, which are the physical basis of the present work, are first presented and discussed. To date, many models of the plastic distortion of single crystals and extensions to polycrystals have been developed. For single crystals, the rate dependent and rate independent models are the two major models. In general, a polycrystal model can be derived from single crystal deformation models by the execution of an appropriate averaging scheme for combining single crystal properties into polycrystal behaviour. There are three classical theories concerning the transition from the micro-response of the individual grains to the macro-response of the polycrystalline aggregate: Taylor's theory, Sach's theory and the self-consistent theory. The Taylor polycrystal theory, on which the present research is based, is described in detail. Its advantages and drawbacks are discussed. In addition, more recent developments in crystal plasticity theory such as the so-called "finite element per single crystal (FESC)" model, strain gradient plasticity theory, models including backstress, and discrete dislocation plasticity theory are briefly presented.

The polycrystal deformation model and its implementation in the finite element code is described in Chapter 3. The rate-sensitive crystal plasticity formulation proposed by Asaro and Needleman (1985) is presented in detail. This model, in which the principal deformation mechanism is assumed to be rate dependent crystallographic slip, accounts for large

deformations, the rotation of crystal axes, and elastic anisotropy of the grains. In the second part of this chapter we present a finite element procedure based on a large-strain Lagrangian formulation of the field equations. Both plane strain and plane stress FE codes are developed and the rate-sensitive crystal plasticity model is implemented in these codes. The basic idea in this formulation is that a material point within the domain represents a polycrystal of N grains, and the constitutive response at the material point is given through the Taylor polycrystal model. Crystal plasticity based simulations entail extremely demanding computations since a significant amount of information at the grain level must be tracked. Thus, parallel computing algorithms are developed to distribute data at the grain level between the processors of a parallel computer. The last part of this chapter presents the parallel computing algorithms and their implementation in the FE codes.

As the first application, simulations of localized deformation in an aluminum sheet alloy (AA3004-H19) under tension are presented in Chapter 4. Simulations with both the plane strain and plane stress FE codes are presented. For the plane strain simulations, an initial imperfection is assumed to trigger localized deformation. However, no initial imperfections are considered for the plane stress simulations where localized deformation occurs as a result of the so-called "built-in" boundary conditions. The effects of texture evolution, slip rate sensitivity, strain hardening, mesh sensitivity, and the loading direction on the formation of localized deformations are discussed in detail. Onsetting criteria are defined for both necking and shear banding.

Since sheet metal forming operations involve large plastic strains, the proper understanding and characterization of the large strain behaviour of thin metal sheets is crucial for controlling product quality. In Chapter 5, the large strain behaviour of the aluminum sheet alloy AA3004-H19 under planar simple shear is investigated. Simulations with both plane strain and plane stress FE codes are presented. For comparison, results based on the Taylor-type polycrystalline model under the assumption of homogeneous simple shear are also included. Mesh sensitivity, and the sensitivity of the overall shear stress response and deformation distribution to the loading direction, are investigated. Furthermore, the initiation and propagation of shear bands are discussed in detail. The numerical results are compared with experimental data found in literature.

Chapter 6 is devoted to simulations of earing during the deep drawing of aluminum sheets. A simple flange model is presented where only the deformations in the flange area of the sheet are considered in the analysis. Simulations with the plane strain FE code are performed both with the polycrystal model and a phenomenological model (Barlat et al., 1991a,b) for the aluminum sheet alloys AA6111-T4 and AA5754-0. The effects of these textures are discussed, and the results are compared with experimental data.

Chapter 7 contains a brief summary and the general conclusions of this research. Future applications and developments to improve metal forming modelling are also discussed in this chapter.

CHAPTER 2

CRYSTAL PLASTICITY THEORY

2.1 Introduction

Metals are crystalline solids which consist of atoms arranged in a pattern that is repeated periodically in three dimensions. Such an atomic arrangement can be described completely by specifying atom positions in some repeating unit cell of the space lattice. Figure 2.1 illustrates the unit cells for three typical microstructures of metals: BCC (body-centred cubic), FCC (face-centred cubic) and HCP (hexagonal close-packed). Metals that crystallize in the FCC lattice are aluminum, copper, brass, nickel, gold, silver, lead, platinum and gamma (γ) iron. In the present research, the focus is on FCC crystals.

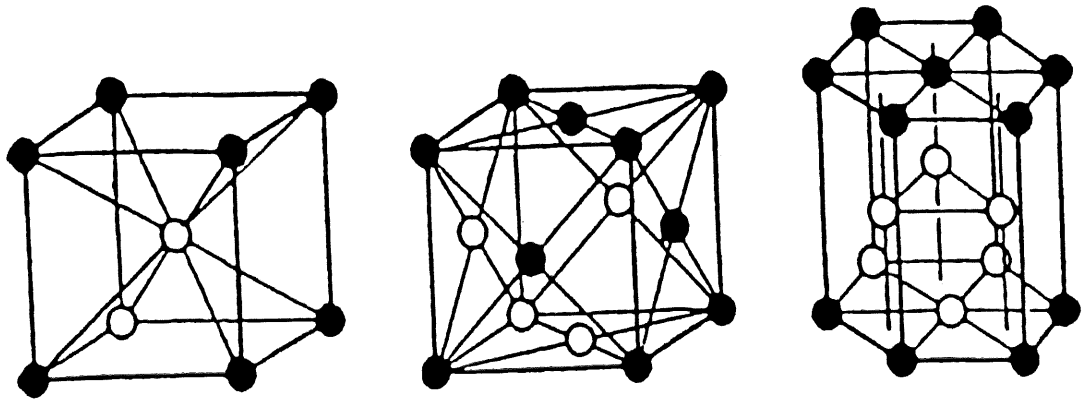

Figure 2.1 The unit cells of BCC, FCC and HCP crystal structures.

Real crystals are rarely perfect. They usually contain imperfections or defects. Lattice imperfections can be characterized geometrically according to whether the disruption in a lattice is at a point, along a line, or over a surface. The most common point imperfections in a crystal are vacancies, interstitial atoms, and substitutional impurity atoms. Vacancies play an important role in deformations at high temperature. The most important is a type of line imperfection, known as a dislocation.

Plastic deformation in polycrystals occurs primarily by the movement of dislocations. The basic concept of dislocations was explained ingeniously by Taylor (1934) as the shearing of different rows of atoms of a crystal in small regions, following their growth through the crystal. The shear stress along the gliding direction on the glide plane of the dislocation, known as the resolved shear stress, supplies the force to cause dislocations to glide. Among the different mechanisms of plastic deformation in metals, such as slip, twinning, grain boundary sliding and diffusion, the translation glide (slip) is the principal one in FCC metals at low and intermediate temperatures. Only this crystallographic slip mechanism is considered in this study.

Crystallographic slip is anisotropic. It implies the massive movement of dislocations along certain crystallographic planes (slip planes) in certain directions (slip directions). Each slip direction on a slip plane defines a *slip system*. These slip directions and planes are almost always those of maximum atomic density, and correspond to those slip systems in which dislocations are most likely to move. Due to the symmetry of the crystal, there are 12 possible slip systems, {111} <110>, for an FCC crystal (Fig. 2.2).

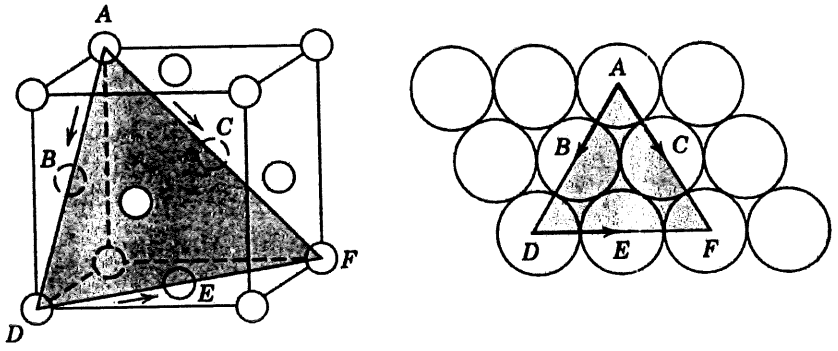

(a) (b)

Figure 2.2 A {111} <110> slip system within an FCC unit cell. (b) The (111) plane from (a) and three <110> slip directions (as indicated by arrows) within that plane comprise possible slip systems.

Slip deformation mechanics is governed by the critical shear stress law (Schmid, 1924), which is often referred to as Schmid's law. It serves as an initial microscopic yield criterion for

single crystals. The Schmid law states that extensive glide occurs when the resolved shear stress attains a critical value; i.e., when

$$\tau^{(\alpha)} = m_{ij}^{(\alpha)}\sigma_{ij} = \tau_y^{(\alpha)} \quad (i,j = 1, 2, 3) \tag{2.1}$$

Here $\tau^{(\alpha)}$ is the resolved shear stress for the slip system α, σ_{ij} is the stress state acting on the crystal, $\tau_y^{(\alpha)}$ is the yield strength of the system α, and $m_{ij}^{(\alpha)}$ is expressed as

$$m_{ij}^{(\alpha)} = s_i^{(\alpha)} b_j^{(\alpha)} \tag{2.2}$$

where $s_j^{(\alpha)}$ and $b_i^{(\alpha)}$ are the components of the slip vector $\boldsymbol{s}^{(\alpha)}$ and slip plane normal $\boldsymbol{b}^{(\alpha)}$, respectively, for the slip system α. In (2.1), and throughout this thesis, the usual summation convention of tensor calculus, is applied. Using (2.2), the components of the plastic strain-rate tensor, $\boldsymbol{D}^{\boldsymbol{p}}$, can be expressed as

$$D_{ij}^{p} = \sum_{\alpha} \frac{1}{2} \left(m_{ij}^{(\alpha)} + m_{ji}^{(\alpha)} \right) \dot{\gamma}^{(\alpha)} \tag{2.3}$$

where $\dot{\gamma}^{(\alpha)}$ is the shear rate on the slip system α.

2.2 Single crystal deformation models

It is well known that the properties of polycrystals can be derived from those of single crystals. With the assumption that plastic deformation is due solely to crystallographic slip, the description of the deformation of single crystals has several versions. Here we discuss two main theories: the rate independent and rate dependent models.

2.2.1 Rate independent deformation

Let $\tau_y^{(\alpha)}$ represent the current value of the yield stress associated with the α slip system and $\tau^{(\alpha)}$ be the corresponding resolved shear stress. The Schmid law yields the following simple flow rule for the shear rates $\dot{\gamma}^{(\alpha)}$ according to the rate independent plasticity theory:

$$\dot{\gamma}^{(\alpha)} = 0 \text{ for } \tau^{(\alpha)} < \tau_y^{(\alpha)},$$

$$\dot{\gamma}^{(\alpha)} = 0 \quad \text{for } \tau^{(\alpha)} = \tau_y^{(\alpha)} \text{ and } \dot{\tau}^{(\alpha)} < h^{\alpha\beta}\dot{\gamma}^{(\beta)}, \tag{2.4}$$

$$\dot{\gamma}^{(\alpha)} \geq 0 \quad \text{for } \tau^{(\alpha)} = \tau_y^{(\alpha)} \text{ and } \dot{\tau}^{(\alpha)} = h^{\alpha\beta}\dot{\gamma}^{(\beta)},$$

Here $h^{\alpha\beta}$ are the components of the slip system hardening matrix, which represent the components of the increment of flow stress on system α due to an increment of shear on system β. In (2.4), and throughout this thesis, repeated Greek indices imply summation over the number of slip systems (12 for FCC crystals) unless indicated otherwise. Equation (2.4) characterizes the inactive, potentially active, and active slip systems.

Since there is essentially no change of volume for a crystal during plastic deformation, only five components of the plastic strain rate tensor are independent. Therefore, there are only five independent equations in Equation (2.3) for the 12 unknowns $\dot{\gamma}^{(\alpha)}$. This implies that a geometrically possible combination of only five independent active slip systems are required to accommodate five independent strains. For FCC crystals which have 12 slip systems, there exist 384 such geometrically possible combinations of 5 slip systems.

In order to select the active slip systems, Taylor (1938) introduced the hypothesis that the actual combination of the slip systems is the one for which the sum of the shear rates is a minimum; i.e.,

$$\sum_{\alpha=1}^{5} \dot{\gamma}^{(\alpha)} = min \tag{2.5}$$

This hypothesis has no obvious a priori justification. However, Taylor based it on observations of single crystals subjected to uniaxial stress and on a postulated analogy with the dynamics of non-conservative mechanical systems.

Bishop and Hill (1951a, 1951b) later recast this theory based on the principle of maximum work, a version of which they derived for a single crystal. In particular, from the principle of maximum work they derived inequalities between external work, computed as the product of macroscopic stress and strain increments, and internal work computed as the integral over the volumes of grains of the products of crystallographic shear strength, and assumed slip increments. They then used these to set bounds on the critical stress state required to induce yield. Indeed the primary aim of the Bishop and Hill theory was the computation of single and polycrystal yield surfaces. They discovered that, for most orientations of a single crystal, the active stress states are on the corners of its yield surface. For FCC metals deformed by {111} <110> slip and which harden isotropically, there are 56 such corner stress states. More than five slip systems are activated on these corners of the yield surface because they are the intersection of at least six planes. Among the 56 stress vertices (28 plus their opposites), 24 will activate 8 slip systems and 32 will activate 6 slip systems.

The use of a yield surface in connection with "maximum plastic work" seems a more valid basis as a selection criterion than Taylor's assumption of "minimum sum of shears". However, Chin and Mammel (1969) proved that the two methods are strictly equivalent. Kocks (1970) and Renouard and Wintenberger (1976) also arrived at the same conclusion.

2.2.2 Rate dependent deformation

The drawbacks of the rate-independent theory arise essentially from the lack of uniqueness in the choice of the actively yielding slip systems. This is because the yield surface of rate-independent single crystals is a polyhedron, and the prescribed strain-rate vector must be

perpendicular to the yield surface. As shown in Fig. 2.3, if the prescribed strain-rate vector is perpendicular to the edge of the yield polygon, it is not possible to uniquely determine the position of the stress vector on the edge. Under such conditions the stress state is ambiguous. Furthermore, if the stress vector is on the corner of the yield locus, six or eight slip systems could possibly be simultaneously activated, and the corresponding slips cannot be uniquely determined from the five equations in Equation (2.3).

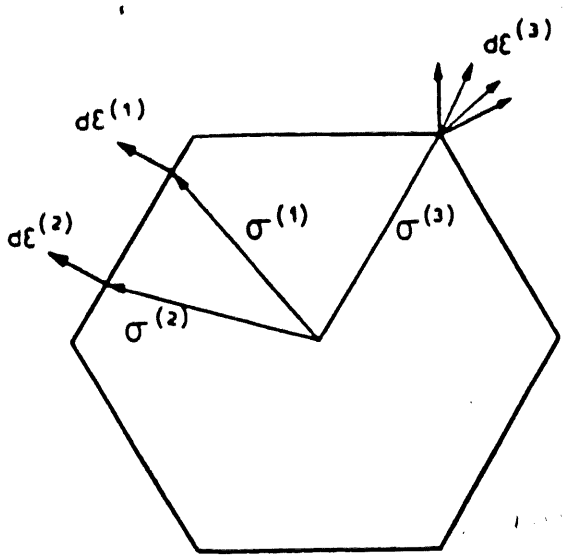

Figure 2.3 Schematic illustration for the stress and slip ambiguities present in the rate independent deformation model

In order to resolve the above ambiguities, Asaro and Needeleman (1985) introduced the rate sensitivity of slip into Taylor-type crystal models. (Details of this formulation will be presented in Chapter 3.) In this rate dependent model, no strict distinction between active and inactive slip systems is made and there is no explicit yielding. Instead, all slip systems slip at a rate which depends on the current value of resolved shear and the stress hardness properties. It is because of the direct and unique relation between slip rates and the prevailing stress state (and the current material state) that the slip rate on each slip system can be determined uniquely, and hence furnish unique solutions. Thus, the long-standing problem of non-uniqueness in the stress

states and in the choice of active slip systems in the rate independent analysis is overcome by the rate dependent model.

2.3 Deformation textures

The common metals in industrial practice are polycrystalline aggregates in which each grain (crystal) can assume different orientations. In forming processes, where metals undergo medium or large deformations, the grains in general do not have random orientations; instead, non-random distributions termed *preferred orientations* or *textures* occur.

The actual orientation distribution of the individual grains in a polycrystal is the result of the manufacturing process. The texture thus reflects the production history of the metal. Textures have profound effects on the mechanical, thermal and electrical properties of materials, as well as on the subsequent performance during fabrication and the final quality of products. For instance, rolling of aluminum, commercial alloys or high-purity materials results in a complex mixture of a range of texture components which include $\{112\}\langle 11\bar{1}\rangle$ (the Cu-component), $\{123\}\langle 41\bar{2}\rangle$ (the S-component), and $\{110\}\langle 1\bar{1}2\rangle$ (the brass-component), as well as a variety of other components. The prediction and simulation of such texture developments are very desirable, since many forming operations are carried out on rolled materials and the forming capability of these metals strongly depend on their textures. Stamping a circular cup from rolled and/or annealed metal sheets with textures, for example, often results in undesirable waves on the sides of the cup, a phenomenon known as "earing". Textures are so important that predicting their development and evolution during deformation is vital for control purposes in industrial practices.

2.4 General introduction to polycrystal deformation models

In addition to the general capabilities of phenomenological models, a polycrystal deformation model must possess other advantages. It should be capable of describing some phenomena which cannot be modelled by phenomenological theories, such as the important polycrystal deformation characteristic – crystallographic textures. In general such a model can be

derived from single crystal deformation models. The issue is how to establish the relationships between microstructural mechanisms of deformation operating on the single crystal level and overall polycrystal behaviour.

To relate the behaviour of a polycrystalline aggregate to that of the constituent single crystals, something must be known or assumed about the stresses or strains of the individual grains. Usually, assumptions are made about the distribution of stresses and strains in the polycrystal, and polycrystal response is identified with some appropriate average of the response of its constituent grains. Several such models have been proposed, which have provided much useful insight into texture development and polycrystal strain hardening behaviour. These models, described below, are based on the concept of polycrystal deformation due to crystallographic slip at the level of the single crystals. Other deformation mechanisms, such as grain boundary sliding, diffusion, and twinning, are neglected.

2.4.1 Sach's model

Sach's (1928) model, one of the earliest polycrystal models, is based on the assumption that each grain is subjected to the same stress state. In this model, the grains are treated as if they were an array of free single crystals which can deform independently of each other. Strain and orientation changes are deduced from the stress in the same way as in the case of a free single crystal submitted to a known stress. Each grain is subjected to the same stress state which is also the macroscopic stress. The model was refined by Kochendorfer (1941) who further stipulated that each grain was subjected to the same stretch.

In this model, because of the assumption that each grain is subjected to the same stress state equal to the macroscopic stress, the stresses arising from constraints necessary to satisfy an imposed strain are neglected. As a result, continuity of strain across a grain boundary is violated (Bishop and Hill, 1951a; 1951b). Also some numerical inconsistencies with experiments exist in this model (Asaro and Needleman, 1985). In general, this theory was not found to be very successful in predicting deformation textures.

2.4.2 The Taylor crystal theory

In order to overcome the objections to Sach's model, Taylor proposed an alternative model. There are two aspects in the original Taylor theory: (a) a criterion for selecting the active slip systems in a deformed single crystal (Section 2.2.1), and (b) the assumptions for linking the deformation behaviour between the constituent grains, and the polycrystalline aggregate.

The basic idea underlying the Taylor model rests on experimental observations. By examining a micrograph of the cross section of a drawn wire, Taylor observed that all the grains were elongated in the direction of extension, and contracted in the two perpendicular directions. He concluded that the strain field throughout the polycrystal is homogeneous, implying that each grain deforms exactly in the same way as the polycrystal. This assumption has served as a tool for linking the deformation behaviour among all constituent grains, and between individual grains and polycrystals. It is now known that it is not exactly true, but the assumption has the advantage of assuring continuity of the strain rate across the grain boundaries so that no voids are created.

With the Taylor assumption the stress state is not continuous, but varies abruptly from grain to grain, depending on different grain orientations. As pointed out by Bishop and Hill (1951a, 1951b), each grain satisfies the relation

$$\sigma_{grain}/\tau = d\gamma/d\varepsilon = M \tag{2.6}$$

where σ_{grain} and $d\varepsilon$ are the axial stress in a grain and the macroscopic aggregate strain increment, respectively, and τ and $d\gamma$ are the shear strength and slip-system shear strain increment, respectively. M is the orientation factor, depending only on the lattice geometry and, in particular, on the relationship between the loading axis and the slip system of the crystal.

Taylor and Elam (1923) studied the uniaxial tension of aluminum polycrystals. By assuming that each grain is at the same stage of strain hardening, Taylor predicted that if τ_y is the yield strength in shear of a single grain, the tensile yield stress of a random aggregate would

be $3.06\tau_y$. Very close agreement was obtained when Taylor tested this theory by comparing the tensile stress–strain relation $(\sigma_{aggre.}-\varepsilon)$ measured on an aggregate with that deduced from the shear stress–strain $(\tau-\gamma)$ curve of single crystal, where

$$\sigma_{aggre.} = \overline{M}\tau$$
$$\varepsilon = \gamma/\overline{M} \tag{2.7}$$

and where $\overline{M}$, the so-called "Taylor factor", may vary from one type of texture to another. Its value is approximately 3.06 for isotropic polycrystals.

Summarizing, two main points emerge from the Taylor theory regarding the relation between the deformation of single crystals and that of polycrystals:

1. The deformation in each crystal is the same as the macroscopic deformation; the shapes of the constituent crystals do not enter in the idealization; and

2. The macroscopic stress of a polycrystal is the average of the stresses of all constituent single crystals.

These concepts are adopted for our numerical analyses.

2.4.3 Relaxed constraint models

In the classical Taylor-type models, five independent slip systems have to be activated to guarantee deformation compatibility of the whole specimen. Since the number of strain conditions (the "number of constraints") is as large as five, such models are referred to as "full constraint" (FC) models.

More recently, a modification of the Taylor model, the method of "relaxed constraints," (RC) has been suggested by Honneff and Mecking (1978) and further developed by Kocks, Jonas, Canova and co-workers (1984) to account for material texture effects. The idea here is to assume that when grains re-orient and take on very distorted shapes, characterised by large aspect ratios of the principal lengths, it is possible to partially relax the strict compatibility requirements imposed in the Taylor model. Non-unuiform deformations (not accounted for in the model) are envisaged to occur at the grain boundaries which accommodate the incompatibilities implied by the non-imposed strain components. When applied to certain deformation states such as axisymmetric tension and compression they argue that the dimensionality of the problem is reduced so that less than five independent slip systems are needed.

The methodology of relaxed constraints has been used by the above authors to analyze deformation textures in FCC polycrystals following several strain histories such as axisymmetric tension and compression, along with large simple shear. Since the imposed strain increments differ from those that would be imposed in a full constraint (Taylor) model, the slip modes and lattice rotations predicted by the two approaches are different. In a few cases the RC method has been reported to lead to predicted textures that are in better agreement with experiment, for example as in the analyses of Canova et al. (1984) of texture development following large simple shear.

2.4.4 Self-consistent schemes

The self-consistent method (SC), based on Eshelby's (1957) concept, was proposed mainly by Kröner (1958), Budiansky and Wu (1962), and Hill (1965). Generally, these models assume a homogenization scheme in which the grain interactions with the matrix are taken into account. In the homogenization scheme, the material properties of a polycrystal aggregate vary from grain to grain, and each grain is treated as a local inhomogeneity embedded in a homogeneous equivalent medium (HEM).

Based on the SC method, Molinari et al. (1987) and Toth et al. (1994, 1997) predicted texture evolution for FCC and BCC polycrystalline materials during rolling and torsion,

respectively. Lebensohn et al. (1993) predicted texture evolution during rolling and axisymmetric deformation of a zirconium alloy. They also determined the plastic anisotropy of a rolled zirconium alloy sheet. Recently Choi et al. (2000) also used the SC method to investigate the effects of crystallographic and morphological texture on the macroscopic anisotropic properties (r-value and normalized yield stress) for AA5019A sheets in H48 and O temper conditions using the full-constraint Taylor and a visco-plastic self-consistent polycrystal model. They have presented results where spherical and ellipsoidal grain shapes were analyzed.

For cubic metals, such as FCC polycrystals, textures predicted by the SC models are rather similar to those obtained with the FC and RC models. Significant differences are observed in plastically more anisotropic hexagonal metals (e.g., Lebensohn et. al., 1994) although sometimes the reorientation due to twinning obscures the comparison between the FC and SC methods.

2.5 Recent developments in crystal plasticity theory

In this section we summarize new developments in crystal plasticity theory and give examples of their applications.

2.5.1 Finite element per single crystal (FESC) model including the effects of the crystal shape on texture evolution

Another approach, which is capable of including the effects of crystal shape on texture evolution, utilizes finite element methodologies to discretize the crystals of an aggregate using one or more elements for every crystal. In this model, a polycrystalline aggregate is treated as a continuum where both compatibility and equilibrium among the individual grains are automatically satisfied.

Asaro and co-workers (e.g., Harren et al., 1988) have conducted some novel experiments and simulations of shear band formation in Al-3wt% Cu FCC single and polycrystals under plane strain compression. In their work, they modelled each grain by a number of finite elements to

allow for non-uniform deformations within the grains. Their simulations of the deformation response of a multi-crystal comprising of 27 grains provided good insight into the underlying micromechanical mechanisms of localized deformation in crystalline materials.

Recently, Mathur et al. (1990) extended the mathematical formulation developed earlier by Mathur and Dawson (1989) to account for the effects of grain shape on the development of deformation-induced crystallographic textures using the relaxed constraints approach of Honneff and Mecking (1978), Kocks and co-workers (Kocks and Canova, 1981; Canova et al., 1984; Tomé et al., 1984). Within their framework, each grain could no longer be treated independently nor could the stresses from all grains in an aggregate simply be averaged. Rather, in a restricted sense the actual continuity requirements from continuum mechanics were enforced across flat grain boundaries, while the overall deformation of an aggregate was constrained to match the macroscopic deformation of the material point. They simulated the flat rolling of polycrystalline aluminum as an application for their model, and compared the predicted deformation textures with the predictions of an earlier study which were based on a Taylor model. Several detailed comparisons indicated that the texture predictions made by the new model, which accounts for the effects of grain morphology, matched the experimental observations more closely.

Kalidindi et al. (1992) developed a finite element polycrystalline model where each element represented one crystal and sets of initially "random" grain orientations were assigned to the elements. As with Taylor model simulations, the macroscopic stress–strain response and crystallographic texture were computed as volume averages over the entire aggregate. The crystallographic texture was obtained by a direct equal-area projection of the orientations of all grains. Their calculations satisfied (in the "weak" finite element sense) both compatibility and equilibrium in the aggregate. They analysed FCC, polycrystalline, oxygen-free-high-conductivity (OFHC) copper for (i) planar simple shear and thin-walled tubular torsion to large shear strains, and (ii) a simple plane-strain forging operation. Their results clearly indicated that the new model nicely captured the major features of the evolved textures.

Bronkhorst et al. (1992) used the model proposed by Kalidindi et al. (1992) to simulate "nominally homogeneous" deformations of simple compression and tension, plane strain

compression, and simple shear of a polycrystalline aggregate by using a multitude of single crystals. They compared their results against those from Taylor-type calculations and concluded that their model was in much better agreement with the experiments than was the Taylor-type model. Anand and Kalidindi (1994) also used the model proposed by Kalidindi et al. (1992) to simulate the effects of crystallographic texture evolution on the process of shear band formation in plane strain compression of initially isotropic OFHC polycrystalline copper. They computed deformed textures that are in very good qualitative agreement with the experimental texture after an axial compressive strain of -1.0.

Beaudoin et al. (1995) developed a finite element model based on a hybrid formulation to investigate the averaging of crystal microscopic responses developed during the course of a macroscopic deformation. They simulated channel die compression with one crystal per finite element and compared their results with simulations obtained from the FC and RC models. Their hybrid finite element formulation was able to predict the development of the brass texture component in the 90° section of the crystal orientation distribution (COD), while there was no evidence of formation of this texture component in their RC simulation. While their FC model showed texture development in the 90° section, it was away from the brass location indicated by the experimental data.

The study of a model polycrystal using finite element simulations (Sarma and Dawson, 1996a) showed neighbour interactions to be the main factor in determining the spread of the applied deformation among the crystals. Sarma and Dawson (1996b) presented a viscoplastic model for distributing the deformation applied to a polycrystal in a non-uniform fashion among the constituent crystals. Their finite element model was based on the hybrid formulation of Beaudoin et al. (1995). Polycrystal simulations of crystallographic texture development under plane strain compression and simple shear were simulated with this model, and the results obtained were compared to the results of similar calculations using a Taylor model. They concluded that the model incorporating neighbour interactions improved texture predictions, in terms of both the intensity levels and the locations of certain texture components.

Recently, Acharya and Beaudoin (2000) proposed a constitutive model for the prediction of grain-size dependent hardening in FCC polycrystalline metals where they considered a purely viscoplastic response. Later on, Beaudoin et al. (2000) extended this work to include effects of temperature and strain rate dependence. Their work has provided detailed comparisons between their model and experimental compression data, taken at varying temperature and strain rate, for pure Ag having two different grain sizes.

2.5.2 Strain gradient plasticity

Dislocation theory suggests that the plastic flow strength of a solid depends not only on strains, but also on strain *gradients*. Hardening is due to the combined presence of geometrically necessary dislocations associated with a plastic strain gradient and statistically stored dislocations associated with plastic strain. In general, strain gradients are inversely proportional to the length scale over which plastic deformation occurs. Thus, gradient effects become important for plastic deformations taking place at small scales. Experimental evidence suggests that the flow strength increases with diminishing size, at length scales on the order of several microns or less.

The most general versions of the theories proposed fit within the Toupin (1962) and Mindlin (1964) strain gradient framework, which involves all components of the strain gradient tensor and work-conjugate higher-order stresses in the form of couple stresses and double stresses. A specialized version deals with only a subset of the strain gradient tensor in the form of deformation curvatures (i.e., rotation gradients). This is the simpler couple stress framework.

Experimental evidence is accruing for the existence of a strong size effect in the plastic flow of metals and ceramics. For example, the measured indentation hardness of metals and ceramics increases by a factor of about two as the width of the indent is decreased from about 10 μm to 1 μm (Stelmashenko et al., 1993; Ma and Clarke, 1995). The well-known Hall-Petch (1951) effect states that the yield strength of pure metals increases with diminishing grain size. Long-standing observations of shear bands in metals have revealed that micro-shear band widths appear to be consistently on the order of a micron. Simple dimensional arguments lead to the conclusion that any continuum theory for each of these phenomena based solely on strain

hardening, with no strain gradient dependence, would necessarily predict an absence of any such size effect.

Gradient effects in an elastic single crystal of pure metal become significant only for deformation fields with wavelengths on the order of the atomic spacing. However, when plastic deformation occurs, gradient effects can become important at much larger scales. Fleck and Hutchinson (1997) used the notions of statistically stored dislocations and geometrically necessary dislocations to provide the physical basis for a continuum theory of single-crystal plasticity. They assumed that slip occurs on specific slip systems in a continuous manner, and that the increment in flow strength of any given slip system depends upon the rates of both the strain and the first spatial gradient of strain. Their crystal theory fits within the framework of Toupin (1962) and Mindlin (1964, 1965) strain gradient theory.

Following Mindlin (1964) and Fleck and Hutchinson (1997), Shu and Fleck (1997) presented a formulation where they assumed that the per unit volume internal work rate of a strain gradient solid consists of two parts: the usual second order stress tensor and a third order double stress tensor. They used this formulation to investigate the size dependent deformation of bicrystals. Recently Shu and Barlow (2000) demonstrated the improved modelling accuracy of a finite deformation strain gradient crystal plasticity formulation over its classical counterpart by conducting a joint experimental and numerical investigation of the microscopic details of the deformation of a whisker-reinforced metal matrix composite. They obtained the lattice rotation distribution around whiskers in thin foils using a transmission electron microscopy (TEM) technique, and then correlated these results with numerical predictions based on finite element analyses of a unit-cell of a single crystal matrix containing a rigid whisker. Their strain gradient formulation accounted for both strain hardening and strain gradient hardening. They found that, while a classical crystal formulation tends to over-predict the spatial gradient of the deformation, the strain gradient formulation was able to predict a more smooth field with significantly lower gradients and thus in better correlation with the TEM measurements.

Acharya and Bassani (2000) developed a simple constitutive model where lattice incompatibility only enters the instantaneous hardening relations, and thus the incremental

moduli, which preserves the classical structure of the incremental boundary value problem. Due to this inclusion of a material parameter with dimensions of length in the hardening response, an intrinsic length-scale was introduced in their theory. Spatial derivatives of elastic deformation entered into material response which, at least in the case of single slip, make the slip evolution dependent on spatial derivatives of slip. They have discussed the implications of their modified constitutive structure with respect to the incremental boundary value problem of equilibrium for rate-independent and rate-dependent response.

2.5.3 Models including backstress

Polycrystalline plasticity formulations to date have neglected explicit effects of dislocation substructure in the constitutive relations. As a result, symptoms which lack physical bases arise, such as premature texture development (Harren et al., 1989).

When a metal deforms inelastically, inhomogeneities arise due to mechanisms at several length scales. These inhomogeneities can arise from single dislocation sources at the lattice, or at a higher length scale via dislocation cell boundaries enclosing equiaxed volumes that contain few dislocations. Inhomogeneities can also arise at higher length scales from geometrically necessary boundaries (GNBs) which surround groups of cells in cell blocks (CBs) (Kuhlman-Wilsdorf, 1989; Hansen, 1990; Leffers, 1992). Inhomogeneities give rise to internal stresses associated with local hard and soft regions; hence, macroscale hardening behaviour during inelastic deformation ensues from dislocations simultaneously interacting throughout a range of length scales. These inhomogeneties not only generate short range stresses at a local level which induce anisotropy, but also affect the polycrystalline elastic anisotropy.

The crystal plasticity models that have previously been discussed have been successful in predicting the elasto-plastic behaviour as well as the texture evolution for crystalline materials. However, backstress evolution has been neglected in these models. The backstress is a residual stress embedded in the polycrystalline or single crystal material at the crystal-lattice level due to plastic deformation of crystals. Within the context of dislocation resistance, the notion of backstress was studied by Mughrabi (1983). It has been used in some plasticity models to describe the Bauschinger effect which has been associated with sequential activation, de-

activation, and dislocation substructures. The backstress arises as dislocation densities at the GNBs are high enough to induce a tensile stress state (or forward stress) such that regions between them experience a compressive stress state. To maintain compatibility at the interface between the boundaries and interiors of the subgrain, the GNBs serve as barriers to dislocation motion and give rise to backstress. These backstresses influence the work-hardening rate and limit the free operation of dislocation sources in the softer cell interiors when the material is reloaded. Tensile stresses (or forward stresses) in the boundaries assist the applied stresses to operate on the sources with shorter dislocation segments.

Horstemeyer and McDowell (1998) introduced a second rank micro-heterogeneity internal state variable (ISV) tensor into the elastoviscoplastic polycrystalline framework (Rashid and Nemat-Nasser, 1990) to represent effects of dislocation substructures in the form of geometrically necessary boundaries (GNBs). This evolving ISV was resolved onto the slip systems using Schmid's law to introduce kinematic hardening (i.e., a backstress) in the flow rule. The micro-heterogeneity ISV tensor that they introduced also affected the intergranular constraint by using a self-consistent (relaxed constraint) method analogous to that of Berveiller and Zaoui (1979). This micro-heterogeneity ISV relates the dislocation substructure evolution to the backstress for intergranular hardening, and to the grain boundaries for intergranular hardening. By including the micro-heterogeneity ISV into the elastoviscoplastic polycrystalline framework relative to the Taylor model, they improved trends of correlations with experimental compression and torsion stress–strain curves. Also the trends of their prediction of axial stresses in fixed end torsion tests were more realistically simulated as second order axial effects were shown to depend on both texture and dislocation substructure. Two other noteworthy results presented were that the trends of intensity and distribution (spread) of texture evolution were more realistically predicted, and that the trends of prediction of polycrystalline elastic moduli for deformed OFHC Cu and 304L stainless steel were more accurately simulated. Also their elastoviscoplastic calculations with the micro-heterogeneity ISV model showed that torsion produced a higher degree of anisotropy than compression since the backstress magnitude for torsion was greater than for compression. Their results and also other results such as presented by Voyiadjis and Huang (1996) and Dawson et al. (1999) suggest that residual stresses such as backstresses and their evolution should be considered for a physically-based polycrystalline framework.

2.5.4 Discrete dislocation plasticity

As has already been discussed, conventional plasticity theories are length-scale independent and exclude the effects of strain gradients. However, based on crystal plasticity, Van Der Giessen and Needleman (1995) have presented a method for solving small-strain plasticity problems with plastic flow represented by the collective motion of a large number of discrete dislocations. Their formulation assumes that the ensuing deformation process is quasi-static and involves small strains. The process leads to the motion of dislocations, mutual annihilation, the generation of new dislocations and their pinning at point obstacles. The analysis of Van Der Giessen and Needleman (1995) of the deformation process is performed in an incremental manner in time, where the incremental step at any instant t involves three main computational stages. First, for the current dislocation arrangement, the current stress, and the strain state of the problem are determined. Secondly, from that state, the so-called Peach-Koehler force, i.e., the driving force for changes in the dislocation structure, is determined. Finally, the instantaneous rate of that dislocation structure is computed on the basis of a set of constitutive equations for motion, annihilation and generation of dislocations.

Van Der Giessen and Needleman (1995) have presented results for monophase and composite materials with periodic microstructures subjected to simple shear loading. Even though they were only for a single slip system and use assumptions for sources and obstacles, the results showed a number of noteworthy features; especially for problems of plastic flow near crack tips, around micro-indentors and in composite materials, at a scale where the collective motion of large numbers of dislocations and discrete dislocation effects play a role. Their results indicate that, for the aforementioned microscale problems, continuum plasticity may not give the desired resolution of stress and strain fields on that scale, and that the discrete nature of dislocations may need to be accounted for.

2.6 Crystal plasticity numerical analyses

In this section, a brief summary of numerical analyses based on crystal plasticity will be presented. Before reviewing simulations for polycrystals, we discuss some analyses based on

single crystal models since these analyses provide a foundation for understanding the nature of nonuniform deformations in crystals.

Numerical analyses of plane strain tension for single crystals have been presented by Peirce et al. (1982, 1983). They demonstrated that nonuniform deformations, crystal lattice rotations, and the evolution of shear bands in single crystals could be modelled using the finite element method. Shear band formation during the plane strain compression of single crystals has been analyzed by Harren et al. (1987). Subsequently, Dève et al. (1988) investigated shear band bifurcation strains, shear band angles, as well as lattice orientations within shear bands. Their predictions were found to be in good agreement with experimentally measured values.

There have been significant advances in implementing single crystal deformation mechanisms in polycrystal constitutive models as well as in the application of these models. A pioneering work is that of Asaro and Needleman (1985) who have presented an elastic-plastic, rate-dependent polycrystalline constitutive model for low homologous temperatures. The global response of the polycrystal was obtained by employing the Taylor (1938) hypothesis. Accordingly, the deformations in each grain of the aggregate were taken to be uniform and equal to the macroscopic deformation, while the macroscopic stresses in the polycrystal were obtained as the average of the stresses in each crystal. As applications of their formulation, Asaro and Needleman (1985) analyzed uniaxial tension, plane strain tension, and compression. Furthermore, they presented sheet necking simulations based on the analysis proposed by Marciniak and Kuczynski (1967) (referred to as the M-K analysis) both for isotropic and strongly textured sheets. Finite element predictions based on their formulation for the evolution of texture in plane strain compression and simple shear in FCC polycrystals have been compared against existing experimental work on copper (Harren et al., 1988; Harren and Asaro, 1989). It was found that all of the relevant features of experimentally determined textures could be captured by this formulation.

Using the polycrystal model proposed by Asaro and Needleman (1985), Harren et al. (1989) presented numerical analyses of large-strain shear in FCC polycrystals. In their work, they investigated the effects of strain hardening, latent hardening, strain-rate sensitivity, and initial

textures on texture evolution and constitutive response. However, their analyses were restricted to conditions of homogeneous simple shear. Neale et al. (1990) presented an accurate analysis of fixed end torsion of a solid bar using a Taylor-type rate dependent polycrystal model. Their analysis was based on a special solution procedure in which the solution was obtained from the response to simple shear. They concluded that the trends for the stresses which develop in solid bar torsion may differ considerably from those of homogeneous simple shear.

Mathur and Dawson (1989) incorporated a Taylor-type polycrystal model into an Eulerian finite element procedure. They used this approach to predict the evolution of crystallographic texture in a steady-state aluminum rolling procedure. A streamline technique was employed to integrate the evolution equations for the lattice rotations and the slip system hardnesses. As an extension of this work, Mathur et al. (1990) analyzed the development of deformation-induced texture during bulk forming processes using the "finite element per single crystal" (FESC) model discussed in Section 2.5.1. Other applications with the FESC model have already been discussed in Section 2.5.1 (e.g., Kalidindi et al., 1992; Bronkhorst et al., 1992; Anand and Kalidindi, 1994; Beaudoin et al., 1995; Sarma and Dawson, 1996b).

Becker (1992) also employed the Asaro and Needleman (1985) polycrystal formulation to simulate the development of shear localization in a polycrystalline sheet subjected to pure bending. His simulations showed that the predicted bands of localized plastic deformation occurred at realistic strain levels and at angles which were in agreement with the shear band angles in a bent sheet. Simulations of earing during the deep drawing of polycrystalline aluminum sheets have also been presented by Becker et al. (1993). Their analysis was based on a special flange analysis (which will be discussed in Chapter 6), and the results were in good agreement with experiments.

Van der Giessen and Neale (1993) extended the polycrystal model employed by Neale et al. (1990) to include the anisotropic elasticity of the crystals as well as slip system hardening (similar to that of Asaro and Needleman, 1985). This work was the first numerical study based on polycrystal plasticity for the inverse Swift effect. They analyzed free-end twisting, unloading and subsequent free-twisting extension of solid bars, and concluded that textures produced during

each of the above stages are of prime importance for the inverse Swift effect. More recently, Wu et al. (1996) have analyzed the behaviour of FCC polycrystals during reversed torsion.

Using the previously mentioned M-K approach, Tvergaard and Needleman (1993) investigated the development of localized shear bands in polycrystals subjected to plane strain tension, biaxial stretching, and large strain shear. In their analyses, which was also based on the polycrystal model formulation of Asaro and Needleman (1985), they investigated the effects of variations in imperfection amplitude and material strain-rate sensitivity on the formation of shear bands. Zhou and Neale (1995) have directly applied a rate dependent crystal plasticity model in conjunction with the M-K approach to predict forming limit diagrams (FLDs) for annealed FCC sheet metals. Subsequently, Wu et al. (1997, 1998) and Savoie et al. (1998) used the Asaro and Needleman (1985) polycrystal plasticity formulation to compute the FLDs for FCC polycrytals. They discussed in detail the effects of various material parameters on the predicted FLDs, and showed that this analysis leads to very good agreements with experimental trends.

2.7 Discussion and conclusion

In this chapter, the deformation characteristics of single crystals and polycrystals have been presented. The principles of anisotropy were well understood for single crystals by the 1950s, even for the grossly nonlinear properties of plastically deforming solids. Predicting the anisotropy of polycrystals from single crystal properties involves two fundamental steps: (a) the determination of the texture by measuring the orientations of all crystals of a polycrystal, and (b) an averaging scheme for combining single crystal properties into polycrystal behaviour which, at least for mechanical properties, is not a trivial task.

The inherent difficulty with the rate independent formulation; loss of uniqueness of the "mode of slip", was solved when Asaro and Needleman (1985) introduced the rate sensitivity of slip into Taylor-type crystal models. In this rate dependent model, slip rates are directly and uniquely related to the prevailing stress state allowing the unique determination of the slipping rate on each slip system.

Crystal plasticity models reviewed in Section 2.4 can be classified in two groups: the self-consistent models and the Taylor-type models. The self-consistent models are more complex than the Taylor-type models; they explicitly account for the interaction of each grain (or subdomains in the grain) with its surroundings, for the relative anisotropies of the grains, and for grain shape effects. As a result, they can be used to analyze problems that cannot be investigated properly with the simpler Taylor-type models, such as the plastic deformation of highly anisotropic materials with a limited number of slip systems, or the heterogeneous deformation of polyphase materials. However, the assumption of an isotropic matrix may not be valid at large deformations, and they involve very lengthy and complex calculations for simulations of polycrystal deformation.

Compared to the self-consistent models, the Taylor-type models are simpler, and the corresponding calculation procedures are much shorter than the self-consistent ones. Therefore, they have been more widely used for simulations of polycrystal deformation, particularly for predictions of texture development. The Taylor hypothesis can be described as a partitioning assumption in which the analysis does not require detailed definition of the aggregate topology. The partitioning of the macroscopic deformation among the crystals of a polycrystalline aggregate is done without regard to which crystals are neighbour of which.

The evaluation of the validity of Taylor's model has been done exclusively through comparisons of its predictions with experimental results. Comparisons of predicted textures based on the Taylor theory with experimentally observed textures have been carried out by many authors. Kocks et al. (1988) concluded that the Taylor model can successfully refer aluminum, copper and silver deformation to large strains by wiredrawing, compression and torsion to one single work-hardening master curve when the initial textures are included in the model calculations.

The Taylor assumption suffices for evaluating the mechanical response of an aggregate if the grains are nearly equiaxed and the strains accumulated over the loading path are not too large. However, heavily worked grains become distorted with the consequence that the deformation of individual grains may not be the same as the macroscopic deformation. Rather, even though

collectively the grains in an aggregate follow the macroscopic deformation, individual grains may be more likely to exhibit responses that differ from the mean. In essence, the constraints on one grain from its neighbours are qualitatively different from those demanded by a Taylor assumption, and thus different combinations of deformation modes in each grain are activated. This directly affects subsequent texture development and thereby influences the anisotropy imparted to the flow and yield properties of the polycrystal. Under these conditions, if grain shape effects are not included, the predicted textures are not in good agreement with the experimental textures.

In order to account for the grain shape effects, the so-called "finite element per single crystal" models were developed where the crystals of an aggregate are modelled by elements, using one or more elements for every crystal. These finite element calculations furnish detailed analyses of the plastic behaviour for each individual grain, which in turn provides an understanding of the mechanisms that contribute to the deformation of the polycrystal. As discussed in Section 2.5.1, many authors have presented improved predictions of the major and minor texture components at large strains by including grain shape effects in the analyses.

Another important concept relates to the residual stresses at the crystal level in a polycrystalline metal following plastic deformation. Residual stresses exist in polycrystals after unloading as a consequence of the single crystal anisotropy and grain interactions. One important residual stress is the backstress embedded in the polycrystalline or single crystal at the crystal lattice level. Computations have shown that backstresses can have important effects on the trends of intensity and distribution of texture evolution (e.g., Horstemeyer and McDowell, 1998).

Considering all the polycrystal models that have been described in this chapter, it is fair to conclude that the Taylor model for polycrystalline materials is in very good first-order agreement with experiments for the evolution of texture and the overall stress–strain response of single phase FCC materials. It has been regarded as one of the most successful models, and is widely accepted for analyzing deformation responses and texture evolution in polycrystals. Thus, for the numerical simulations presented in this study, the rate dependent Taylor type polycrystal model is adopted.

CHAPTER 3

POLYCRYSTAL DEFORMATION FORMULATION AND NUMERICAL ANALYSIS

3.1 Formulation

The polycrystal deformation analysis used in the present study is based on Asaro and Needleman's (1985) Taylor-type formulation. It includes five aspects: (i) the polycrystalline nature of the metal, (ii) the microscopic deformation mechanism, assumed to be rate-dependent crystallographic slip, (iii) the evolution of crystallographic texture, (iv) anisotropic crystal elasticity, and (v) finite deformations.

This formulation considers a material point as a collection of a certain number of grains. The deformation in each grain is taken to be identical to the macroscopic deformation of the continuum. Furthermore, the macroscopic values of all quantities, such as stresses, stress rates and elastic moduli, are obtained by averaging their respective values over the total number of grains at the particular material point. In this model, strain compatibility is satisfied from grain to grain, but equilibrium may be violated on the grain boundaries, since the state of stress may vary among the grains of the aggregate in general. However, the average macroscopic stresses are required to satisfy equilibrium and balance the external tractions.

The mathematical formulation based on this model, and used in our finite element procedure, attempts to simulate any evolving plastic anisotropy by tracking all the grains at a material point, and computing how the grains rotate and how the slip systems of these grains strain-harden. It is worthwhile to mention that, even though our applications are simulated as 2-D modes of deformation, the constitutive model and computational procedures incorporate the full 3-D slip structure of FCC crystals.

3.1.1 Notations

Standard notations are used throughout this thesis. Tensors and vectors are denoted by bold-faced letters and the symbol $\otimes$ denotes the tensor product. The following operations for arbitrary second-order tensors $\boldsymbol{a}$ and $\boldsymbol{b}$ apply: $\boldsymbol{ab} = a_{ik}b_{kj}\,\boldsymbol{e}_i \otimes \boldsymbol{e}_j$ ($\boldsymbol{e}_i$ being a cartesian basis), $\boldsymbol{a} \cdot \boldsymbol{b} = a_{ij}b_{ij}$, with proper extension to higher order tensors. Superscripts T and -1 denote the transverse

and inverse of a second order tensor respectively. The trace is denoted by tr. Furthermore, Latin indices range from 1 to 3.

3.2 Single crystal constitutive model

The total deformation of a single crystal is taken to be the result of two distinct physical mechanisms: crystallographic slip due to dislocation motion on the active slip systems, and elastic lattice distortion (e.g., Rice, 1971; Hill and Rice, 1972). Within an FCC crystal, plastic deformation occurs by crystallographic slip on the 12 $\{111\}\langle 110\rangle$ slip systems where the slip planes are the $\{111\}$ crystallographic planes with normals $\boldsymbol{b}$, and the $\langle 110\rangle$ directions are the shear directions with slip vectors $\boldsymbol{s}$. Plastic deformation is envisaged to occur as a set of plastic simple shears along the various slip systems, leaving the lattice and the slip system vectors ($\boldsymbol{s}^{(\alpha)}$, $\boldsymbol{b}^{(\alpha)}$) not only essentially undistorted, but also unrotated. (The brackets for the subscripts α indicate that α is not a tensor index, and its value ranges from one to the total number of slip systems.) Next, the material and lattice are considered to deform elastically and rotate rigidly from the plastically deformed state to the current configuration as illustrated in Fig. 3.1.

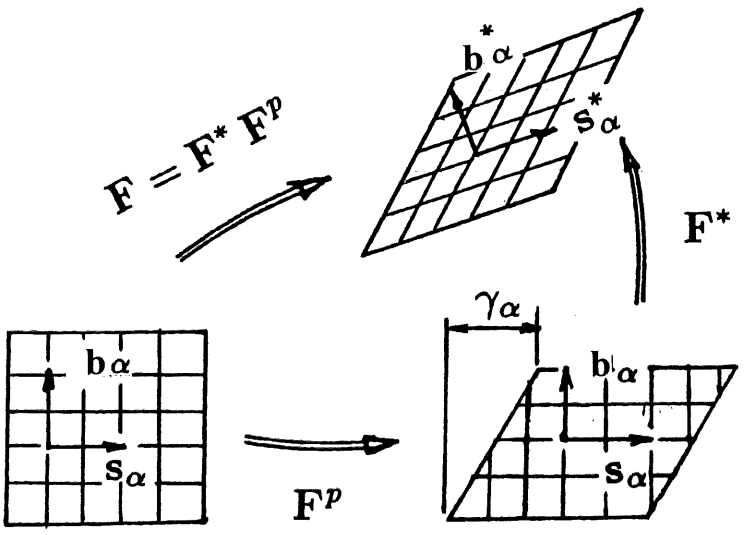

Figure 3.1 Decomposition of the deformation gradient $\boldsymbol{F}$

As a result of the above deformation mechanism, the deformation gradient $\boldsymbol{F}$ can be written as:

$$\boldsymbol{F} = \boldsymbol{F}^{*}\boldsymbol{F}^{p}, \tag{3.1}$$

where $\boldsymbol{F}^{p}$ consists solely of crystallographic slipping along the specific slip systems, while the elastic deformation and any rigid body rotation are embodied in $\boldsymbol{F}^{*}$. The deformation in (3.1) can be envisioned as occurring in two stages: material first moves though the undeformed crystal lattice according to $\boldsymbol{F}^{p}$ and then the lattice and material deform together giving rise to $\boldsymbol{F}^{*}$. From (3.1), the spatial gradient of velocity can be written as

$$\boldsymbol{L} = \dot{\boldsymbol{F}}\boldsymbol{F}^{-1} = \boldsymbol{L}^{*} + \boldsymbol{L}^{p}, \tag{3.2}$$

where

$$\boldsymbol{L}^{*} = \dot{\boldsymbol{F}}^{*}\boldsymbol{F}^{*-1},\ \boldsymbol{L}^{p} = \boldsymbol{F}^{*}(\dot{\boldsymbol{F}}^{p}\boldsymbol{F}^{p-1})\boldsymbol{F}^{*-1} \tag{3.3}$$

The vectors $\boldsymbol{s}^{(\alpha)}$ and $\boldsymbol{b}^{(\alpha)}$ are regarded as lattice vectors that remain orthogonal. Accordingly, they stretch and rotate by

$$\boldsymbol{s}^{*(\alpha)} = \boldsymbol{F}^{*}\boldsymbol{s}^{(\alpha)},\ \boldsymbol{b}^{*(\alpha)} = \boldsymbol{b}^{(\alpha)}\boldsymbol{F}^{*-1} \tag{3.4}$$

Taking the symmetric and antisymmetric parts of (3.2) and (3.3) leads to the elastic and plastic strain rates $\boldsymbol{D}^{*}$ and $\boldsymbol{D}^{p}$, the so-called plastic spin Ω^{P}, and the spin Ω^{*} associated with the rigid lattice rotation

$$\boldsymbol{D} = \boldsymbol{D}^{*} + \boldsymbol{D}^{p},\ \Omega = \Omega^{*} + \Omega^{P} \tag{3.5}$$

where

$$\boldsymbol{D}^{p}=\sum_{\alpha=1}^{N}\dot{\gamma}^{(\alpha)}\frac{1}{2}\left(\boldsymbol{s}^{*(\alpha)}\otimes\boldsymbol{b}^{*(\alpha)}+\boldsymbol{b}^{*(\alpha)}\otimes\boldsymbol{s}^{*(\alpha)}\right)$$

$$\Omega^{p}=\sum_{\alpha=1}^{N}\dot{\gamma}^{(\alpha)}\frac{1}{2}\left(\boldsymbol{s}^{*(\alpha)}\otimes\boldsymbol{b}^{*(\alpha)}-\boldsymbol{b}^{*(\alpha)}\otimes\boldsymbol{s}^{*(\alpha)}\right) \tag{3.6}$$

By introducing the following symmetric and skewsymmetric tensors for each slip system α

$$\boldsymbol{P}^{(\alpha)}=\frac{1}{2}\left[\boldsymbol{b}^{*(\alpha)}\otimes\boldsymbol{m}^{*(\alpha)}+\boldsymbol{b}^{*(\alpha)}\otimes\boldsymbol{s}^{*(\alpha)}\right]$$

$$\boldsymbol{W}^{(\alpha)}=\frac{1}{2}\left[\boldsymbol{s}^{*(\alpha)}\otimes\boldsymbol{b}^{*(\alpha)}-\boldsymbol{b}^{*(\alpha)}\otimes\boldsymbol{s}^{*(\alpha)}\right], \tag{3.7}$$

the plastic strain rate and plastic spin for the crystal can be written as

$$\boldsymbol{D}^{p}=\sum_{\alpha}\boldsymbol{P}^{(\alpha)}\dot{\gamma}^{(\alpha)},\ \Omega^{p}=\sum_{\alpha}\boldsymbol{W}^{(\alpha)}\dot{\gamma}^{(\alpha)} \tag{3.8}$$

respectively, where $\dot{\gamma}^{(\alpha)}$ is the shear rate on the slip system α.

The elastic constitutive equation for a crystal is specified by

$$\overset{\nabla}{\tau}^{*}=\dot{\tau}-\Omega^{*}\tau+\tau\,\Omega^{*}=\mathbf{L}\boldsymbol{D}^{*}, \tag{3.9}$$

where $\overset{\nabla}{\tau}^{*}$ is the Jaumann rate of the Kirchhoff stress tensor τ based on the lattice rotations, and $\mathbf{L}$ is the tensor of the elastic moduli. These moduli are based on the anisotropic elastic constants of the FCC crystals and thus exhibit the appropriate cubic symmetry.

In order to express the constitutive law (3.9) in terms of the Jaumann rate $\overset{\nabla}{\boldsymbol{\sigma}}$ of the Cauchy stress $\boldsymbol{\sigma} = \det(\boldsymbol{F})^{-1}\boldsymbol{\tau}$, based on the continuum slip $\boldsymbol{W}$, we introduce a second-order tensor $\boldsymbol{R}^{(\alpha)}$ for each slip system as follows

$$\boldsymbol{R}^{(\alpha)} = \mathbf{L}\,\boldsymbol{P}^{(\alpha)} + \boldsymbol{W}^{(\alpha)}\boldsymbol{\sigma} - \boldsymbol{\sigma}\,\boldsymbol{W}^{(\alpha)} \tag{3.10}$$

Using (3.4) – (3.8) and (3.10), the constitutive equation (3.9) can be rewritten in the form

$$\overset{\nabla}{\boldsymbol{\sigma}} = \mathbf{L}\,\boldsymbol{D} - \dot{\boldsymbol{\sigma}}^{0} - \boldsymbol{\sigma}\ \mathbf{tr}\,\boldsymbol{D} \tag{3.11}$$

where $\dot{\boldsymbol{\sigma}}^{0}$ is a viscoplastic type stress rate defined by

$$\dot{\boldsymbol{\sigma}}^{0} = \sum_{\alpha} \boldsymbol{R}^{(\alpha)}\dot{\gamma}^{(\alpha)} \tag{3.12}$$

The slip rates to be substituted into equation (3.12) are taken to be governed by the power law expression

$$\dot{\gamma}^{(\alpha)} = \dot{\gamma}_{(0)}\,\mathrm{sgn}\,\tau^{(\alpha)}\left|\frac{\tau^{(\alpha)}}{g^{(\alpha)}}\right|^{1/m} \tag{3.13}$$

where $\dot{\gamma}_{(0)}$ is a reference shear rate taken to be the same for all the slip systems, $\tau^{(\alpha)} = \boldsymbol{P}^{(\alpha)} : \boldsymbol{\sigma}$ is the resolved shear stress on slip system α, and $g^{(\alpha)}$ is its hardness. The constant m characterizes the material strain-rate sensitivity, which is taken to be the same for each slip system. For the limiting case as $m \to 0$, the analysis becomes rate-insensitive.

For multiple slip, the evolution of slip system hardness is governed by:

$$\dot{g}^{(\alpha)} = \sum_{\beta} h_{(\alpha\beta)}\left|\dot{\gamma}^{(\beta)}\right| \tag{3.14}$$

where $g^{(\alpha)}(0)$ is the initial hardness, taken to be a constant τ_0 for each slip system, and $h_{(\alpha\beta)}$ are the hardening moduli. The form of these moduli is

$$h_{(\alpha\beta)} = q_{(\alpha\beta)} h_{(\beta)} (\text{no sum on } \beta) \tag{3.15}$$

where $h_{(\beta)}$ is a single slip hardening rate and $q_{(\alpha\beta)}$ is the matrix describing the latent hardening behaviour of the crystallite. For FCC crystals with 12 slip systems, we take $q_{(\alpha\beta)}$, as in Asaro and Needleman (1985), to be given by

$$q_{(\alpha\beta)} = \begin{bmatrix} A & qA & qA & qA \\ qA & A & qA & qA \\ qA & qA & A & qA \\ qA & qA & qA & A \end{bmatrix} \tag{3.16}$$

where q is the ratio of the latent hardening rate to self-hardening rate, and A is a 3 x 3 matrix fully populated by ones. In the above, slip systems {1,2,3} are coplanar, as are systems {4,5,6}, {7,8,9} and {10,11,12}. Thus, the ratios of the latent hardening rates to the self-hardening rates for coplanar systems are taken as unity.

Asaro and Needleman (1985), among others, simply take each $g^{(\alpha)}$ to depend on the accumulated sum, γ_a, of the slips; i.e.

$$g^{(\alpha)} = g^{(\alpha)}(\gamma_a) \tag{3.17}$$

where

$$\gamma_a = \int_0^t \sum_\alpha \left| \dot{\gamma}^{(\alpha)} \right| dt \tag{3.18}$$

Thus, h_β is identical for each slip system.

The most elusive parameters in the constitutive law (3.9) are the elements of the hardening matrix $h_{\alpha\beta}$ in (3.14). Each component of $h_{\alpha\beta}$ depends on the deformation history. Further, the $h_{\alpha\beta}$ need only be homogeneous of degree zero in the shear rates; an increment of flow stress might as well depend nonlinearly on the increments of slip. In an FCC crystal there would be 144 elements to specify for a general monotonic deformation, and this number becomes 576 if reverse plastic straining is taken into account. Thus, in order to obtain a tractable description of crystal hardening, several simple forms for the hardening matrix have been assumed in the past. Calculations by Peirce et al. (1981) indicate however that the detailed description of latent hardening, even within the range suggested by the experiment, may be very important.

3.2.1 Single slip hardening laws

The simplest single slip hardening law takes the following power-law form for $h_{(\beta)}$:

$$h_{(\beta)}=h_0\left(\frac{h_0\gamma_a}{\tau_0 n}+1\right)^{n-1} \tag{3.19}$$

where h_0 is the initial hardening rate of the system, and n is the hardening exponent.

Based on measurements of strain hardening of single crystals of aluminium alloys by Chang and Asaro (1981), the following slip hardening function was used by Asaro and co-workers (e.g., Harren et al., 1989):

$$h_{(\beta)} = h_s + (h_0-h_s)\, sech^2\left\{\left(\frac{h_0-h_s}{\tau_s-\tau_0}\right)\gamma_a\right\} \tag{3.20}$$

where h_0 and h_s are the initial and asymptotic hardening rates. If h_s=0, then τ_s represents the saturation value of the shear stress.

Motivated by the work of Brown et al. (1989), Anand and co-workers (e.g., Kalidindi et al., 1992; Bronkhorst et al., 1992) have considered another power-law form of the hardening function h_β

$$h_{(\beta)}=h_0\left(1-\frac{g^{(\beta)}}{\tau_s}\right)^a \tag{3.21}$$

where h_0, a and τ_s are slip system hardening parameters which are taken to be identical for all slip systems. Unlike the Asaro (3.20) single slip hardening rate, $h_{(\beta)}$ in (3.21) is directly related to the current hardness g_β of the slip system.

As previously pointed out, the simple form for $h_{(\alpha\beta)}$ in (3.15) incorporates only a limited coupling between slip systems through off-diagonal components that scale by the latent hardening parameter q with the corresponding diagonal components. When viewed in terms of observations from uniaxial stressing of single crystals including an orientation dependence of hardening, secondary slips before overshoot and coarse slip band formation, the degree of latent hardening introduced in (3.15) appears to be too high. By reviewing reported experimental observations and reinterpreting latent hardening, Bassani and Wu (1991) proposed a particular multiplicative form in which each diagonal component is taken as the product of a self-hardening term h and an interactive hardening term G:

$$h_{(\alpha\alpha)} = h\left(\gamma^{(\alpha)}\right)G \text{ (no sum on } \alpha) \tag{3.22}$$

The hardening of system β due to slip on the system α is simply taken to be a fraction q of the active modulus, and the off-diagonal components are given by

$$h_{(\alpha\beta)}=qh_{(\alpha\alpha)}, \alpha\neq\beta \text{ (no sum on } \alpha) \tag{3.23}$$

It is clear that Asaro and co-workers as well as others have adopted a hardening description that is a special case of the form (3.22) where $G = 1$. A form for G that equals unity when its arguments are all zero and asymptotes to finite values when all slips $\gamma^{(\beta)}\ (\beta \neq \alpha)$ are large is (Bassani and Wu, 1991)

$$G = 1 + \sum_{\beta \neq \alpha} f_{\alpha\beta} \tanh\left(\frac{\gamma^{(\beta)}}{\gamma_0}\right), \tag{3.24}$$

where γ_0 represents the amount of slip after which a given interaction between slip system α and β reaches peak strength. Each $f_{\alpha\beta}$ represents the strength of the interaction and depends on the type of dislocation junction formed between slip systems α and β, which in turn, depends on the geometric relation between the two slip systems. For FCC crystals, Bassani and Wu (1991) classify $f_{\alpha\beta}$ into five groups. Table 2 in Bassani and Wu (1991) gives each value of $f_{\alpha\beta}$ while the corresponding notations for the slip systems and slip planes are given in their Table 1.

A simple form for the self-hardening $h\left(\gamma^{(\alpha)}\right)$ that gives a monotonically decreasing modulus at small strains and a finite rate of hardening at large γ_a is (Bassani and Wu, 1991)

$$h\left(\gamma^{(\alpha)}\right) = h_s + \left(h_0 - h_s\right) \operatorname{sech}^2\left\{\left(\frac{h_0 - h_s}{\tau_I - \tau_0}\right)\gamma_a\right\}, \tag{3.25}$$

where τ_0 is the initial critical resolved shear stress, τ_I is the so-called stage I stress and h_0 is the initial hardening rate, and h_s is assumed to depend on the total accumulated slip γ_a on all slip systems (Bassani, 1994):

$$h_s = h_s^I + \left(h_s^{III} - h_s^I\right) \tanh\left(\frac{\gamma_a}{\gamma_0^{III}}\right) \tag{3.26}$$

where h_s^I and h_s^{III} are the hardening rates during the stage I and III, respectively, and γ_0^{III} is approximately the accumulated slip at the onset of stage III. It is important to note, for applications to different loading histories (e.g. reverse loading), that the slip rates $\dot{\gamma}^{(\alpha)}$ in the present description in (3.8) – (3.15) can be either positive or negative (contrary to Bassani, 1994). Therefore, it is implied in the hardening laws (3.23) – (3.26) that γ_a is interpreted as the accumulated shear on the slip system i.e., $\int|\dot{\gamma}^{(\alpha)}|dt$. Then, also note that (3.25) is similar in form as (3.20), but a function of the accumulated shear of the slip system instead of the total accumulated shear.

3.3 Basic field equations

Many metal forming operations involve large inelastic deformations with severe nonlinear geometric effects. Although the mathematical formulation of these large-strain plasticity problems is now a reasonably straightforward matter (except sometimes for the difficulty of choosing appropriate constitutive laws), the solution of the governing equations is often a formidable task.

Numerical techniques are required for the majority of applications since it is generally not possible to obtain analytical mathematical solutions for problems involving complicated geometries, loadings, and material properties. Among these numerical techniques the finite element method offers a numerical means to solve the governing field equations. Finite element solutions are generally preferred for numerical analyses since they provide the most flexible means for achieving the degree of accuracy required for a given application. The basic formulation is usually in incremental or rate form to account for the large-strain history-dependent features of inelastic behaviour.

3.3.1 Principle of virtual work

In this study, a finite element procedure based on a large-strain Lagrangian formulation of the field equations using convected coordinates is employed (Neale, 1981; Needleman and

Tvergaard, 1984). The initial, undeformed configuration of the body, with volume V and surface S, is used as a reference. A material point is identified by the convected coordinates x_i in the reference configuration having base vectors $\boldsymbol{g}_i$ and corresponding metric tensor g_{ij} where

$$g_{ij} = \boldsymbol{g}_i \cdot \boldsymbol{g}_j, \; g^{ij} = \boldsymbol{g}^i \cdot \boldsymbol{g}^j \tag{3.27}$$

In the current configuration the base vectors are $\boldsymbol{G}_i = \boldsymbol{F}\,\boldsymbol{g}_i$ with metric tensor G_{ij} where

$$G_{ij} = \boldsymbol{G}_i \cdot \boldsymbol{G}_j, \; G^{ij} = \boldsymbol{G}^i \cdot \boldsymbol{G}^j \tag{3.28}$$

The displacement and velocity vectors with respect to the undeformed configuration can be written as

$$\begin{aligned} \boldsymbol{u} &= u_i\,\boldsymbol{g}^i = u^i\,\boldsymbol{g}_i \\ \dot{\boldsymbol{u}} &= \dot{u}_i\,\boldsymbol{g}^i = \dot{u}^i\,\boldsymbol{g}_i \end{aligned} \tag{3.29}$$

respectively. The Lagrangian strain tensor components with respect to the initial base vectors $\boldsymbol{g}^i$ are given by

$$\begin{aligned} \boldsymbol{\eta} &= \eta_{ij}\,\boldsymbol{g}^i\,\boldsymbol{g}^j \\ \eta_{ij} &= \tfrac{1}{2}(u_{i,j} + u_{j,i} + u^k_{,i} u_{k,j}) \end{aligned} \tag{3.30}$$

Here, a comma denotes covariant differentiation with respect to the undeformed metric. The strain rates $\dot{\eta}_{ij}$ are equal to the covariant Eulerian strain-rate components D_{ij} of $\boldsymbol{D}$ on the deformed base vectors $\boldsymbol{G}^i$ ($\boldsymbol{D} = D_{ij}\,\boldsymbol{G}^i\,\boldsymbol{G}^j$), but this correspondence does not hold for the respective contravariant components.

The Kirchhoff stress components τ^{ij} ($\boldsymbol{\tau} = \tau^{ij}\,\boldsymbol{G}_i\,\boldsymbol{G}_j$), conjugate to η_{ij}, are defined in terms of the Cauchy stress components with respect to the deformed base vectors, σ^{ij} ($\boldsymbol{\sigma} = \sigma^{ij}\,\boldsymbol{G}_i\,\boldsymbol{G}_j$), by

$$\tau^{ij}=(\det \boldsymbol{F})\sigma^{ij} \tag{3.31}$$

The nominal traction vector $\boldsymbol{T} = T^i\,\boldsymbol{g}_i$ on a surface element dS having unit normal $\boldsymbol{n} = n_i\,\boldsymbol{g}^i$ in the reference configuration has components

$$T^i=n_j(\tau^{ij}+\tau^{kj}u^i_{,k}) \tag{3.32}$$

We may now express the conditions of equilibrium in terms of the principle of virtual work (under quasi-static conditions) as

$$\int_V \tau^{ij}\delta\eta_{ij}dV = \int_S T^i\delta u_i dS \tag{3.33}$$

In the linear incremental formulation, we suppose the current state of equilibrium to be known at time t. To determine the equations for the field quantity rates, Equation (3.33) is expanded in a Taylor series about the time t to yield (Needleman and Tvergaard, 1984)

$$\int_V \left(\dot{\tau}^{ij}\delta\eta_{ij}+\tau^{ij}\dot{u}^k_{,i}\delta u_{k,j}\right)dV = \int_S \dot{T}^i\delta u_i dS - \left[\int_V \tau^{ij}\delta\eta_{ij}dV - \int_S T^i\delta u_i dS\right] \tag{3.34}$$

The term in brackets on the right side of Equation (3.34) serves as an equilibrium correction if equilibrium in the current state is only approximate.

3.4 Numerical analysis

In this section, we briefly present our finite element formulations (Inal, 1998), for both plane strain and plane stress assumptions, and the rate tangent modulus method that are used in our numerical analyses.

3.4.1 Finite element formulation

The basic finite element employed in both the plane stress and plane strain analyses is a four-node quadrilateral element, consisting of four "crossed" constant strain triangular sub-elements. In presenting results, the quadrilateral is regarded as the basic element, and when reporting values of the field quantities, the average value of the triangles is associated with the centroid of the quadrilateral.

3.4.1.1 Plane strain formulation

We first present the FE formulation for the plane strain case. The continuous displacement variable **u** is approximated in terms of its nodal values and shape functions as follows:

$$\mathbf{u} = \mathbf{N}\,\hat{\mathbf{u}} \tag{3.35}$$

where $\mathbf{N}$ is the matrix of the shape functions and $\hat{\mathbf{u}}$ is the vector of nodal displacements (in our formulation, 2 degrees of freedom are assigned per node). By introducing a $\mathbf{B}$ matrix which contains the partial derivatives of the displacements and the shape functions, the Lagrangian strain tensor defined in Equation (3.30) can be written as;

$$\eta = \mathbf{B}\,\hat{\mathbf{u}} \tag{3.36}$$

where

$$[\mathbf{B}] = \begin{bmatrix} (1+u_{,1}) & 0 & v_{,1} & 0 \\ 0 & u_{,2} & 0 & (1+v_{,2}) \\ u_{,2} & (1+u_{,1}) & (1+v_{,2}) & v_{,1} \end{bmatrix} \begin{bmatrix} N_{1,1} & 0 & N_{2,1} & 0 & N_{3,1} & 0 \\ N_{1,2} & 0 & N_{2,2} & 0 & N_{3,2} & 0 \\ 0 & N_{1,1} & 0 & N_{2,1} & 0 & N_{3,1} \\ 0 & N_{1,2} & 0 & N_{2,2} & 0 & N_{3,2} \end{bmatrix}$$

The left side of the virtual work Equation (3.34) can be written in matrix form as

$$\int_V \left(\dot{\tau}^{ij} \delta\eta_{ij} + \tau^{ij} \dot{u}^k_{,i} \delta u_{k,j} \right) dV = \int_v \delta\hat{\mathbf{u}}^T (\mathbf{B}^T \mathbf{L}\, \mathbf{B} + \mathbf{N}_\mathbf{d}^T \tau\, \mathbf{N}_\mathbf{d}) \dot{\hat{\mathbf{u}}}\, dV \tag{3.37}$$

since,

$$\dot{\tau}^{ij} \delta\eta_{ij} = \delta\hat{\mathbf{u}}^T \mathbf{B}^T \mathbf{L}\, \mathbf{B}\, \dot{\hat{\mathbf{u}}}$$

$$\dot{u}^i_{,k} \tau^{kj} \delta u_{i,j} = \delta\hat{\mathbf{u}}^T \mathbf{N}_\mathbf{d}^T \tau\, \mathbf{N}_\mathbf{d}\, \dot{\hat{\mathbf{u}}} \tag{3.38}$$

where

$$[\mathrm{N_d}] = \begin{bmatrix} N_{1,1} & 0 & N_{2,1} & 0 & N_{3,1} & 0 \\ N_{1,2} & 0 & N_{2,2} & 0 & N_{3,2} & 0 \\ 0 & N_{1,1} & 0 & N_{2,1} & 0 & N_{3,1} \\ 0 & N_{1,2} & 0 & N_{2,2} & 0 & N_{3,2} \end{bmatrix} \tag{3.39}$$

$$\begin{Bmatrix} \delta u^1_{,1} \\ \delta u^1_{,2} \\ \delta u^2_{,1} \\ \delta u^2_{,2} \end{Bmatrix} = \begin{bmatrix} N_{1,1} & 0 & N_{2,1} & 0 & N_{3,1} & 0 \\ N_{1,2} & 0 & N_{2,2} & 0 & N_{3,2} & 0 \\ 0 & N_{1,1} & 0 & N_{2,1} & 0 & N_{3,1} \\ 0 & N_{1,2} & 0 & N_{2,2} & 0 & N_{3,2} \end{bmatrix} \begin{Bmatrix} \delta u_1 \\ \delta v_1 \\ \delta u_2 \\ \delta v_2 \\ \delta u_3 \\ \delta v_3 \end{Bmatrix}$$

In Equation (3.37), $\mathbf{L}$ and τ represent the elastoplastic moduli and the Kirchhoff stress tensor respectively. Similarly, the right hand side of Equation (3.34) becomes

$$\int_S \dot{T}^i \delta u_i dS - \left[\int_V \tau^{ij} \delta\eta_{ij} dV - \int_S T^i \delta u_i dS \right] = \int_S \delta\mathbf{u}\, \dot{\mathbf{T}}\, dS - \left[\int_V \delta\mathbf{u}\, \mathbf{B}^T \tau\, dV - \int_S \delta\mathbf{u}\, \mathbf{T}\, dS \right] \tag{3.40}$$

Considering Equations (3.37) and (3.40), we can construct the global finite element equations in the form

$$\mathbf{K}\,\hat{\dot{\mathbf{u}}} = \dot{\mathbf{F}} \tag{3.41}$$

where the global stiffness matrix $\mathbf{K}$ and the vector $\dot{\mathbf{F}}$ become:

$$\mathbf{K} = \int_v (\mathbf{B}^T \mathbf{L}\,\mathbf{B} + \mathbf{N}_\mathbf{d}^T \tau\, \mathbf{N}_\mathbf{d})\, dV \tag{3.42}$$

$$\dot{\mathbf{F}} = \int_S \dot{\mathbf{T}}\, dS - \left[\int_V \mathbf{B}^T \tau\, dV - \int_S \mathbf{T}\, dS\right] \tag{3.43}$$

respectively.

The numerical solution of this system gives the rate of displacement of each node within the domain. Once the rate of displacement of all the nodes are known, the rates of deformation are calculated in each element. Furthermore, with the constitutive relations, the rates of stresses are obtained from the rates of deformation at each integration point within the solid. Following an update of all quantities, this procedure is repeated until the analysis is completed.

3.4.1.2 Plane stress formulation

A plane stress based FE code is developed by modifying the plane strain FE code presented in the previous section, without changing the general structure of the FE formulation. When modelling with the assumption of plane stress, the stress component in the normal direction (ND) of the sheet is taken as zero; i.e.,

$$\dot{\tau}^{33} = \mathrm{L}^{33kl}\, \dot{\eta}_{kl} = 0 \tag{3.44}$$

Thus, $\dot{\eta}_{33}$ can be written as;

$$\dot{\eta}_{33} = -\frac{L^{1133}}{L^{3333}}\dot{\eta}_{11} - \frac{L^{2233}}{L^{3333}}\dot{\eta}_{22} - 2\frac{L^{3312}}{L^{3333}}\dot{\eta}_{12} \tag{3.45}$$

In order to include the thickness strain into the formulation presented through Equations (3.36) – (3.43), we introduce a reduced constitutive moduli so that the rate of Kirchhoff stress tensor becomes

$$\begin{Bmatrix} \dot{\tau}^{11} \\ \dot{\tau}^{22} \\ \dot{\tau}^{12} \end{Bmatrix} = \begin{bmatrix} \mathcal{L}^{11} & \mathcal{L}^{12} & \mathcal{L}^{13} \\ \mathcal{L}^{21} & \mathcal{L}^{22} & \mathcal{L}^{23} \\ \mathcal{L}^{31} & \mathcal{L}^{32} & \mathcal{L}^{33} \end{bmatrix} \begin{Bmatrix} \dot{\eta}_{11} \\ \dot{\eta}_{22} \\ 2\dot{\eta}_{12} \end{Bmatrix} \tag{3.46}$$

where $\mathcal{L}^{ij}$ are called the so-called reduced moduli having as components

$$\begin{aligned}
\mathcal{L}^{11} &= L^{1111} - \frac{\left(L^{1133}\right)^2}{L^{3333}} \\
\mathcal{L}^{12} &= L^{1122} - \frac{L^{1133}\,L^{2233}}{L^{3333}} = L^{21} \\
\mathcal{L}^{22} &= L^{1122} - \frac{\left(L^{2233}\right)^2}{L^{3333}} \\
\mathcal{L}^{13} &= L^{1112} - \frac{L^{1133}\,L^{3312}}{L^{3333}} = L^{31} \\
\mathcal{L}^{33} &= L^{1212} - \frac{\left(L^{1233}\right)^2}{L^{3333}} \\
\mathcal{L}^{23} &= L^{2212} - \frac{L^{2233}\,L^{3312}}{L^{3333}} = L^{32}
\end{aligned} \tag{3.47}$$

3.4.2 Rate tangent modulus method

A direct implementation of the constitutive law (3.11) in the finite element code leads to an explicit Euler-time integration scheme which requires extremely small time steps to ensure numerical stability. In this study, we use the semi-implicit, forward-gradient time-integration procedure developed by Peirce et al. (1983, 1984).

Considering the slip-rate law expressed in Equation (3.13), the slip increment on system α at time t is given by

$$\Delta\gamma^{(\alpha)}=\gamma^{(\alpha)}(t+\Delta t)-\gamma^{(\alpha)}(t) \tag{3.48}$$

A linear interpolation is employed within the time increment to give

$$\Delta\gamma^{(\alpha)}=\left[(1-\theta)\dot{\gamma}^{(\alpha)}(t)+\theta\dot{\gamma}^{(\alpha)}_{(t+\Delta t)}\right]\Delta t \tag{3.49}$$

where Δt is the time increment. The parameter θ ranges from 0 to 1; $\theta=0$ corresponds to the simplest Euler integration procedure. A choice of θ between 0.5 and 1 is recommended (Pierce et al., 1984). Then the last term in Equation (3.49) can be obtained using a Taylor expansion as follows:

$$\dot{\gamma}^{(\alpha)}_{(t+\Delta t)}=\dot{\gamma}^{(\alpha)}_{t}+\left(\frac{\partial\dot{\gamma}^{(\alpha)}}{\partial\tau^{(\alpha)}}\Delta\tau^{(\alpha)}+\frac{\partial\dot{\gamma}^{(\alpha)}}{\partial g^{(\alpha)}}\Delta g^{(\alpha)}\right)_{t} \tag{3.50}$$

where $\Delta\tau^{(\alpha)}$ and $\Delta g^{(\alpha)}$ are the increments of the resolved shear stress and the current hardening in slip system α within the time increment Δt, respectively. Finally, the slip increments, according to Equation (3.49), can be expressed in terms of the quantities at time t as

$$\Delta\gamma^{(\alpha)}=(\dot{f}^{(\alpha)}+\mathbf{F}^{(\alpha)}:\boldsymbol{D})\Delta t \tag{3.51}$$

where

$$\dot{f}^{(\alpha)}=\sum_{\beta} M_{\alpha\beta}\dot{\gamma}_t^{(\alpha)}, \quad \mathbf{F}^{(\alpha)}=\sum_{\beta} M_{\alpha\beta}\mathbf{Q}^{(\alpha)}, \quad \mathbf{Q}^{(\alpha)}=\left(\frac{\theta\Delta t\dot{\gamma}_t^{(\alpha)}}{m\tau^{(\alpha)}}\right)\boldsymbol{R}^{(\alpha)} \tag{3.52}$$

Here $M_{\alpha\beta}$ is the inverse of matrix $N_{\alpha\beta}$ defined by

$$N_{\alpha\beta}=\delta_{\alpha\beta}+\left(\frac{\theta\Delta t\dot{\gamma}_t^{(\alpha)}}{m}\right)\mathrm{x}\left[\frac{\boldsymbol{R}^{(\alpha)}:\boldsymbol{P}^{(\beta)}}{\tau^{(\alpha)}}+\mathrm{sgn}(\tau^{(\beta)})\frac{h_{\alpha\beta}}{g^{(\alpha)}}\right] \tag{3.53}$$

It is important to mention that, for the rate-insensitive analysis, $N_{\alpha\beta}$ is not necessarily invertible. However, for any $m > 0$ a sufficiently small time step can be chosen so that $N_{\alpha\beta}$ is invertible. Thus, for rate-sensitive material behaviour a unique set of slip rates is always obtained for any prescribed strain rate.

From Equation (3.51), the constitutive Equation (3.11) can be rewritten as

$$\overset{\nabla}{\boldsymbol{\sigma}}=\mathbf{C}\,\boldsymbol{D}-\dot{\boldsymbol{\sigma}}^{0}-\boldsymbol{\sigma}\ \mathbf{tr}\,\boldsymbol{D} \tag{3.54}$$

where the moduli **C** are defined by

$$\mathbf{C}=\mathbf{L}-\sum_{\alpha}\boldsymbol{R}^{(\alpha)}\,\mathbf{F}^{(\alpha)} \tag{3.55}$$

and the viscoplastic type stress rate term (Equation (3.12)) becomes

$$\dot{\boldsymbol{\sigma}}^{\theta}=\sum_{\alpha}\boldsymbol{R}^{(\alpha)}\dot{f}^{(\alpha)} \tag{3.56}$$

3.5 Parallel Computing

The implementation of the crystal plasticity based constitutive law in the finite element modelling leads to significant demands in both computational power and storage, due to the necessity of tracking an enormous number of so-called internal state variables on the microscopic level. Classical sequential computations based on workstations, even on vector supercomputers, are generally unable to supply the computing power required for these applications. However, with the advent of high-speed computers and massive parallelization techniques, such demands are more easily met using parallel processing.

Parallel computers perform their calculations by concurrently executing different computational tasks on a number of processors. The processors within a parallel computer generally exchange information during the execution of the parallel code. This exchange of information occurs either in the form of explicit messages sent by one processor to another, or by different parallel processors sharing a specified common memory resource within the parallel computer.

The parallel computer used for our calculations is the IBM SP3 at the Université de Sherbrooke. It consists of 21 WinterHawk 2 nodes. Each node has 4 IBM POWER3 processors, and a total memory of 90 Gbytes is distributed amongst these processors. The parallel finite element formulations have been developed to be executed on this system.

In this section the parallel finite element formulation is presented briefly. The two main goals in the parallelization of a code are: (1) a decrease in CPU time for the simulations, and (2) code capacity enlargement. The Taylor-type polycrystal model is ideally suited for the parallelization of the computational procedures. A detailed parallel formulation to decrease CPU time was presented by Inal (1998) where simulations where performed with relatively less memory demanding applications (smaller than 1 Gbytes). For the applications considered in that work, CPU time was decreased significantly; the results were very close to the maximum values of the speed-up that can be achieved by parallel computing.

We now focus attention on parallelization for code capacity enlargement. The parallel algorithms used in our simulations are designed to distribute data (e.g., Beaudoin et al., 1993) on the microscopic level (crystal data) over the processors of the IBM SP3. To illustrate this, consider a simulation with a total number N of crystals (Fig. 3.2a). The global crystal data is distributed between the processors (Fig. 3.2b) such that each processor runs a part of the global program for N / A crystals where A is the total number of processors used in the simulation.

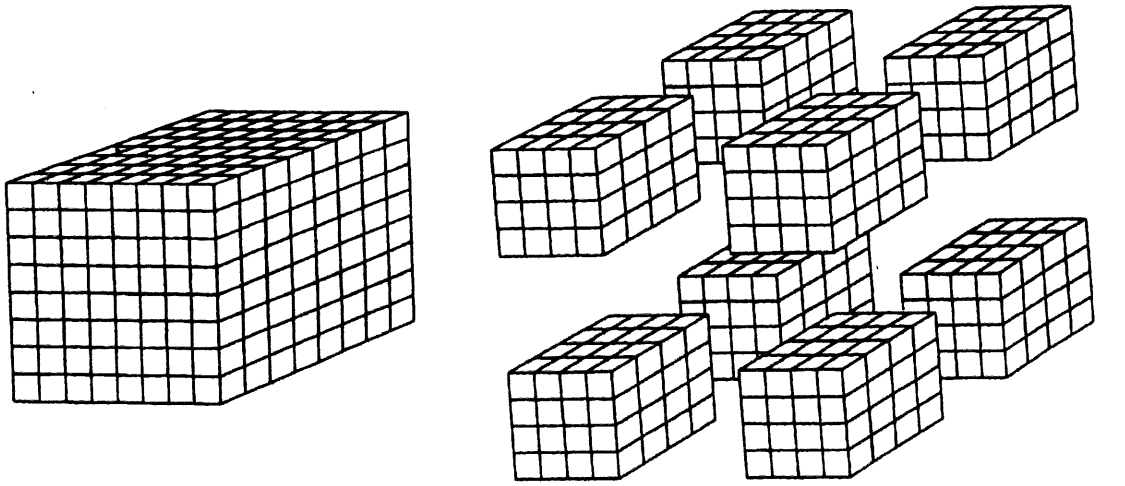

(a) (b)

Figure 3.2 (a) Polycrystal aggregate comprised of N crystals, (b) the distribution of this polycrystal aggregate between the processors

The macroscopic values of all quantities such as stresses, stress rates and elastic moduli are obtained by collective communication between the processors using the message passing interface (MPI) library. As a result, each processor has its own microscopic data; however, all of the processors have the same macroscopic data. We should mention that the total number of crystals should be distributed as evenly as possible between the processors. Otherwise the large difference in the number of crystals per processor affects the CPU time per processor, and blocking commands (which are costly in terms of CPU) are required during communication

between processors. To avoid this the parallel algorithms developed here distribute the crystals as evenly as possible among the available processors.

The above parallel data distribution enables us to perform simulations using the total memory of the IBM SP3. Furthermore, the subroutines which have been developed are scalable; that is, increasing the number of processors (corresponding to increasing the total memory) will proportionately decrease the memory required per processor.

CHAPTER 4

INSTABILITY AND LOCALIZED DEFORMATION IN FCC POLYCRYSTALS UNDER TENSION

4.1 Introduction

In the early stages of tensile straining, crystals of ductile pure metals and alloys exhibit deformation patterns which, on a macroscopic scale, are essentially homogeneous. With continued straining, however, the homogeneous deformation pattern is observed to give way to a non-homogeneous one, generally through the onset of diffuse necking and/or localized shearing. Failure usually ensues either by necking down to a "chisel edge" or by rupture within intense shear bands.

There are two main classes of material behaviour that have been employed for plastic instability predictions: the rate-insensitive and the rate-sensitive constitutive models. For a rate-insensitive solid, plastic instability occurs either as a bifurcation from a homogeneous state of stress and deformation, or as an imperfection-triggered localization. For rate-sensitive materials, bifurcation is effectively excluded, but small inhomogeneites (material and/or geometric) can still result in localization. In the limit of low material rate sensitivity, the localization strain predicted for a given initial inhomogeneity is practically identical to that predicted for the corresponding rate-insensitive solid, while for high rate sensitivity, localization is retarded considerably (Hutchinson and Neale, 1977).

Numerous analytical and numerical investigations have been carried out to investigate the onset of necking in metal bars under axial tension, both in terms of bifurcation theory and in terms of imperfection-sensitivity. For a one-dimensional model, Considére (1885) demonstrated that instability occurs at the maximum load point. Hutchinson and Miles (1974) have shown that the occurrence of necking at the maximum load point corresponds to the limit of a long, thin bar, whereas the first critical bifurcation in a more stubby specimen is delayed to a point somewhat after the maximum load. Also the subsequent localization of plastic flow in a neck, with a length of the order of magnitude of the diameter, has been predicted numerically (e.g., Needleman, 1972; Norris et al., 1978; Saje 1979).

In metal-forming problems involving thin sheets, the onset of localized necking is an important failure mode that limits the sheet formability. The concept of a forming limit diagram

(FLD), first introduced by Keeler (1961) from his investigation of plastic instability and fracture in sheets stretched over steel punches, has proved to be extremely useful for representing conditions for the onset of sheet necking. It is now a standard tool for characterizing materials in terms of their drawability.

Early calculations of forming limit diagrams were based on Hill's (1952) criterion for localized necking along a direction of zero-extension. In Hill's bifurcation analysis for rate-insensitive materials, J_2 flow theory was employed together with a power-law stress–strain relationship and smooth yield surface. His predictions only gave the critical strains between the uniaxial tension and plane strain states on the FLD. When the sheet is under biaxial stretching, Hill's direction of zero-extension does not exist.

An alternative plane stress analysis for sheet necking was presented by Marciniak and Kuczynski (1967) (referred to as the M-K analysis). In the M-K analysis, thickness imperfections are introduced normal to the principal stress and strain direction in the form of a groove to simulate pre-existing defects in the material. Necking was considered to occur when the ratio of the thickness in the groove to the nominal thickness was below a critical value. For this two-dimensional view to be appropriate, the length scale of the neck should be long compared to the sheet thickness but short compared to characteristic in-plane dimensions (Hutchinson et al., 1977).

Originally developed as a means of describing localized necking in biaxial stretching for which the minor strain $\varepsilon_{22} \geq 0$, the M-K analysis was later extended to the negative ε_{22} region (Stören and Rice, 1975; Hutchinson and Neale, 1978a; Chan et al., 1984). Furthermore, in Hutchinson and Neale's (1978a) work, the M-K model, which is based on the flow theory of plasticity framework and quadratic plastic potentials, was also refined by incorporating the J_2 deformation theory of plasticity.

Another extension, namely the inclusion of strain-rate effects in studies of sheet metal formability, was initially initiated by Marciniak et al. (1973). Similar analyses were carried out by Hutchinson and Neale (1978b) and Needleman and Tvergaard (1984) for rate-sensitive

materials. In these simulations, the effects of various constitutive features on localized sheet necking were explored.

It is well known that the localization of plastic flow is strongly influenced by deformation-induced textures and anisotropy (Asaro and Needleman, 1985). In turn, this localization then affects, to some degree, the texture development in polycrystals. Considering these factors, polycrystal deformation models can be expected to be very effective for simulating plastic instability processes. A polycrystal model should provide an improved understanding of the relation of localization to the microstructure of the material, and thus be more successful in predicting strain localization phenomena than phenomenological models.

Early applications of crystal plasticity concepts in instability analyses were presented by Bassani et al. (1979) and Barlat and co-workers (Barlat 1987, 1989; Barlat and Richmond, 1987). These researchers calculated a series of Bishop-Hill yield surfaces of polycrystals corresponding to various crystallographic textures. They used these yield surfaces rather than the conventional phenomenological ones to compute the corresponding FLDs and obtained results which were in good agreement with corresponding experimental observations (Lege et al., 1989) in certain cases. However, neither Bassani et al. (1979) nor Barlat and co-workers (Barlat 1987, 1989) have included the subsequent evolution of the yield surface during deformation. Furthermore none of these analyses included the effect of elasticity. Based on the simple M-K-type model, Asaro and Needleman (1985) presented analyses of localized necking in thin sheets subjected to equal biaxial stretching with their polycrystal model. Their work enabled, for the first time the study of the effects of texture and path-dependent strain hardening on sheet necking. Later on, Tvergaard and Needleman (1993) investigated the development of localized shear bands from an initial material inhomogeneity using the polycrystal model proposed by Asaro and Needleman (1985). They studied shear band formation in materials subjected to plane strain tension, biaxial stretching, and large strain shear. Zhou and Neale (1995) have directly applied a rate-sensitive crystal plasticity model in conjunction with the M-K approach to predict FLDs for annealed FCC sheet metals. Their analyses considered the initial texture and its evolution. However, elasticity was neglected and the imperfection groove was restricted to be normal to the major principal stretch direction. Wu et al. (1997) used the Asaro and Needleman (1985) polycrystal plasticity

model to calculate the FLDs for FCC polycrytals. They have discussed in detail the effects of initial imperfection intensity and orientation, initial distribution of grain orientations, crystal elasticity, strain rate sensitivity, single slip hardening, and latent hardening on the predicted FLDs.

It has already been mentioned that the initiation of a neck leads to localized deformation. With further stretching, either strain localizes progressively in this neck or necking triggers the formation of shear bands. In the mathematical description, the formation of localized shear bands in solids is quite similar to localized necking in sheets. However shear bands represent a material instability, and they do not depend on constraints along the boundary of the solid. Such material instabilities are of significance as a precursor to fracture, and have been observed in a wide variety of materials (Needleman and Tvergaard, 1992). The basic phenomenon of shear localization can be studied using a relatively simple approach similar to the above-mentioned M-K analysis where localized shearing is assumed to occur in a thin slice of material, while the strain fields outside this band are assumed to remain uniform throughout the deformation history.

Pierce et al. (1982) presented finite element calculations for nonuniform deformation modes in ductile single crystals, based on a rate-independent constitutive model for crystallographic slip. Their analysis, however, highlighted inherent limitations of the rate-independent idealisation of crystalline slip. These limitations were so severe that an analysis of large strain plastic flow was precluded for a full range of material properties, in particular for materials having high strain hardening. As a result, Pierce et al. (1983) adopted the rate-dependent constitutive theory for crystalline slip, and were able to simulate large strain tension tests of single crystals. Their results provided a general understanding of the roles of rate sensitivity and lattice kinematics in the development of localized modes of deformation.

More recently, Zikry and Nemat-Nasser (1990) have studied numerically the phenomenon of shear banding in an FCC single crystal undergoing plane-strain tensile deformations at high strain rates. They have demonstrated that shear band formation in single crystals, subjected to high rates of strain, is a function of the geometrical and thermal softening mechanisms of the

crystal. The problem of the initiation and growth of dynamic shear bands in a FCC single crystal deformed in simple compression was also investigated by Zhu and Batra (1993).

This chapter is dedicated to the investigation of tensile instabilities in FCC polycrystals using our polycrystal model-based finite element code. Numerical simulations of instabilities and localized deformations in the commercial aluminum sheet alloy AA3004-H19 under both plane strain tension and plane stress tension are carried out. The effects of various parameters on the formation of localized deformation are discussed in detail. The results of these investigations have been published in Inal et al. (2001a, 2001b). In an additional study (Inal et al., 2000), which will not be presented in this thesis, the plane stress FE code was employed to predict the angular variations (with respect to the rolling direction) of the R-value (the ratio of width-to-thickness strain under tensile loading) of this aluminum sheet alloy.

4.2 Instability and localized deformation in polycrystalline solids under plane strain tension

In this section, the plane strain finite element model which has been developed is employed to simulate localized deformation in polycrystals subjected to plane strain tension. Simulations are performed for a specimen with an initial thickness inhomogeneity. The effects of texture evolution, slip-rate sensitivity, and strain hardening on the nonuniform localization modes are investigated.

4.2.1 Problem formulation

A specimen subjected to tensile loading along the x_1-axis (Fig. 4.1) has been modelled under the assumption of plane strain conditions in the x_2 direction. The initial length of the specimen is 2 L_0 and its initial thickness is $2(h_0+\Delta h_0)$ where 2 h_0 is the average thickness and 2 Δh_0 is the initial thickness inhomogeneity. When the reference axes x_1 and x_3 are assumed to coincide with the rolling (RD) and normal (ND) directions of the sheet, respectively, the deformations can be considered symmetric about the central lines $x_1 = 0$ and $x_3 = 0$. Consequently, only one-quarter of the specimen needs to be considered in the numerical analysis.

The FE mesh consists of four-node quadrilateral elements, made up of four 'crossed' constant strain triangular sub-elements. In presenting results, the quadrilateral is regarded as the basic element and, when reporting values of the field quantities, the average value of the triangles is assigned to the centroid of the quadrilateral (Wu and Van der Giessen, 1996). A typical finite element mesh used in the simulations is shown in Fig. 4.1.

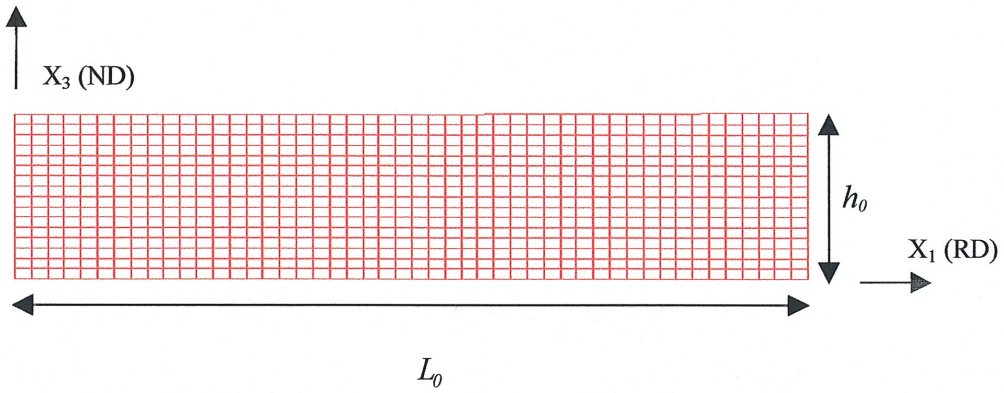

Figure 4.1 Finite element mesh used in simulations

With the tensile axis aligned in the x_1 direction, the boundary conditions become

$$u_3 = 0 \text{ along } x_3 = 0$$

$$u_1 = 0 \text{ along } x_1 = 0 \tag{4.1}$$

$$\dot{u}_1 = \text{V (applied velocity) along } x_1 = L_0$$

The end of the specimen, $x_1 = L_0$, is considered to be shear free.

The initial thickness imperfection Δh_0 is the same as that employed by Tvergaard et al. (1981), and is given by

$$\Delta h_0 = h_0 \left[-\xi_1 \cos\left(\pi x^2 / L_0\right) + \xi_2 \cos\left(p\pi x^2 / L_0\right) \right] \tag{4.2}$$

where ξ_1 and ξ_2 are prescribed imperfection amplitudes and $p(>1)$ is the wave number.

4.2.2 Results and discussion

The initial texture (represented by 380 crystals) of the aluminum sheet alloy AA3004-H19 is presented in Fig. 4.2 in terms of {111} stereographic pole figures for the x_1 - x_2 and x_1 - x_3 planes, respectively. Here x_1, x_2 and x_3 refer to the rolling, transverse and the normal directions of the sheet, respectively.

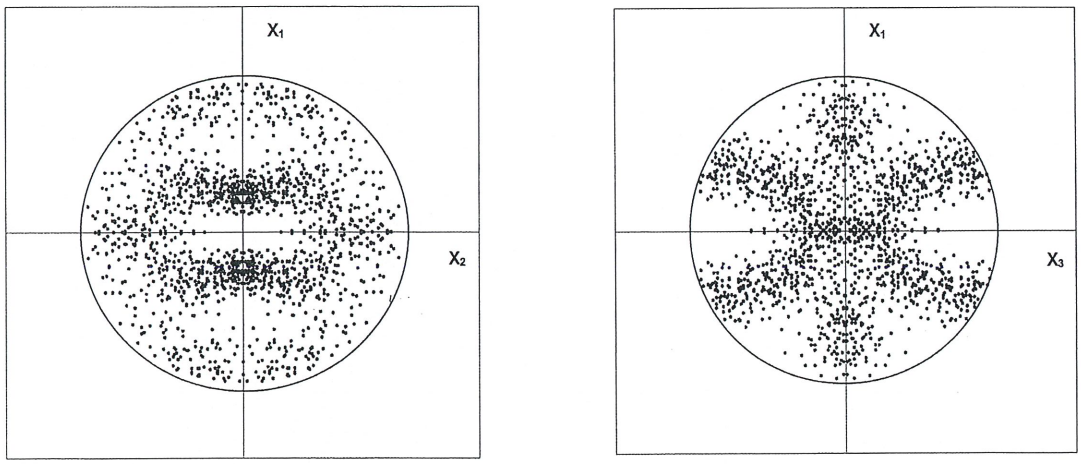

Figure 4.2 Initial texture of AA30004-H19 represented by {111} stereographic pole figure

The single slip hardening law proposed by Asaro and co-workers (3-20) is used in the simulations. The material constants in this law are as follows:

$$\tau_0 = 95 \text{ MPa},\ h_0/\tau_0 = 1.2,\ \tau_s/\tau_0 = 1.16,\ h_s/\tau_0 = 0,\ q = 1.0 \qquad (4.3)$$

These properties were obtained by fitting the uniaxial stress–strain curve obtained by the polycrystal plasticity simulation to the uniaxial stress–strain curve measured experimentally (Inal et al., 2000b). The slip system reference plastic shearing rate $\dot{\gamma}_0$ and the slip rate sensitivity parameter m are taken as $\dot{\gamma}_0 = 0.001 s^{-1}$ and m = 0.002, respectively, with the crystal elastic constants taken as C_{11} = 206 GPa, C_{12} = 118 GPa and C_{44} = 54 GPa.

The specimen is stretched under plane strain tension by applying the boundary conditions defined in (4.1). The initial aspect ratio of the specimen considered in this study is $L_0/h_0 = 3$ as in Tvergaard et al. (1981), and the finite element discretization is a 16 x 48 mesh, giving a total of 768 quadrilaterals (Fig. 4.1). The initial thickness imperfection is given by (4.2), with ξ_1=0.42 x 10^{-2}, ξ_2=0.24 x 10^{-2}, and a wave number $p = 2$.

The normalized nominal stress (σ_{NOM}/τ_0) – elongation (U/L_0) response is plotted in Fig. 4.3. This curve indicates that the normalized nominal stress reaches a maximum around U/L_0 = 0.055, and then starts to decrease. The deformation patterns at various normalized elongations are shown in Fig. 4.4. Figure 4.4a shows the deformed mesh after the maximum normalized nominal stress, at U/L_0 = 0.07, where a very light diffuse neck has formed. Evidence of the formation of shear bands that cross at the specimen centre can be observed in Fig. 4.4b, where U/L_0 = 0.10. These bands are more fully developed at U/L_0 = 0.13, as shown in Fig. 4.4c.

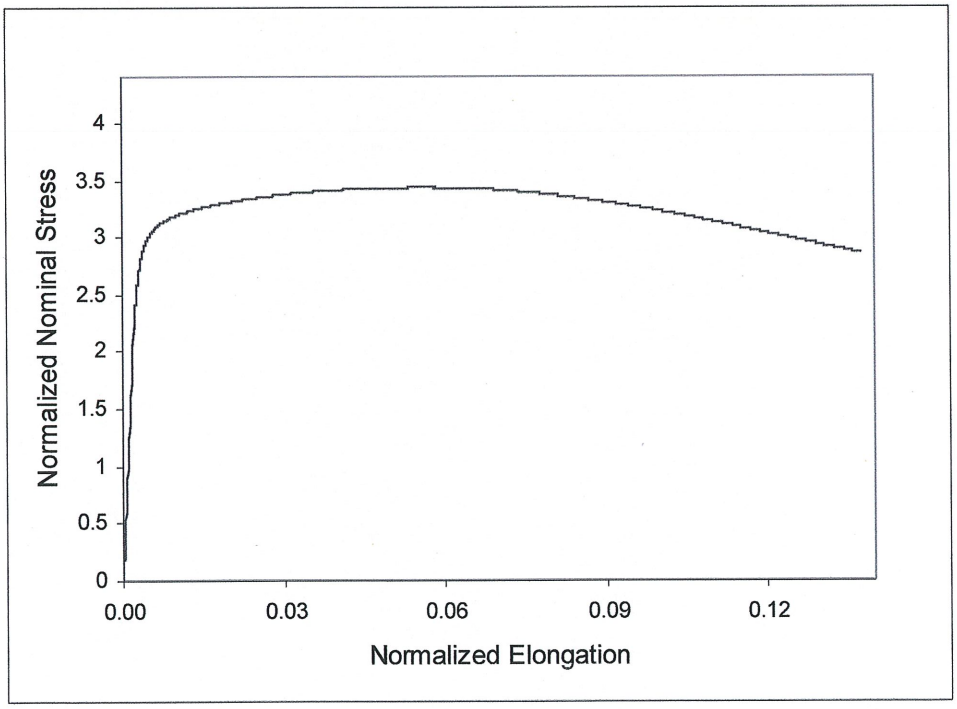

Figure 4.3 Normalized nominal stress – elongation curve

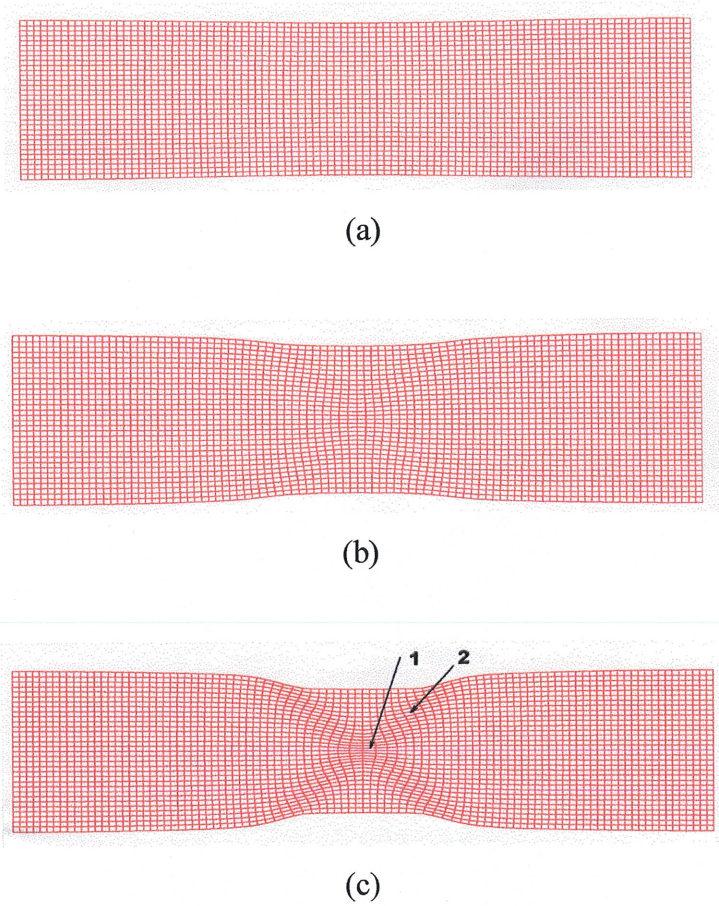

(a)

(b)

(c)

Figure 4.4 Deformed meshes at: (a) $U/L_0 = 0.07$, (b) $U/L_0 = 0.10$, and (c) $U/L_0 = 0.13$

A more quantitative representation of shear band development is presented in Fig. 4.5, where contours of true strain ε_{11} are plotted at various deformation stages. Figure 4.5a corresponds to Fig. 4.4a, where $U/L_0 = 0.07$. Although the strain pattern is slightly nonuniform, an inhomogeneity corresponding to the early stages of necking can be observed since the highest strains are at the specimen centre. A shear band pattern is evident in Fig. 4.5b, which shows contour plots at $U/L_0 = 0.10$. Although little additional straining has occurred towards the end of the specimen as compared to Fig. 4.5a, strain has begun to concentrate in a well-defined band (represented by the 0.21 contour) nearer the centre of the specimen. Figure 4.5c shows the fully developed shear band at $U/L_0 = 0.13$. The strains in the shear band exceed 0.4 although the

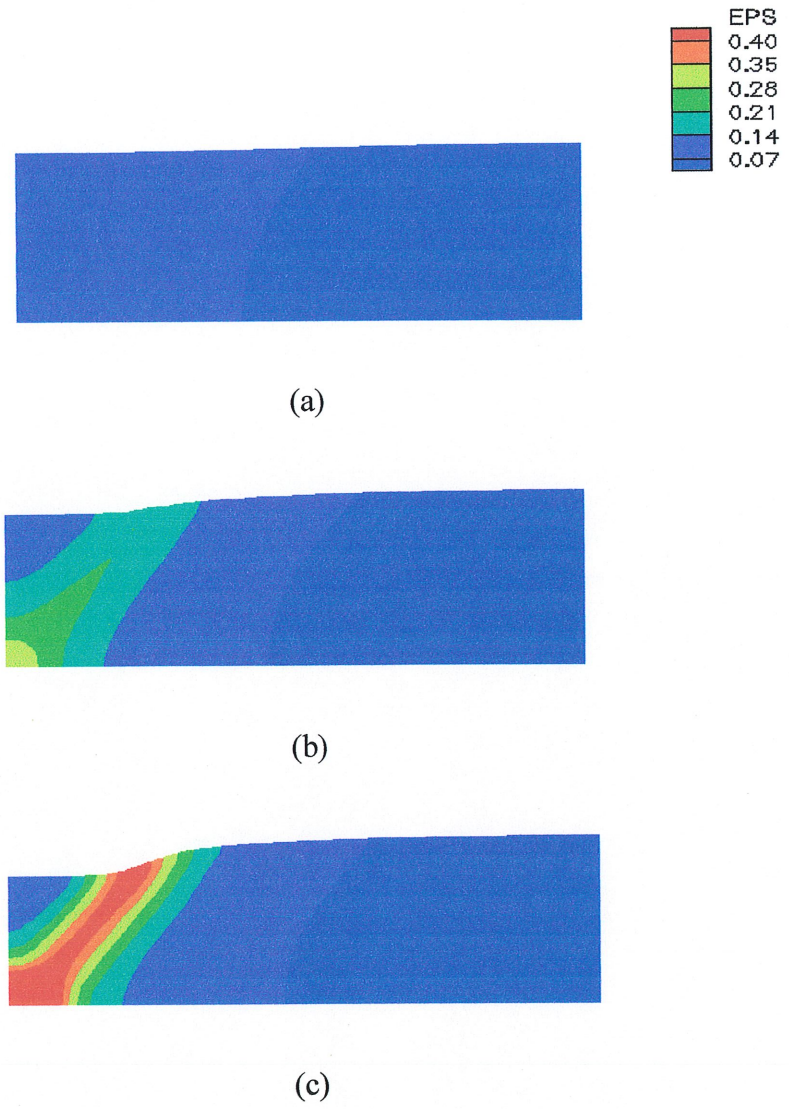

Figure 4.5 True strain ε_{11} at: (a) $U/L_0 = 0.07$, (b) $U/L_0 = 0.10$, and (c) $U/L_0 = 0.13$

overall normalized extension is $U/L_0 = 0.13$. While there is very little deformation occurring outside the band, a large amount of shear is accumulating within the well-defined shear band (represented by the 0.4 contour).

4.2.2.1 The effect of texture evolution

To investigate the effect of texture evolution on the localization modes, the simulation described above has been carried out once more, but with texture evolution excluded from the polycrystal model. Thus, the stretching and rotation of the lattice vectors ($\boldsymbol{s}^{*(\alpha)}$, $\boldsymbol{b}^{*(\alpha)}$) according to

Equation (3.4) are excluded in the analysis. From now on, the model including texture evolution will be referred to as ITE, and the model excluding texture evolution will be referred to as ETE. Figure 4.6 shows that the normalized nominal stress – elongation curves for the two models start to differ after the maximum normalized nominal stress is attained. In the ITE model, the nominal stress drops more rapidly than that obtained with the ETE model.

The importance of including texture evolution can be seen by comparing Fig. 4.4c to the deformed mesh of Fig. 4.7, which is the result from the ETE simulation at $U/L_0 = 0.13$. As discussed earlier, shear bands are fully developed at this stage of the simulation with the ITE model. However, there are no shear bands formed with the ETE model, although the initiation of necking is visible. With further loading, strain localizes progressively in the neck area without any formation of shear bands. Pierce et al. (1982) have shown that, for single crystals, necking causes nonuniform lattice rotations and "geometrical softening" that lead to localized shearing. In their work, they refer to "geometrical softening" as the increase in the resolved shear stress on the

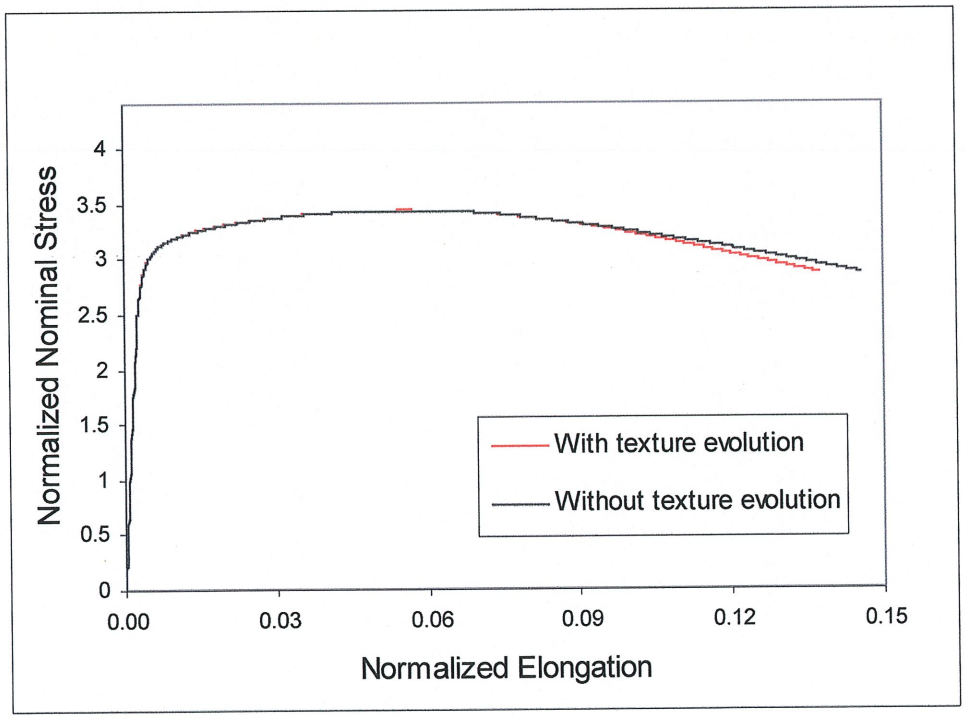

Figure 4.6 Comparison between the normalized nominal stress – elongation curves for simulations with and without texture evolution

slip system responsible for the concentrated straining due to its rotation with respect to the loading direction. We shall adopt this terminology. As the ETE model does not include texture evolution, necking cannot induce the necessary lattice rotations that produce "geometrical softening". As a result, although a neck is formed, it cannot act as a triggering mechanism for shear localization in the form of a band.

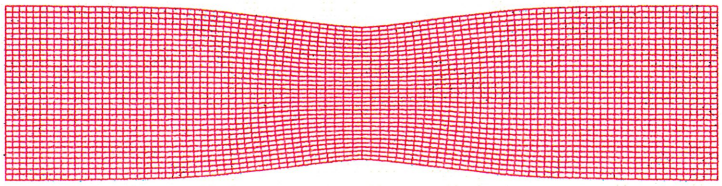

Figure 4.7 Deformed mesh at $U/L_0 = 0.13$ for the case where texture evolution is excluded

A comparison between the texture evolutions at the centre of the specimen and at the end of the specimen (away from the neck) are shown in Figs. 4.8 and 4.9 where the pole figures relative to the rolling (x_1) and transverse (x_2) directions are given for points at the end and at the centre of the specimen, respectively. Figures 4.8a and 4.8b correspond to the deformation shown

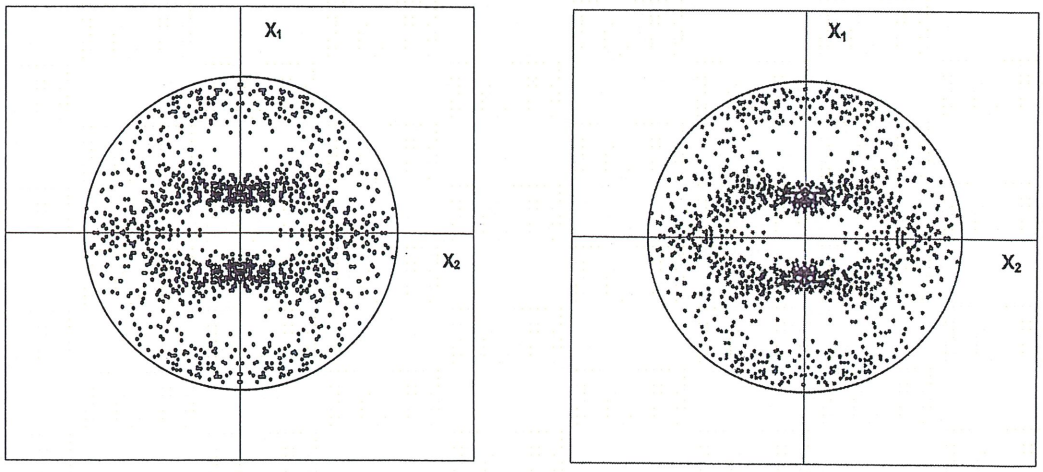

(a) (b)

Figure 4.8 Texture evolution for $U/L_0 = 0.07$ at: (a) the end of the specimen, and (b) at the centre of the specimen

in Fig. 4.4a ($U/L_0 = 0.07$), and they indicate that the initial texture (Fig. 4.2) has evolved slightly. Note that texture evolution at the end and at the centre of the specimen are very similar at this elongation. By contrast, Figs. 4.9a and 4.9b (corresponding to Fig. 4.4c and $U/L_0 = 0.13$) show that, in the shear band, the texture has become much sharper than that at the end of the specimen.

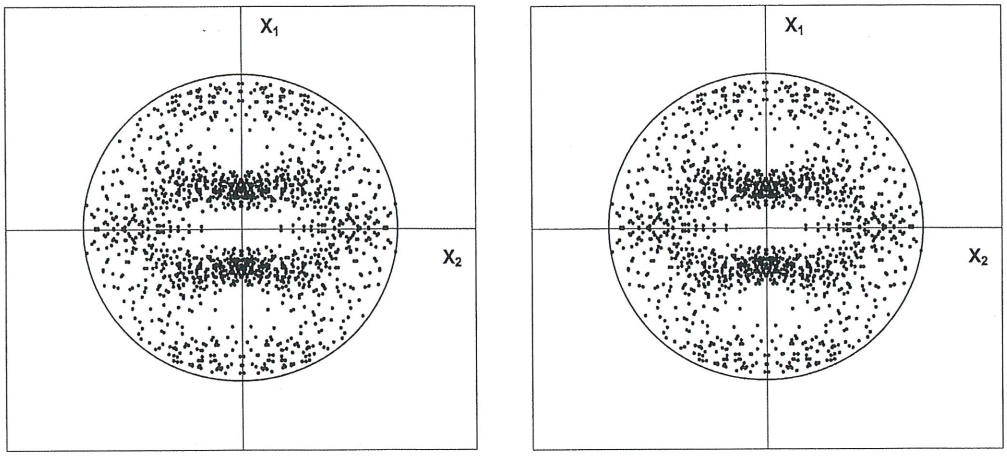

(a) (b)

Figure 4.9 Texture evolution for $U/L_0 = 0.13$ at: (a) the end of the specimen, and (b) at the centre of the specimen

Next the texture evolution at two different elements in the shear band (elements 1and 2 identified in Fig. 4.4c) are compared. Figures 4.10 a-b present pole figures related to the rolling (x_1) and normal (x_3) directions for these when $U/L_0 = 0.13$. The differences between these two textures suggest that the deformation modes are different at the two elements selected. Element 1 is undergoing tensile stretching, while element 2 is experiencing both shearing and tensile stretching.

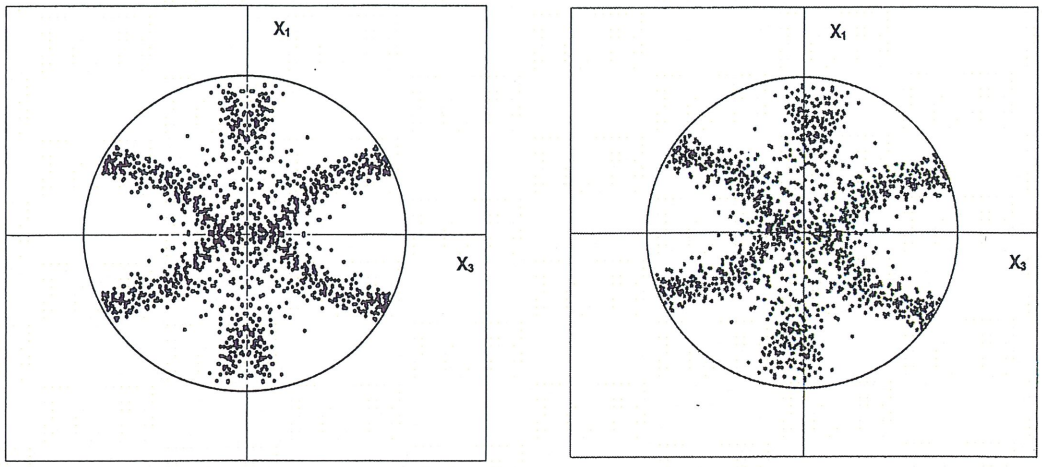

(a) (b)

Figure 4.10 Texture evolution for $U/L_0 = 0.13$ at elements: (a)1, and (b) 2

4.2.2.2 The effect of slip rate sensitivity *m*

The effect of slip rate sensitivity m on the constitutive response is investigated by comparing simulations with $m = 0.002$, 0.01 and 0.02, respectively. Figure 4.11 compares the

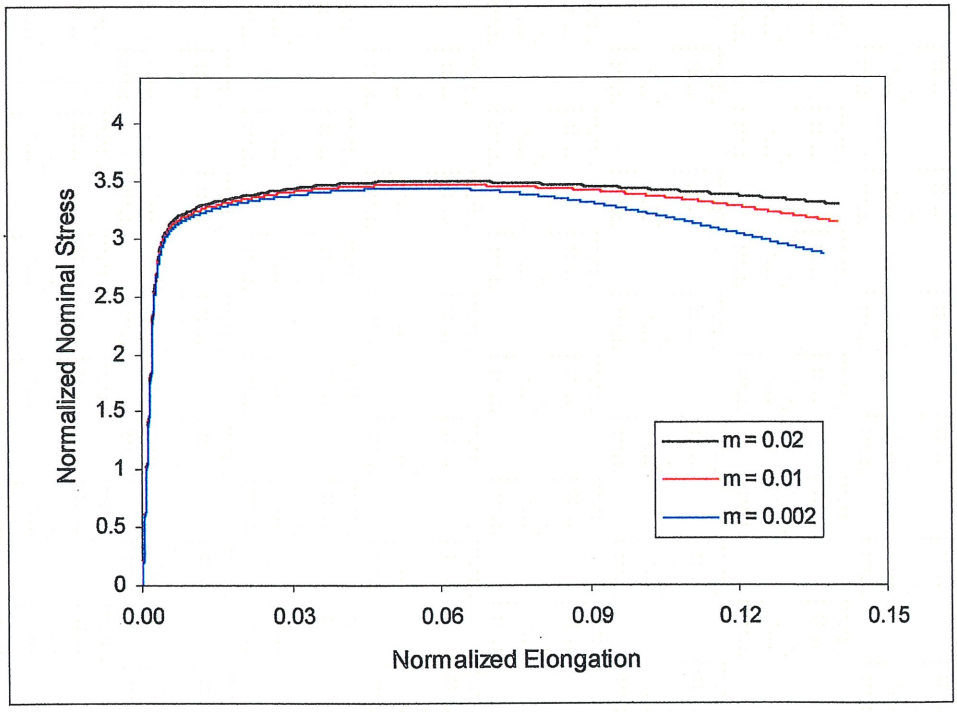

Figure 4.11 Normalized nominal stress – elongation curves for various values of the rate sensitivity m

normalized nominal stress–elongation curves for these simulations. It can be seen that, as expected, the normalized nominal stress response increases with increasing m value. It is also observed that, as m increases, the nominal stress falls less rapidly in the later stages of deformation. In Fig. 4.12 the deformed meshes are presented for the simulation where the rate sensitivity m is taken as 0.02. The normalized extension in Fig. 4.12a is $U/L_0 = 0.11$, and the deformation pattern is quite uniform. Evidence of the initiation of necking can be seen in Fig. 4.12b where $U/L_0 = 0.16$. In Fig. 4.12c, where $U/L_0 = 0.23$, the neck is clearly visible. Recall that, shear bands were fully developed at $U/L_0 = 0.13$ (Fig. 4.4c). However, there is no evidence of shear band formation when the strain rate sensitivity m was taken as 0.02.

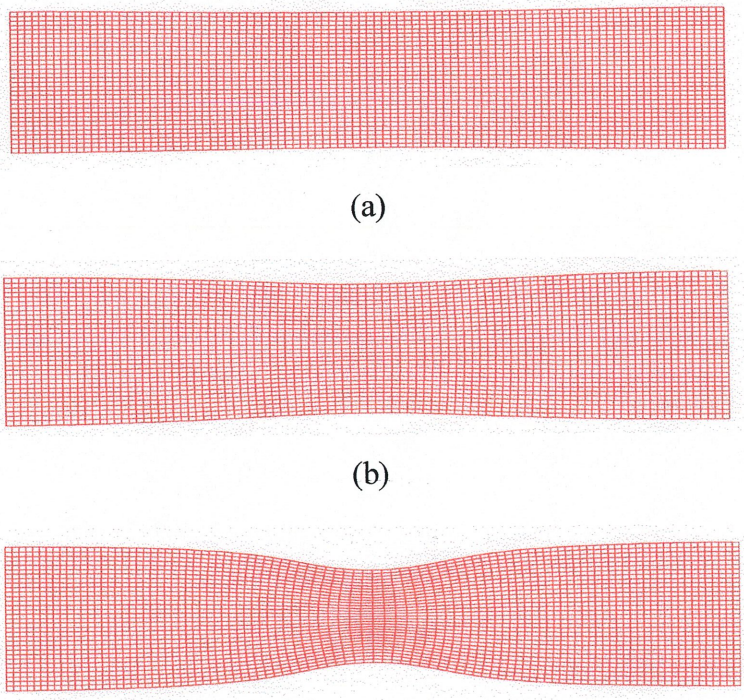

(a)

(b)

(c)

Figure 4.12 Deformed meshes for the case where $m = 0.02$ at: (a) $U/L_0 = 0.11$, (b) $U/L_0 = 0.16$ and (c) $U/L_0 = 0.23$

The above results show that, when the rate sensitivity is increased, not only does the ductility of the metal increase, but that, the localization mode can change from shear bands to

necking if the m value is sufficiently high. This change in the mode of localization was an expected result considering the results of Section 4.2.2.1 where the importance of texture evolution on the development of shear bands was clearly demonstrated. Previous studies (Canova et al., 1988) have shown that the rate of texture evolution in tension is decreased by an increase in the slip rate sensitivity. Harren et al. (1989) have shown for simple shear that, when the strain rate sensitivity m was high enough (0.5 for their material), there was almost no tendency for textures to form. This can be explained by the near vanishing with increasing m of the plastic spin Ω^p defined in the second part of Equation (3.5). In our simulations, the evolution of texture does not vanish completely when m is taken as 0.02, but the "geometric softening" produced by this texture evolution is not sufficiently high to trigger shear band formation.

In Fig. 4.13 the normalized stress σ/σ_{MAX} is plotted as a function of the normalized elongation. Here, σ_{MAX} refers to the maximum of the physical component of the true stress (in the loading direction) calculated at the end section of the specimen, $x_1 = L_0$. It can be seen that

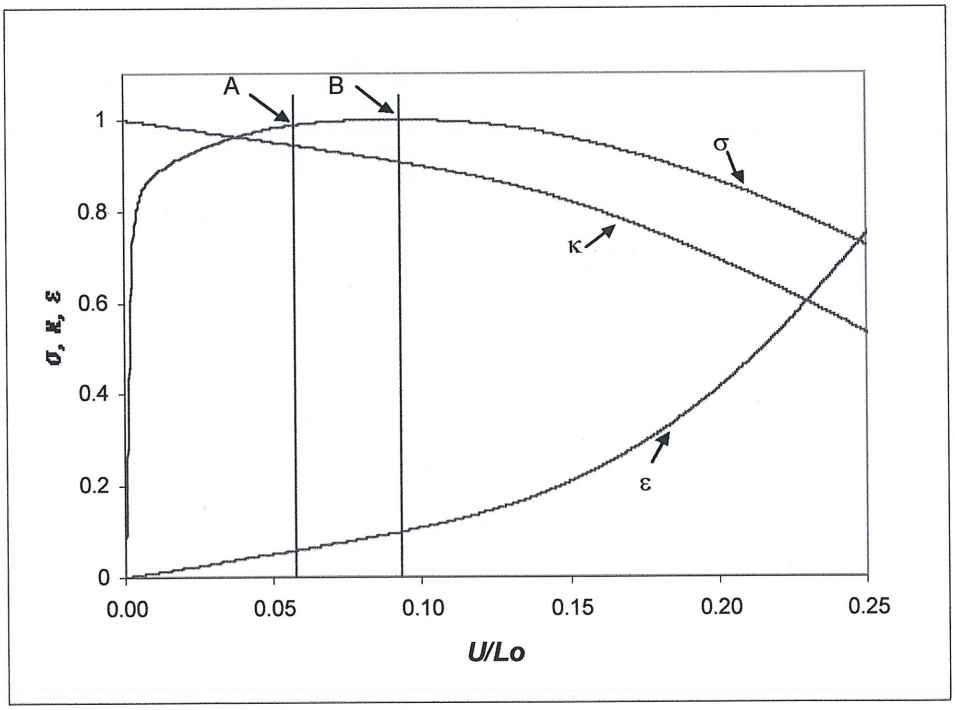

Figure 4.13 The evolution of neck section area κ, the true strain ε_{11} (at the centre of the specimen) and the true stress σ_{11} (at the end of the specimen)

σ reaches a maximum around $U/L_0 = 0.09$ (point B) and then begins to decrease. The normalized elongation ($U/L_0 = 0.058$) where the maximum nominal stress is attained is represented by point A.

The evolution of the neck-section area κ (where $\kappa = A_N/A_0$ calculated along the centre of the specimen, $x_1 = 0$) together with the true strain ε_{11} (in the rolling direction) at the centre of the specimen are also shown in Fig. 4.13. These curves show that the attainment of the maximum stress at $U/L_0 = 0.09$ identifies the onset of diffuse necking, and beyond this elongation the strain ε_{11} begins to increase rapidly thus signifying localization. This conclusion was also reached for other simulations based on phenomenological constitutive laws of plasticity (e.g., Tugcu and Neale, 1988; Tugcu, 1991), where it was shown that the attainment of the maximum stress at the end of a round tensile specimen identified the onset of necking.

4.2.2.3 The effect of strain hardening

The effect of strain hardening on the formation of shear bands is investigated by comparing the results obtained from simulations with three different values of asymptotic hardening rates: $h_s/\tau_0 = 0$, $h_s/\tau_0 = 0.02$ and $h_s/\tau_0 = 0.2$. Figure 4.14 depicts the true stress – true strain curves (for a specimen without imperfection) for these three cases. It can be seen that when $h_s/\tau_0 > 0$ there is strain hardening, while for $h_s/\tau_0 = 0$ there is saturation.

The normalized nominal stress – elongation curves for these 3 cases are compared in Fig. 4.15. The only difference in the normalized nominal stress – elongation curves for the simulations with $h_s/\tau_0 = 0$ and $h_s/\tau_0 = 0.02$ is that the normalized nominal stress drops more rapidly when $h_s/\tau_0 = 0$. Nevertheless, shear bands are still predicted for both cases. However, no shear bands are predicted when the strain hardening rate is taken relatively high ($h_s/\tau_0 = 0.2$), where the specimen deforms by the strain localizing progressively in the neck.

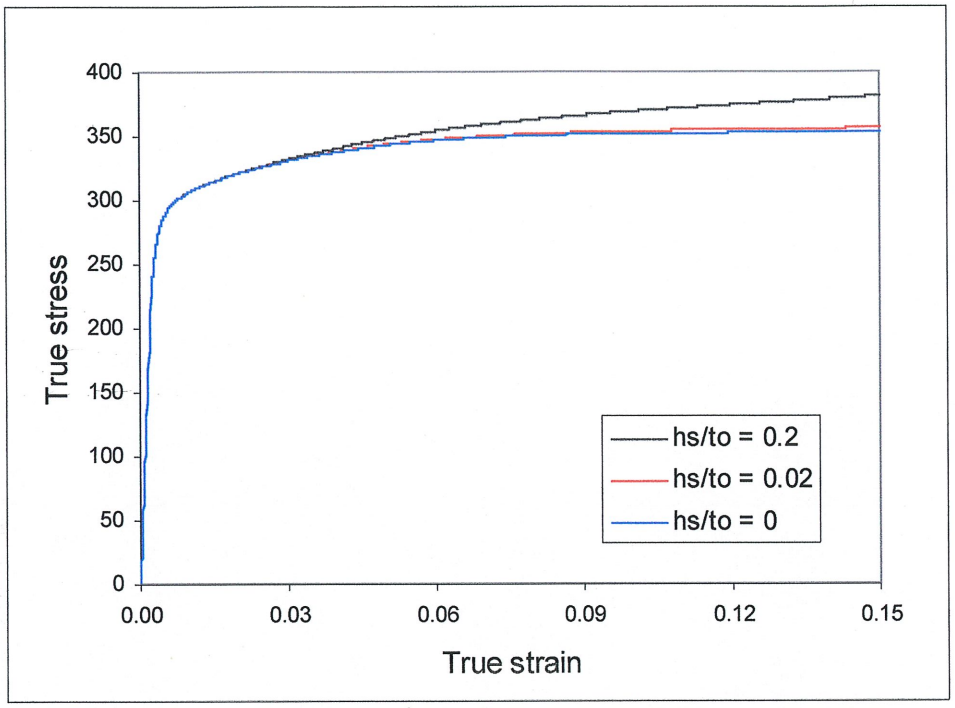

Figure 4.14 True stress–strain curves for various asymptotic hardening rates

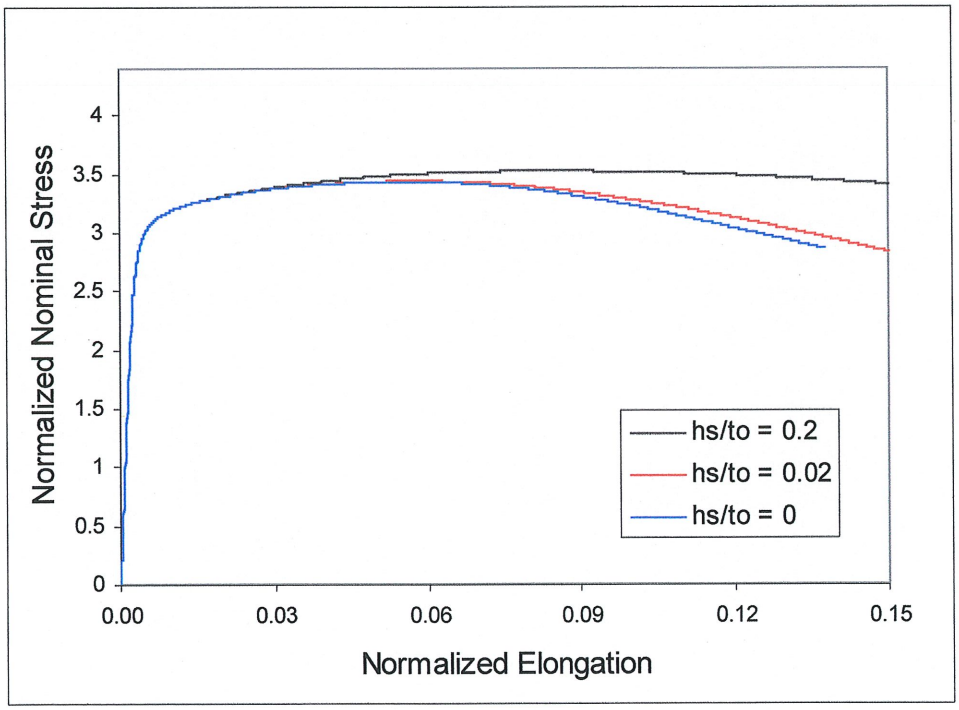

Figure 4.15 Normalized nominal stress–elongation curves for various asymptotic hardening rates

4.3 Instability and localized deformation in polycrystalline solids under plane stress tension

In this section, the plane stress finite element model that has been developed is employed to simulate localized deformation in polycrystalline sheets. Simulations are performed with a specimen without any initial inhomogeneity. The so-called "built-in" boundary conditions at the ends of the specimen are applied, and the resulting inhomogeneous behaviour eventually initiates localized deformation. Simulations are performed for specimens rotated such that the rolling direction is at 0°, 1°, 45° and 90° to the tensile axis. The onset of both necking and shear banding are investigated.

4.3.1 Problem formulation

A specimen subjected to tension along the x_1-axis (Fig. 4.16) has been modelled under the assumption of plane stress conditions. It is assumed that $D_{13} = D_{23} = W_{13} = W_{23} = 0$, where W_{13} and W_{23} are the components of the skew symmetric spin tensor. D_{33} is determined from the condition that the average stress component $\dot{\sigma}_{33} = 0$. For the orthotropic texture considered, these conditions imply that the average stress components $\sigma_{13} = \sigma_{23} = 0$.

When x_1 and x_2 are assumed to coincide with the rolling and transverse directions of the sheet, respectively, deformations can be considered symmetric about the central lines $x_1 = 0$ and $x_2 = 0$. In such cases (e.g., 0° and 90° oriented specimens) only one-quarter of the specimen is considered in the numerical solutions, as shown in Fig. 4.16. With the tensile axis aligned in the x_1 direction, the so called "built-in" boundary conditions on the quadrant are

$$\begin{aligned} u_2 &= 0 \text{ along } x_2 = 0 \\ u_1 &= 0 \text{ along } x_1 = 0 \\ u_2 &= 0 \text{ along } x_1 = L_0 \\ \dot{u}_1 &= \text{V (applied velocity) along } x_1 = L_0 \end{aligned} \tag{4.4}$$

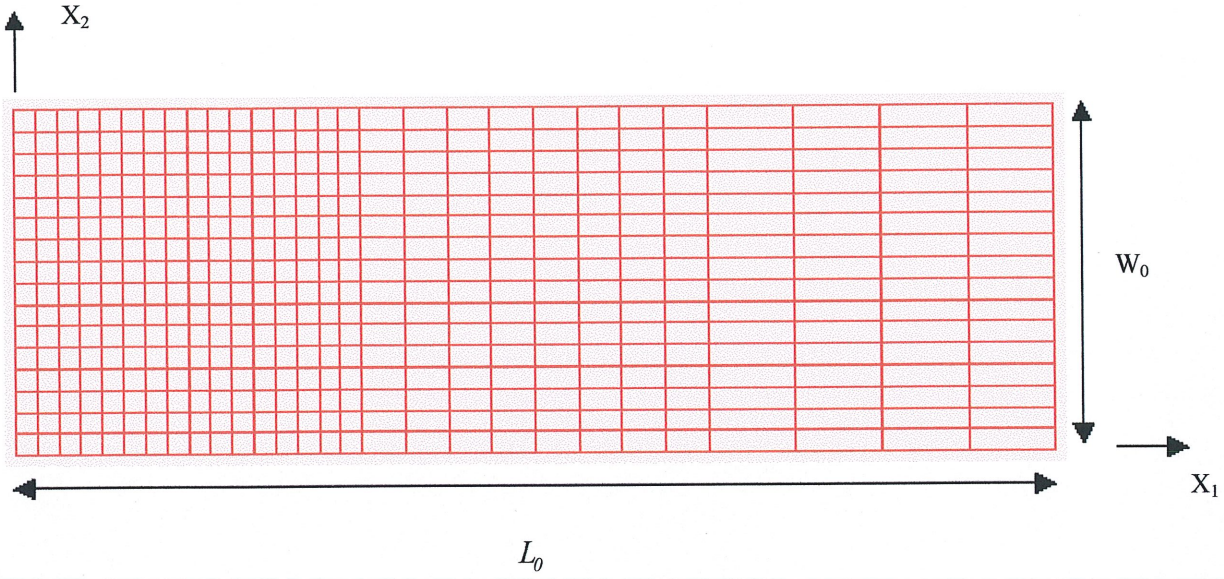

Figure 4.16 Finite element mesh used in 0 and 90 degrees rotated specimen simulations

Thus, the end of the specimen, $x_1 = L_0$, in this case is not shear free.

Specimens where the RD is oriented at 1° and 45° with respect to the tensile axis are also considered. For these cases the assumption of orthotropic material symmetry is no longer valid, and the entire specimen has to be modelled in the numerical analysis. The finite element mesh used to model the entire specimen is presented in Fig. 4.17. The boundary conditions for simulations with the full mesh are:

$$u_2 = 0 \text{ along } x_1 = \pm L_0$$

$$\dot{u}_1 = \text{V (applied velocity) along } x_1 = L_0 \qquad (4.5)$$

$$\dot{u}_1 = \text{-V (applied velocity) along } x_1 = -L_0$$

Again, the ends of the specimen, $x_1 = \pm L_0$, are not shear free.

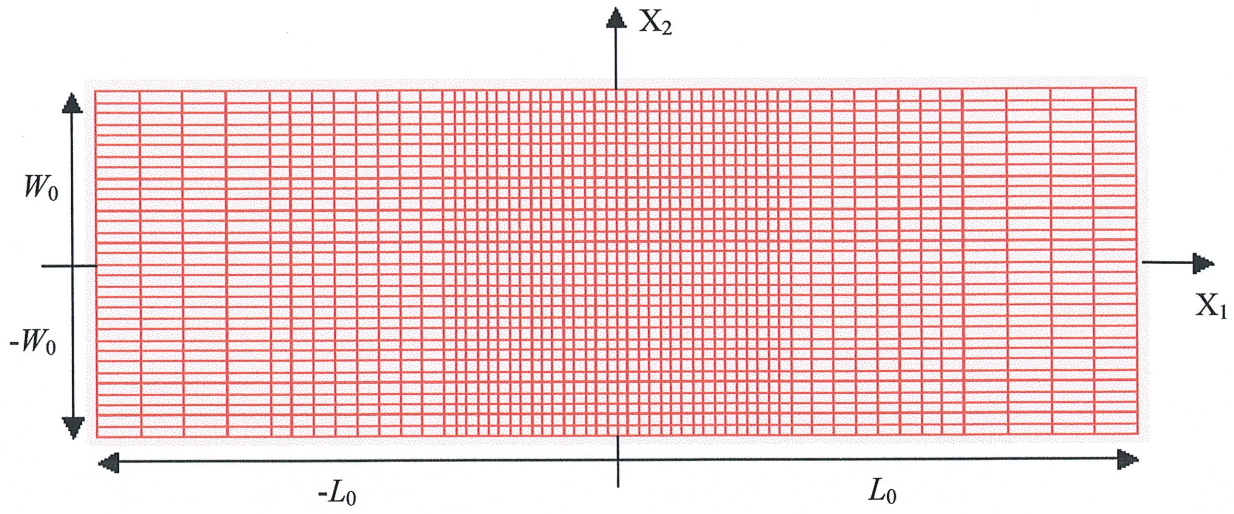

Figure 4.17 Finite element mesh used in 1 and 45 degrees rotated specimens

4.3.2 Results and discussion

The initial texture for the aluminum alloy AA3004-H19 as presented in Fig. 4.2 and the material properties for the single slip hardening law (3-20) are as specified by Equation (4.3). The slip system reference plastic shearing rate $\dot{\gamma}_0$ and the slip rate sensitivity parameter m are taken as $\dot{\gamma}_0 = 0.001\text{s}^{-1}$ and m = 0.002, respectively. The initial geometry of the specimen is such that $L_0/W_0 = 3$, and this value is used for all simulations presented in this section.

4.3.2.1 A typical result

A comparison between the simulated and experimental true stress–strain curves for uniaxial tension in the RD is presented in Fig. 4.18. It can be seen that the FE simulation is in reasonably good agreement with the experimental curve. The failure strain has been over-predicted by our simulation, but this is an obvious result since the simulation is carried out without any initial imperfection. Also, the crystal plasticity model employed in this study does not account for microscopic defects, such as voids, which will possibly influence the failure strain.

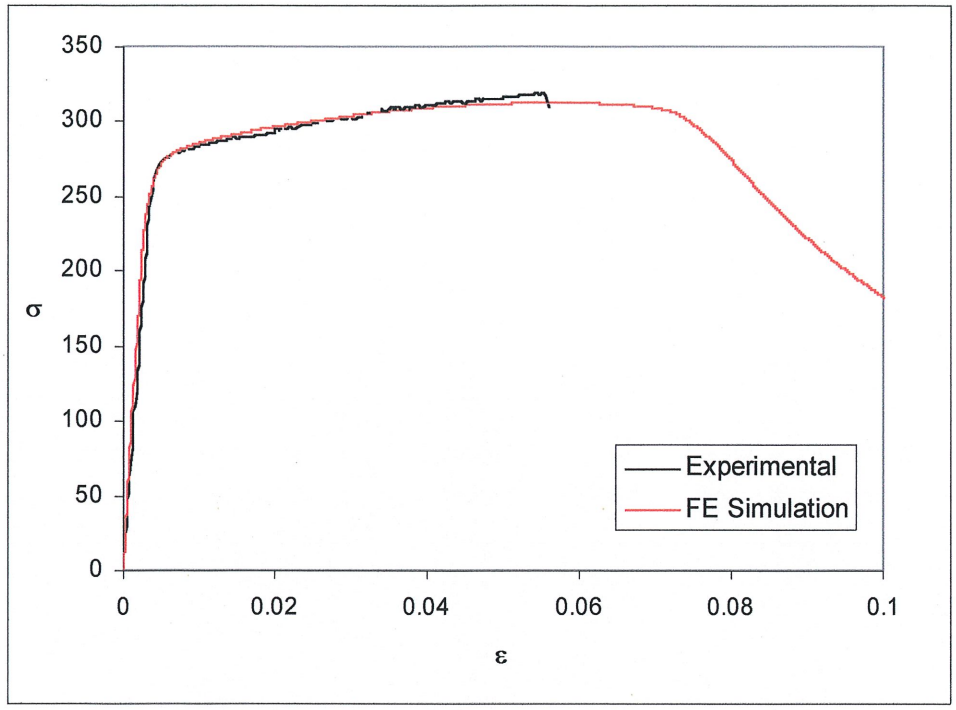

Figure 4.18 True stress–strain curves in RD

4.3.2.2 Mesh sensitivity

Shear band localization phenomena are notorious for sometimes exhibiting a pathological mesh sensitivity. However, as demonstrated by Needleman (1988), this is not necessarily the case for our type of simulations where the inherent mesh sensitivity with a rate-independent theory can be eliminated by a rate-dependent formulation such as the one used in this study. Nevertheless, the selection of a proper mesh does require attention. Figures 4.19 a-c show the three different finite element meshes used in this study with 288, 448 and 864 elements respectively.

The numerical studies show that the overall stress–strain curves for all three meshes are nearly identical for strain hardening and saturation (Fig. 4.20). Once softening occurs, the finer meshes demonstrate a stronger softening effect. Figure 4.21 illustrates the contours of true strain (in the loading direction) at an elongation of U/L_0=0.10 for the three meshes considered. These

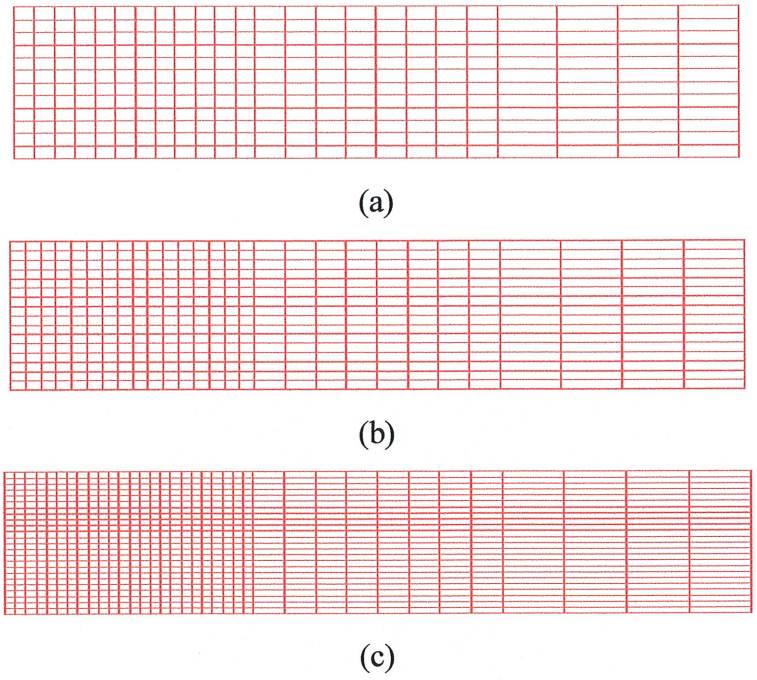

Figure 4.19 Initial meshes used in the mesh sensitivity analysis: (a) 288, (b) 448, and c) 864 elements

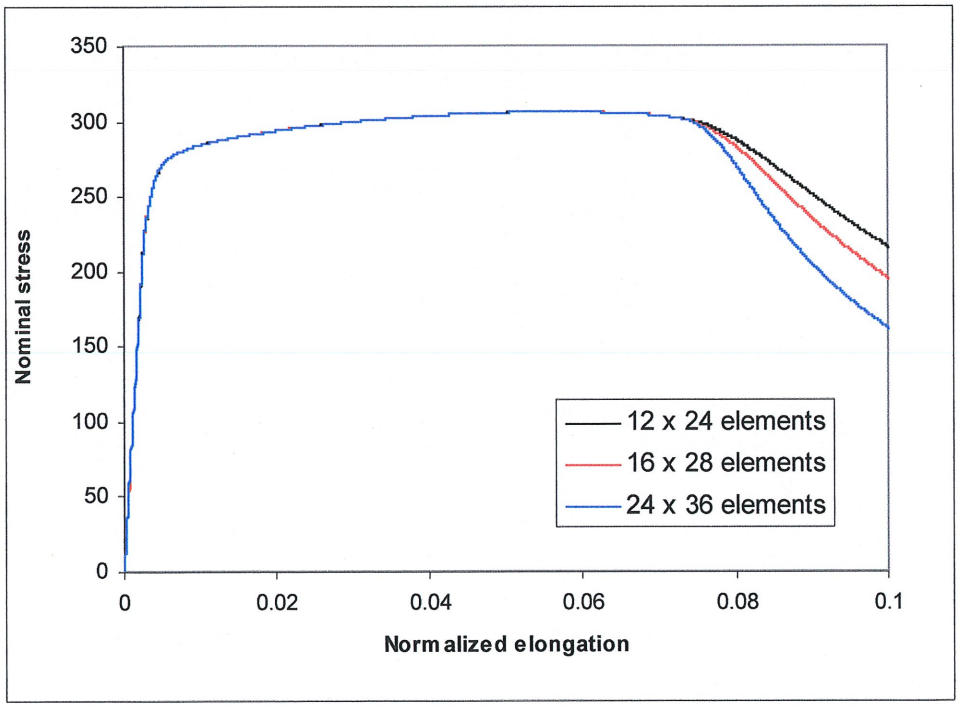

Figure 4.20 Nominal stress–normalized elongation curves for three different meshes

simulations show that the initiation and propagation of shear bands are not sensitive to the meshes considered; for all cases, localized deformation in the form of two shear bands intersecting at the centre of the specimen are formed. It is also observed that, the finer is the mesh, the narrower and stronger are the shear bands, although this does not have a significant impact on localized deformation. Based on these observations, it was decided that the relatively fine mesh (16 x 28) was sufficiently accurate. This mesh is therefore used for all simulations with

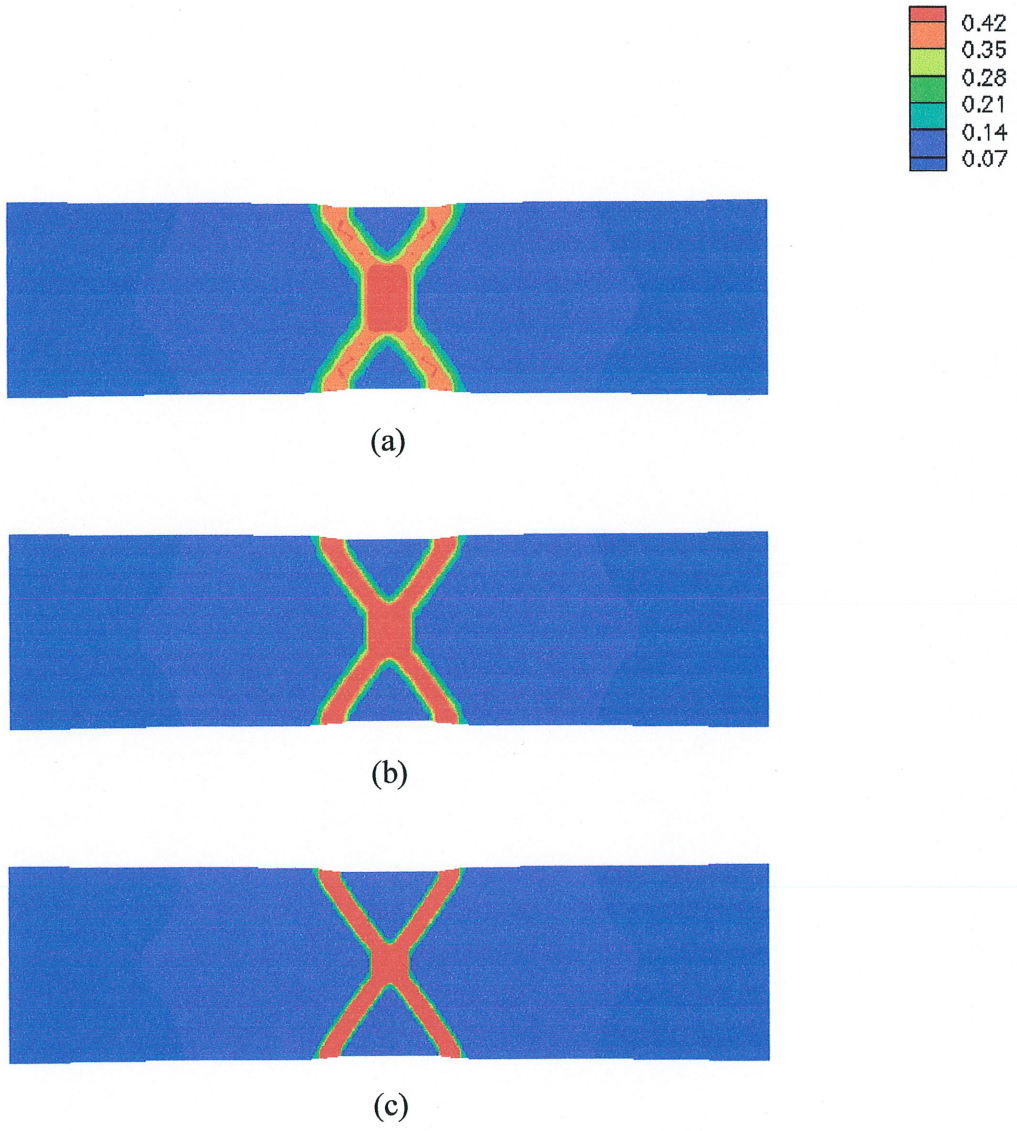

Figure 4.21 Contour plots of true strain (in loading direction) at $U/L_0 = 0.1$ for: (a) 12 x 24, (b) 16 x 28, and (c) 24 x 36 elements

one quarter of the specimen, while a mesh of 32 x 56 elements is employed for the simulations of the complete specimen.

4.3.2.3 Uniaxial tension simulations along the RD, 45^0 from the RD, and along the TD

We first present results for uniaxial tension simulations along the RD, for the 45^0 orientation from the RD, and for tension along the TD. Henceforth, simulations of uniaxial tension along the RD, 45^0 from the RD, and along the TD will be referred to as the RD, 45^0 and TD simulations, respectively. The nominal stress–strain curves for the RD, 45^0 and TD simulations are compared in Fig. 4.22. These simulations show that the nominal stress–normalized elongation curves for the RD and 45^0 simulations are quite similar, while the TD simulation results in a somewhat higher curve. The maximum nominal stresses are obtained at U/L_0=0.55, U/L_0=0.53 and U/L_0=0.52 for the RD, 45^0 and TD simulations, respectively. After saturation, softening occurs for all three orientations, with the 45^0 simulation exhibiting slightly stronger softening than the other two.

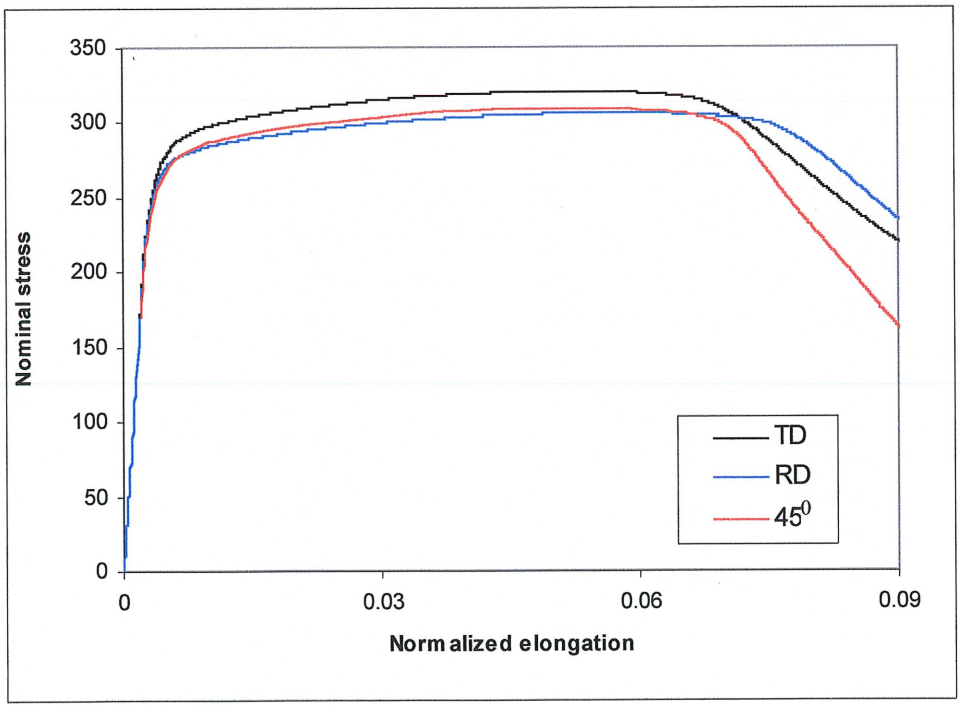

Figure 4.22 Nominal stress–strain curves for uniaxial tension along the RD, 45^0 from the RD, and along the TD

As already mentioned, the RD and TD simulations are carried on by modelling one quarter of the specimen with the assumption of orthotropic symmetry. Since that assumption is not valid for the 45^0 simulations, the full specimen is modelled for this case. In order to analyse the sensitivity of the results to the loading direction, we have compared uniaxial tension along the RD with a slightly rotated specimen, with the RD oriented at 1^0 with respect to the axis of loading. The complete specimen has been modelled for both these cases. For the RD simulations, as expected (due to orthotropic symmetry), two shear bands are predicted, similar to what was presented in Fig. 4.21b. However, when the specimen is rotated even as slightly as 1^0, only one shear band is predicted as shown in Fig. 4.23.

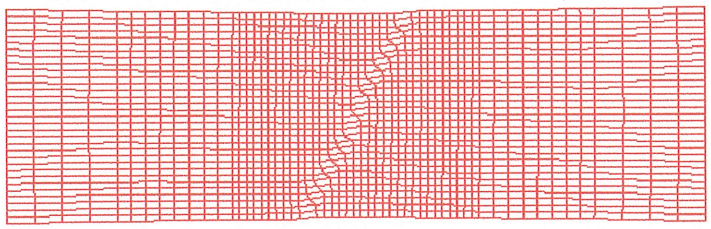

Figure 4.23 Deformed mesh for 1^0 simulation at U/L_0=0.09

Results are now presented for the deformed meshes of the RD, 45^0 and TD simulations. Figure 4.24a presents the deformed meshes at U/L_0=0.07 (after the maximum nominal stresses for all three orientations) where very slight diffused necks have formed in all three orientations. Shear bands are fully developed for all three orientations at U/L_0=0.09 (Fig. 4.24b). Here the RD and TD simulations indicate two shear bands intersecting at the centre of the specimen, while the 45^0 simulation predicts only one shear band.

A more quantitative representation of shear band development is presented in Fig. 4.25, where contours of true strain (in the loading direction) are plotted at various stages of deformation. Figure 4.25a corresponds to Fig. 4.23a, where U/L_0=0.07. The strain distribution is observed to be nonuniform for all orientations indicating localized deformation (Fig. 4.25a). For the RD simulation, the concentration of strain at the centre of the specimen indicates early stages of necking; however, there are no signs of shear banding. By contrast, for the TD and 45^0

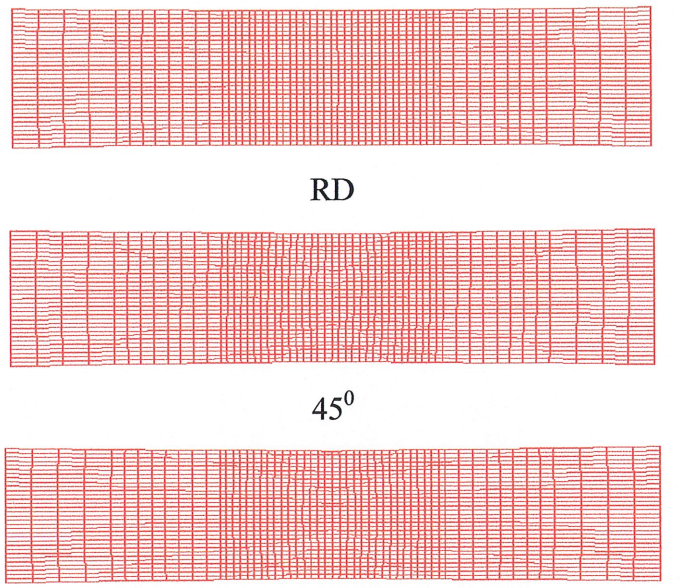

Figure 4.24 Deformed meshes for the RD, 45^0 and TD simulations at: (a) U/L_0=0.07, and (b)U/L_0=0.09

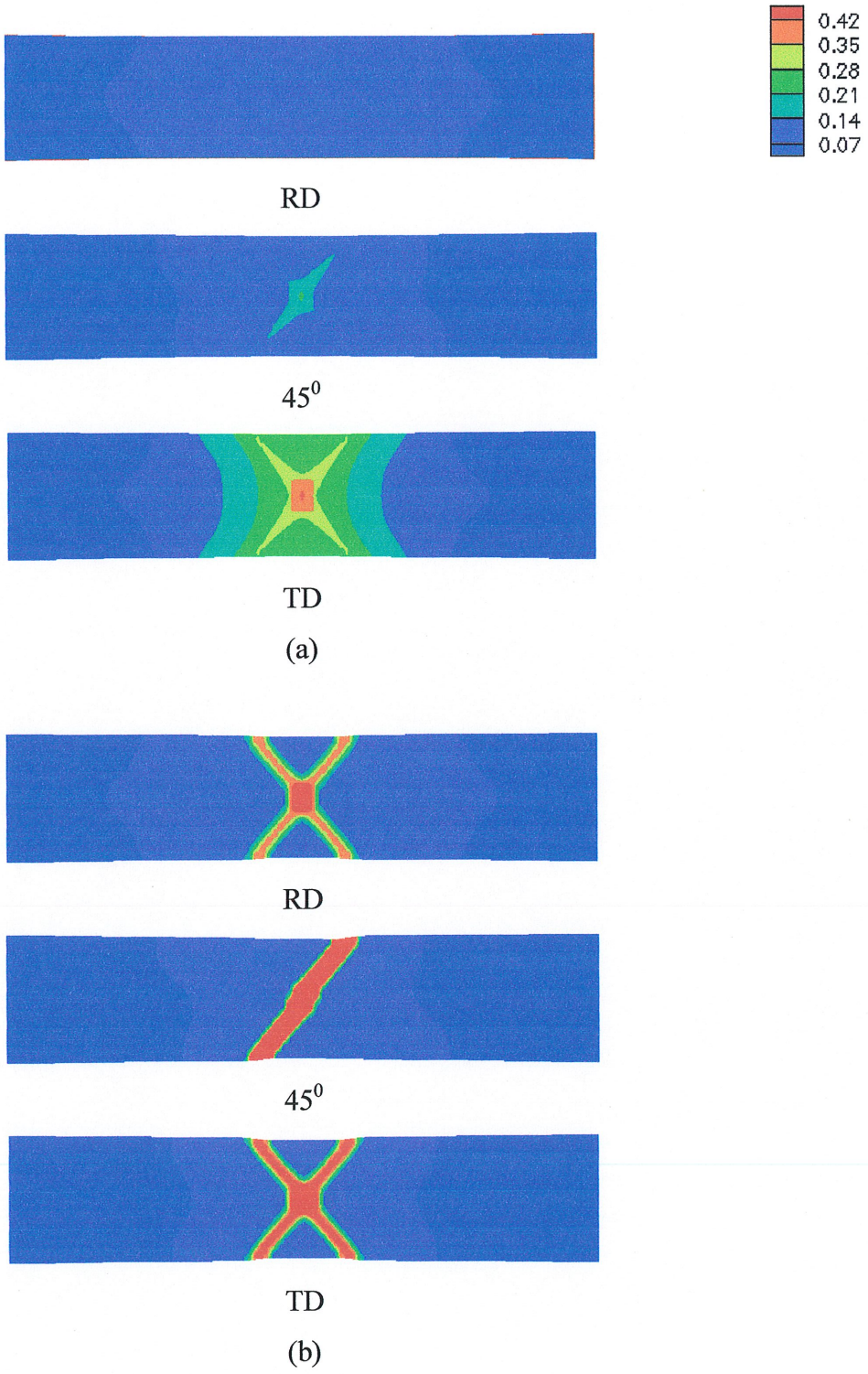

Figure 4.25 Contours of true strain (in the loading direction) for the RD, 45^0 and TD simulations at: (a) U/L_0=0.07, and (b)U/L_0=0.09

simulations, shear band patterns are evident with two bands for the TD simulation and a single band for the 45^0 simulation as indicated by the 0.21 strain contours. With further straining, it can be seen that shear bands also develop with the RD simulation. The strain in the shear bands exceed 0.35 although the overall normalized extension is U/L_0=0.09 (Fig. 4.25b). Thus, while there is very little deformation occurring outside the shear bands, a large amount of shear is accumulating within these well-defined shear bands.

4.2.3.4 Onset of localization for 45^0 simulation

As has already been discussed, numerous analytical and numerical investigations have been carried out to investigate the onset of necking and shear banding. In this section we will investigate both the onset of necking and shear banding for the 45^0 simulations.

In Fig. 4.26 the normalized stress σ/σ_{MAX} is plotted as a function of the normalized elongation. Here, σ_{MAX} refers to the maximum of the physical component of the true stress

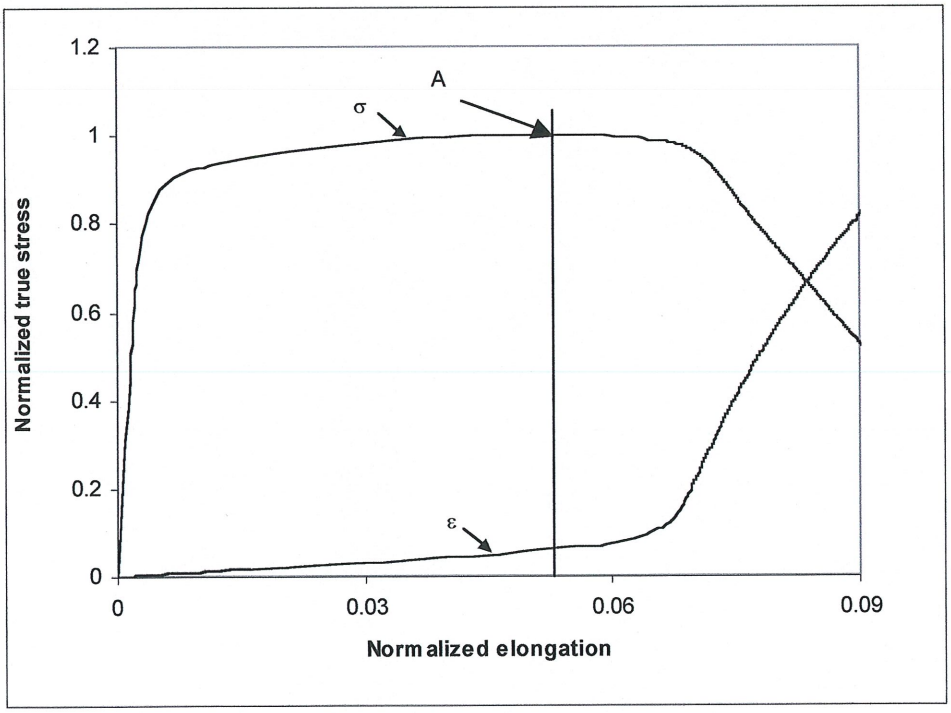

Figure 4.26 The evolution of the true strain ε (averaged at the centre of the specimen) and the true stress σ (averaged at the end of the specimen)

(in the loading direction) calculated at the end section of the specimen, $x_1 = L_0$. It can be seen that σ reaches a maximum around U/L_0=0.052 (point A), and then begins to decrease. The evolution of the true strain ε (in the loading direction) measured at the centre of the specimen is also included in Fig. 4.26. The results show that the attainment of the maximum stress at U/L_0=0.052 (point A) identifies the onset of diffuse necking, and beyond this elongation the strain ε begins to increase rapidly thus signifying localization.

It should be mentioned that the nominal stress (calculated at the end section of the specimen) for the 45^0 simulation also reaches a maximum around U/L_0=0.052. This is because of the relatively low strain rate-sensitivity (m = 0.002) used in the analysis. When the strain-rate sensitivity is increased, there is a significant difference between the elongations that the nominal and true stresses reach their maximum, as shown in Section 4.2.2.2 where m was taken as 0.02. For cases with high strain-rate sensitivity, the elongation value where the true stress σ reaches a maximum is taken as the value for the onset of diffuse necking.

The evolution of the true strains measured at the centre of the specimen are presented in Fig. 4.27. The deformations are almost uniform up to the onset of necking, which corresponds to the attainment of the maximum true stress at the end of the specimen. With continued stretching, sharp changes in the strains at the neck section occur, thus signifying localization. Note that $-\varepsilon_{22}$ reaches a maximum value at an elongation of U/L_0=0.88 and then remains nearly constant at this value during further deformation. Thus, the deformation at the centre of the specimen becomes in-plane plane strain.

Although an appropriate approximate criterion for the onset of diffuse necking has been known for some time, quantitative criteria for the initiation of localized shearing are more recent in origin. Initially, localized shearing was associated with reaching an ideally plastic state. In fact, for crystals undergoing single slip and obeying the Schmid criterion (Chapter 2) for continued yielding, it is necessary for the slip plane work hardening rate to vanish in order for localized shearing to initiate. However, in most cases shear band formation is observed in crystals undergoing multi-slip, often with a double mode of primary-conjugate slip. Employing a planar idealization of this primary-conjugate slip mode, Asaro (1979) found that, for single crystals,

shear band initiation is associated with the attainment of a critically small positive value of the ratio of slip plane hardening rate to the current stress level.

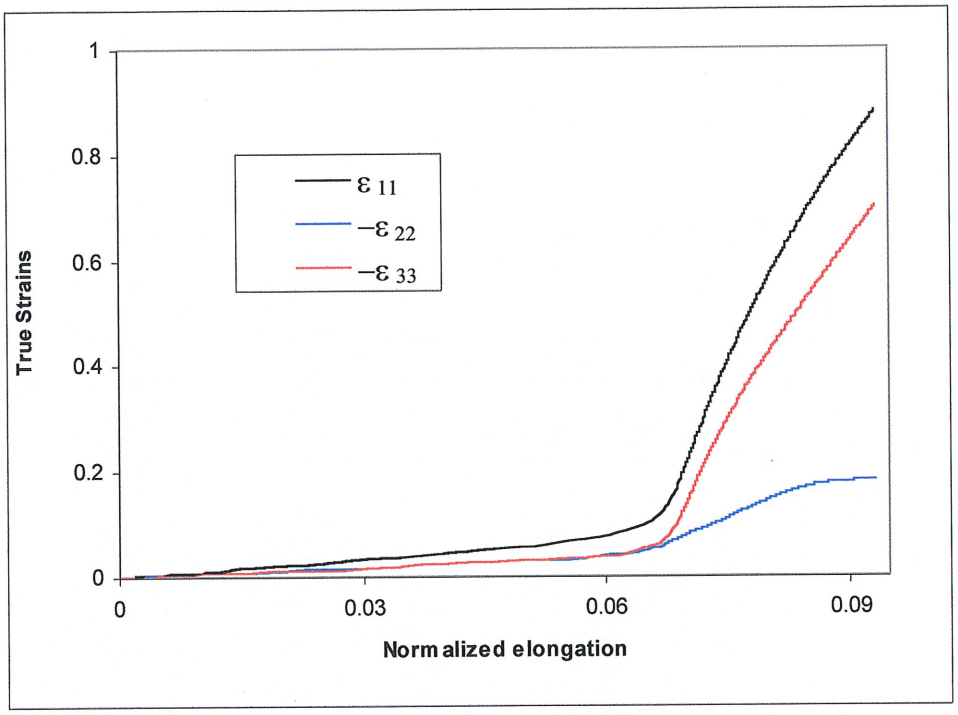

Figure 4.27 The evolution of the true strains ε_{ii} at the centre of the specimen

In this study, a macroscopic parameter is introduced to define a criterion for the onset of shear banding. The onset of diffuse necking (Fig. 4.26) has already been defined as the attainment of maximum true stress (at the end of the specimen). To determine the onset of shear banding, the true stress–strain curve obtained at the centre of the specimen, averaged along line B-B' as shown in Fig. 4.28, is examined. The average true stress calculated along line B-B' reaches a maximum around U/L_0=0.068 as shown by point B in Fig. 4.29. In order to investigate the localization mode, contour plots of true strain in loading direction at points A (defined in Fig. 4.26) and B (defined in Fig. 4.29) are presented in Fig. 4.30. Figure 4.30a corresponds to point A where U/L_0=0.052. It can be seen that the strain is concentrating towards the centre of the specimen, thus, indicating the initial phases of necking. When Fig. 4.30b (which corresponds to

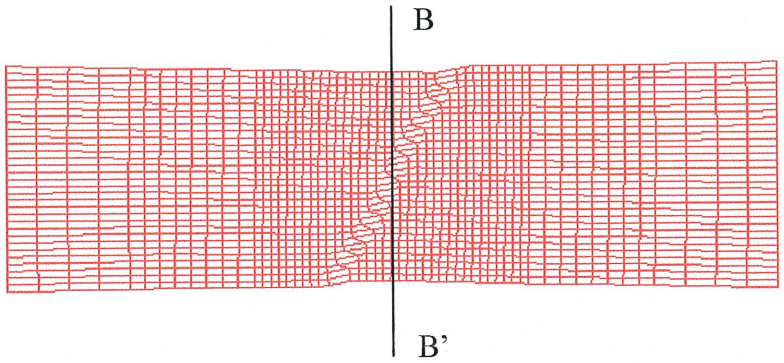

Figure 4.28 Deformed mesh for 45^0 simulation

point B where U/L_0=0.068) is examined, it can be seen that the strain has begun to localize in the form of a band (represented by the 0.12 strain contour), thus indicating the initiation of shear banding. Note that if the localization mode is only necking, the stress–strain curve obtained along line B-B' will always exhibit strain hardening. Thus the attainment of maximum true stress calculated along line B-B' can be taken as an approximate criterion for the onset of shear banding.

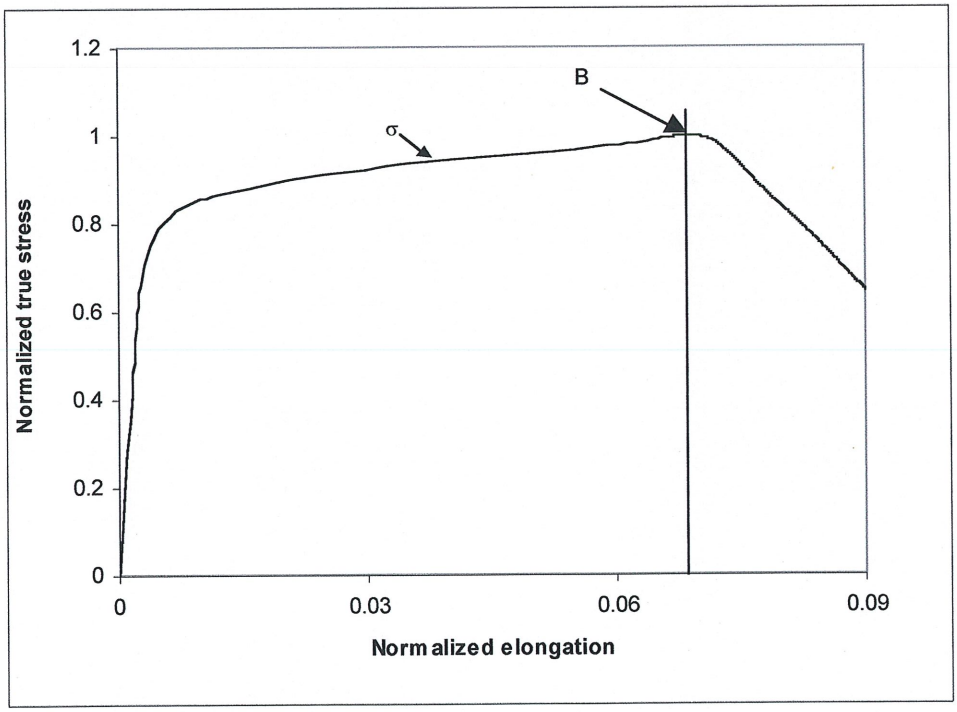

Figure 4.29 The evolution of the true stress σ (averaged along line B-B')

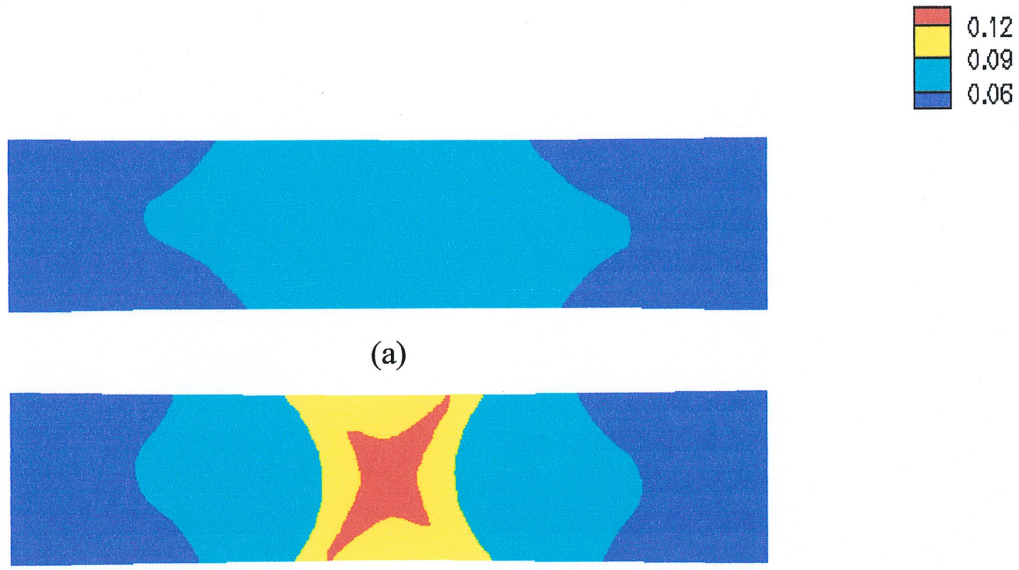

(a)

(b)

Figure 4.30 Contours of true strain (in loading direction) for 45^0 simulation at: (a) U/L_0=0.052, and (b)U/L_0=0.068

However, the application of this onsetting criterion during laboratory experiments would undoubtedly be very difficult since after the maximum is attained the load drops very abruptly. By the time the drop is noticed, failure might already have already occurred.

4.5 Conclusion

In this chapter we have analyzed localized deformation modes in FCC polycrystals using our crystal plasticity based finite element model. The behaviour of the aluminum sheet alloy AA3004-H19 was investigated under both plane strain tension and plane stress tension.

Our simulations have shown that localization occurs in two modes. For the first mode, a neck initiates and deformation continues as the strain localizes progressively in this neck. For the rate dependent analysis considered, the onset of necking is defined as the attainment of the maximum stress at the end section of the specimen, away from the neck. For the limiting case of a rate-independent material, this criterion reduces to the attainment of a maximum strain (which is the onset of the elastic unloading) since for the rate-independent analysis the attainment of

maximum strain will also correspond to the attainment of the maximum stress. For the second localization mode, necking triggers the formation of shear bands. There are several factors that contribute to the formation and prediction of shear bands such as texture evolution, strain rate sensitivity, and strain hardening.

Our calculations have shown that it is possible to define an appropriate approximate criterion for the onset of shear banding. The attainment of the maximum stress at the centre of the specimen (calculated as an average over line B-B' as shown in Fig. 4.29) corresponded to the onset of shear banding for all three orientations considered in this study. It is obvious that, when the localization mode is simply necking without shear banding, the stress calculated at the centre of the specimen does not pass through a maximum since there will always be strain hardening at the centre of the specimen.

A significant mesh sensitivity was not observed for the overall stress response, nor for the initiation and propagation of the localized deformation. Our calculations showed that the finer is the mesh, the narrower and sharper become the shear bands. It is important to mention that the mesh sensitivity analysis carried out in this chapter was carried out by refining the mesh without changing the initial element aspect ratio.

One of the factors affecting localized deformation is the loading direction, since the overall stress response and deformation pattern is sensitive to this. Even the slightest rotation of the loading direction was seen to have a significant effect on the deformation pattern; two shear bands were predicted for uniaxial tension along the RD, while only one single shear band was predicted for uniaxial tension along 1^0 from the RD.

Texture evolution was shown to play a very important role in the prediction of shear bands. If texture evolution is not included to the model, the "geometric softening" effect that leads to localized shearing does not occur. As a result, shear band formation is precluded from the localization mode. The simulations have shown that shear bands were formed for engineering strain of about 10%. Although strong textures are not expected to occur at strains of this value, the evolution of texture at this strain level is still critical to the proper prediction of shear bands.

This effect of texture evolution also explains the inability of phenomenological plasticity models with a smooth yield surface to predict shear bands at realistic strain levels (e.g., Tvergaard et al., 1981).

It is well known that increasing the material rate sensitivity increases ductility as it will delay the formation of nonuniform localization modes such as shear bands or necking. In this regard, our simulations have shown that, when the rate sensitivity was increased to certain values (corresponding to a decrease in the rate of texture evolution), shear band formation was not only delayed, but was completely precluded from the localization mode since the resulting "geometric softening" was not strong enough to form shear bands.

Strain hardening is another important factor in the formation of shear bands. Our results have shown that strain softening behaviour is not necessarily required to predict shear bands or other localized modes of deformation. However, the rate of strain hardening plays a key role in the determination of the localization mode. When a relatively high rate of strain hardening was considered, shear band formation was completely precluded from the localization mode.

CHAPTER 5

LARGE STRAIN BEHAVIOUR OF THIN ALUMINUM SHEETS UNDER PLANAR SIMPLE SHEAR

5.1 Introduction

The formability of aluminum alloys used in sheet-metal forming operations encountered in packaging and can-making is often limited by plastic strain localization such as necking or shear banding (as discussed in Chapter 4), which may lead to early failure. Thus, understanding and characterizing the large strain behaviour of thin rolled aluminum sheets are crucial for controlling product quality and for progressively down-gauging in the canning industry.

The experimental investigation of the large strain behaviour of thin sheets used in the canning industry is not easy due to their strong rolling texture, high strength, and low hardening rate. For example, the most commonly used uniaxial tension test can reach only 8% strain before fracture following localized necking. However, shear deformations are able to achieve large strains because of the inherent geometric stability of this mode of deformation.

The torsion test is more and more frequently used to assess large strain behaviour for many different engineering materials. For the circular cross sections widely used in the torsion testing of ductile metals at finite strain, torsion gives rise to inhomogeneous simple shearing, possibly combined with uniaxial or biaxial stretching. For a thin-walled circular section the deformations are nearly homogeneous and correspond to combined simple shear and plane strain extension, provided that the thickness of the tube remains constant. The kinematics of the torsion test and its relation to simple shear have been discussed by Shrivastava et al. (1982) for solid circular bars, and by McMeeking (1982) for thin-walled tubes.

Although the torsion test is a very valuable tool for achieving large strains, its application to can-body (e.g., AA3004-H19) and can-end (e.g., AA5182-H28) aluminum alloy sheets is not practical because of the inevitable buckling due to the very thin gauge. Recent researches have indicated that the planar simple shear test can be used to characterize the plastic behaviour of very thin sheet metals at large to very large strains (Gasperini et al., 1996; Duval et al., 1996; Legresy et al., 1997). However, very few laboratory shear testing setups are available. These tests are conducted on flat parallelepiped samples cut from the sheet specimens.

Some authors (Rauch et al., 1989; Gaspérini et al., 1996) have reported that localization by shear banding may occur during the shear tests, due to sample end effects and material behaviour. For heavily cold-rolled aluminum alloys, Gaspérini et al. (1996) showed that the initial dislocation microstructure and the crystallographic texture influenced the localization and the post-localization behaviour during shear tests. Their tests were performed using a shear device mounted on a conventional tensile machine. Their results also showed that there was no localization during the shear tests of recovered material. They linked this observation to the relative homogeneity of the substructure and the absence of strong barriers to dislocation glide for the second path.

For aluminum can-end sheet AA5182-H28 of gauge 0.27 mm, Legresy et al. (1997) found that the deformation in the gauge section remained essentially homogeneous, and no macroscopic localized shear band was detected if the specimen was sheared along the rolling direction (RD). When the shear deformation was applied at 45° from the RD, very few shear bands appeared, and a ductile crack initiated in one of the shear bands. Many shear bands were observed on the sample surface in the case of shearing along the transverse direction (TD).

Recently, Wu et al. (2001) employed a 2-D finite element analysis to simulate the large strain planar simple shear of a can body stock (CBS) AA51820-H48 aluminum alloy based on crystal plasticity theory. They presented results from two models: a model based on a Taylor-type polycrystal plasticity theory, and a model where a material point or a polycrystal is represented by an "unit-cell" in which an element of the finite element mesh represents a single crystal. Based on these two models, they investigated the initiation and evolution of shear bands at different length scales.

In this chapter we analyze numerically the large strain behaviour of the aluminum can-body sheet AA3004-H19 under planar simple shear using our polycrystal model-based finite element code (Inal et al., 2001c). Both plane stress and plane strain analyses are performed to investigate the validity of either assumption in the modelling of the planar simple shear problem. Simulations are performed with specimens rotated such that the rolling direction is at 0^0, 45^0 and 90^0 to the shearing axis. The initiation and propagation of shear bands are investigated. These

simulations are compared with homogeneous simple shear deformations and experimental data published in the literature.

5.2 Problem formulation

The planar simple shear deformation of a parallelepiped solid of initial length L and height W, as illustrated in Fig. 5.1, is considered. The shear deformation is expressed by the ratio $\gamma = U / W$, where U is the relative displacement of the opposite faces of the parallelepiped. The conventional nominal shear stress and normal stress are defined by F_s / L and F_n / L, where F_s and F_n are the applied shearing and normal forces per unit thickness, respectively. The dimensions L and W are assumed to remain constant during the deformation. The vertical sides AD and BC are assumed to be stress free (Fig. 5.1) as in the real planar simple shear test (Gaspérini et al., 1996; Legresy et al., 1997), and the sides AB and CD are assumed to remain straight. Thus, the boundary conditions are:

$$\begin{aligned} u_2 &= 0 \text{ along } x_2 = 0 \text{ and along } x_2 = W \\ u_1 &= 0 \text{ along } x_2 = 0 \\ \dot{u}_1 &= \text{V (applied velocity) along } x_2 = W \end{aligned} \tag{5.1}$$

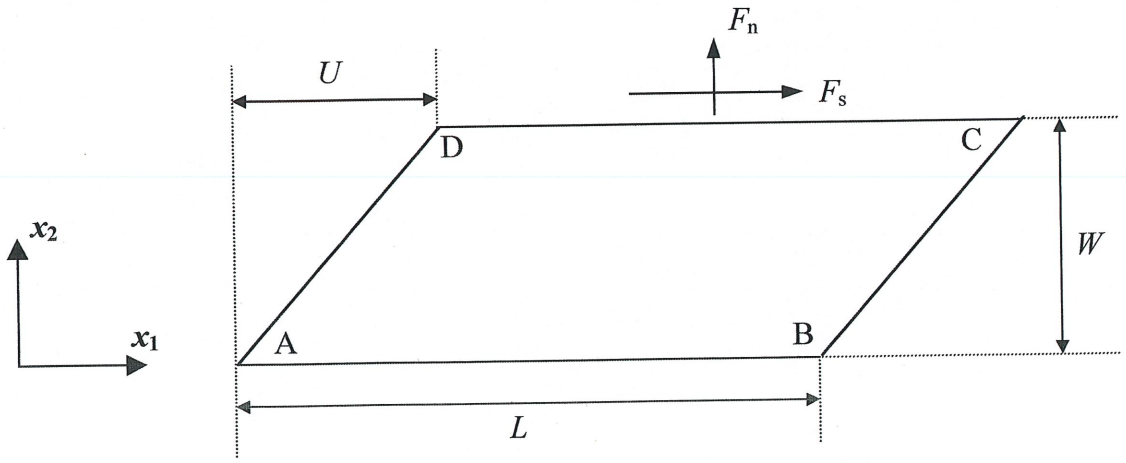

Figure 5.1 Schematic definition of the specimen under planar simple shear

The FE mesh used in the simulations consists of four-node quadrilateral elements, constructed from four 'crossed' constant strain triangular sub-elements as described in Chapter 4.

5.3 Results and discussion

The initial texture (represented by 380 crystals) of the aluminum can-body sheet AA3004-H19 is presented in Fig. 5.2 in terms of a {111} stereographic pole figure. Here X_1 and X_2 refer to the rolling and transverse directions of the sheet, respectively.

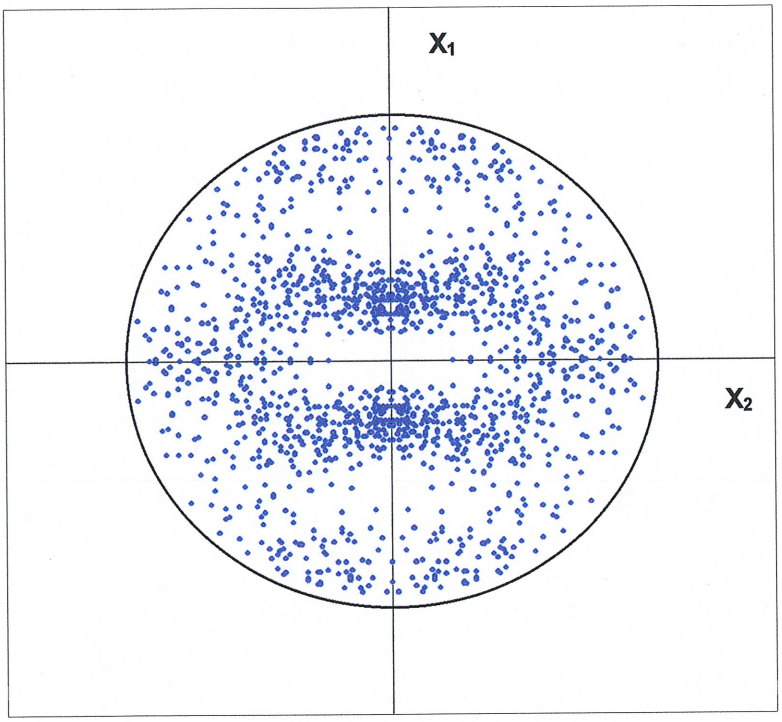

Figure 5.2 Initial texture of AA30004-H19 represented by a {111} stereographic pole figure

The single slip hardening law used for the simulations in Chapter 4 is employed for the simple shear analysis. Accordingly, the material properties are,

$$\tau_0 = 95 \text{ MPa},\ h_0/\tau_0 = 1.2,\ \tau_s/\tau_0 = 1.16,\ h_s/\tau_0 = 0,\ q = 1.0 \qquad (5.2)$$

The slip system reference plastic shearing rate $\dot{\gamma}_0$ and the slip rate sensitivity parameter m are taken as $\dot{\gamma}_0 = 0.001 s^{-1}$ and $m = 0.002$, respectively, with the crystal elastic constants taken as C_{11} = 206 GPa, C_{12} = 118 GPa and C_{44} = 54 GPa.

5.3.1 Plane strain simulations

In this section, our plane strain finite element model is employed to simulate planar simple shear for specimens rotated such that the rolling direction is at 0^0, 45^0 and 90^0 to the shearing axis. The geometry of the specimen is described by L / W =15 and this value is used for all simulations presented in this section.

5.3.1.1 Mesh sensitivity

The importance of mesh sensitivity on localized deformation was discussed in Chapter 4. Thus, a mesh sensitivity study for the specimen oriented at 45^0 with respect to the shearing axis has been performed. Figures 5.3 a-c illustrate the finite element meshes with 10 x 50, 12 x 60 and 20 x 100 elements, respectively.

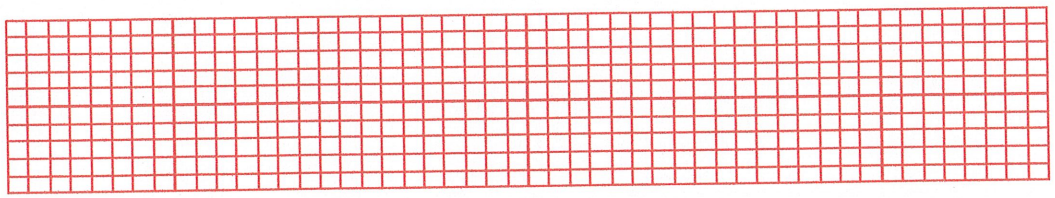

(a)

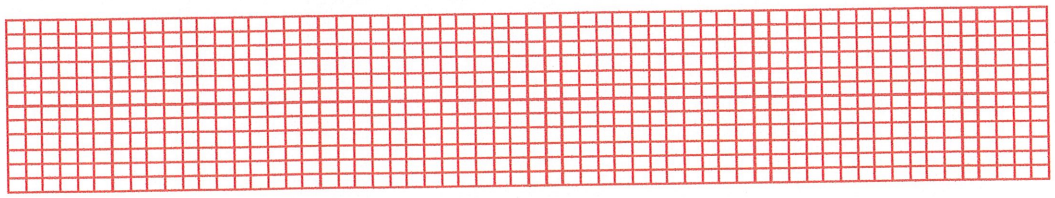

(b)

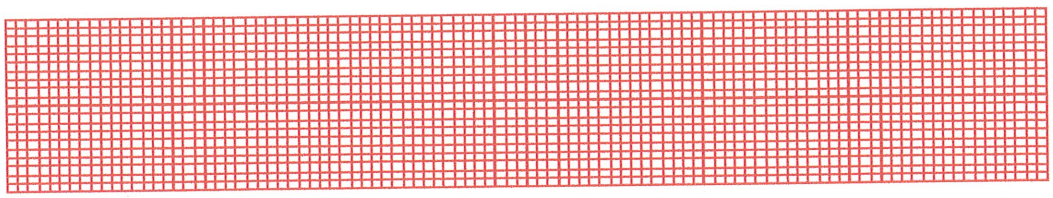

(c)

Figure 5.3 Initial meshes for: (a) 10 x 50, (b) 12 x 60, and (c) 20 x 100 elements

The shear stress–shear deformation curves up to a shear deformation of 0.4 are presented in Fig. 5.4. The results are similar to those obtained in Chapter 4; the curves are nearly identical during the strain hardening and saturation stages. Once there is softening, the finer meshes predict stronger softening effects.

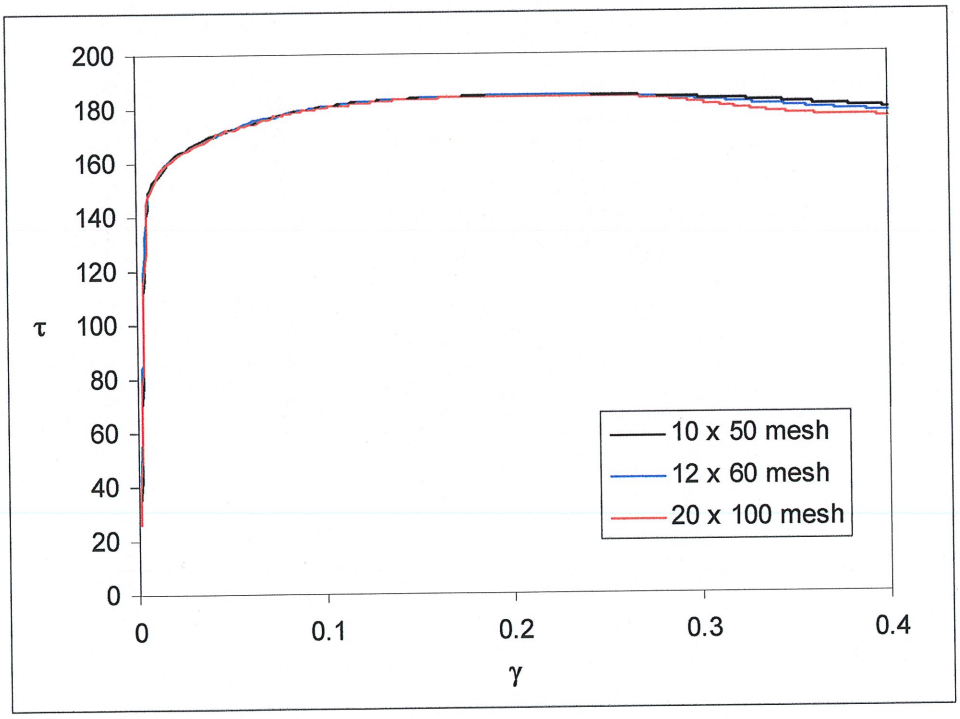

Figure 5.4 Shear stress responses under simple shear predicted with different finite element meshes

Figures 5.5 a-b show contours of a measure of an "equivalent plastic shear strain", γ^p (normalized by the applied shear deformation γ) as defined by (Anand et al., 1994)

$$\dot{\bar{\gamma}}^p = \frac{\sum \tau^{(\alpha)} \dot{\gamma}^{(\alpha)}}{\bar{\tau}}, \quad \gamma^p = \int \dot{\gamma}^p \, dt \tag{5.3}$$

where

$$\bar{\tau} = \sqrt{\frac{1}{2} S_{ij} S^{ij}} \tag{5.4}$$

is the effective shear stress and S_{ij} and S^{ij} are the covariant and contravariant components of the deviatoric stress tensor respectively. Regions of enhanced shear appear at the corners of the specimen in simulations with all three finite element meshes (Fig. 5.5 a). These regions gradually grow into two nearly parallel shear bands (Fig. 5.5b).

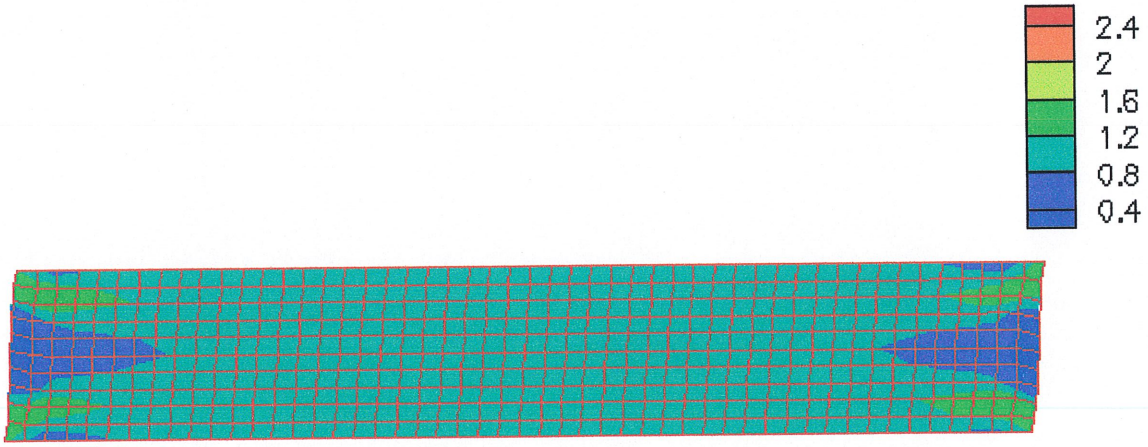

10 x 50 elements

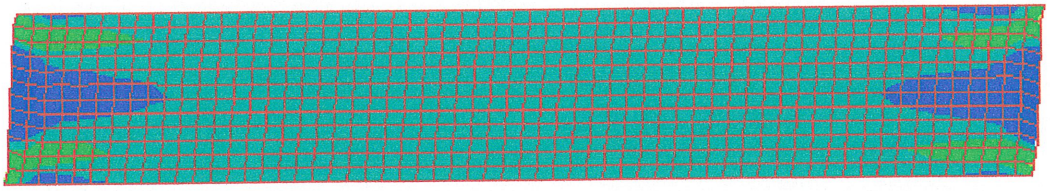

12 x 60 elements

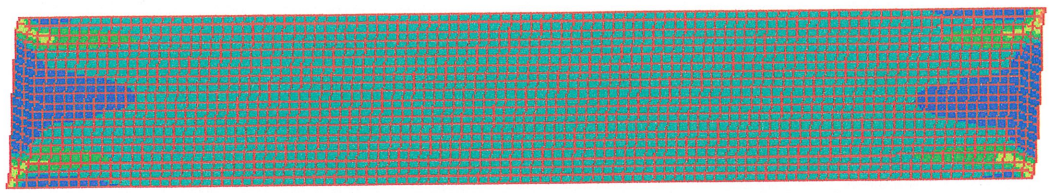

20 x 100 elements

(a)

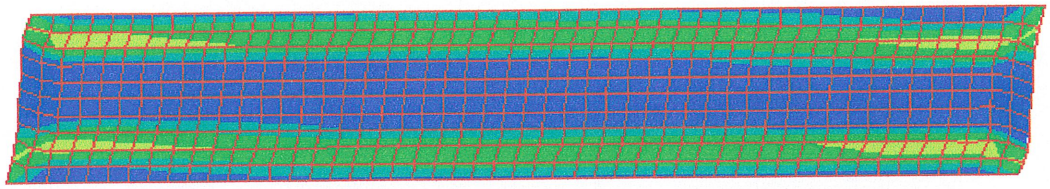

10 x 50 elements

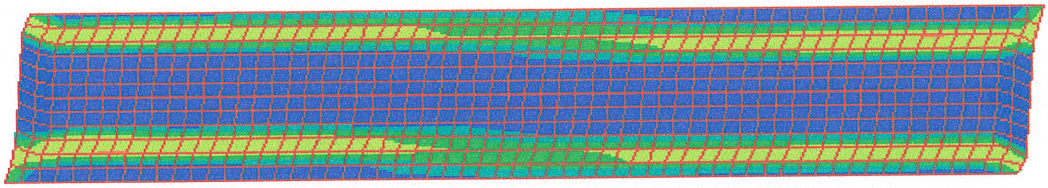

12 x 60 elements

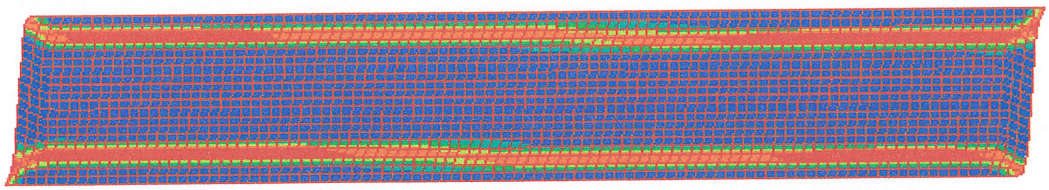

20 x 100 elements

(b)

Figure 5.5 Contours of normalized equivalent plastic shear deformation for different finite element meshes at: (a) $\gamma = 0.2$, and (b) $\gamma = 0.4$

Considering the three different meshes used in the analysis, it can be seen that the finer is the mesh, the narrower and stronger are the shear bands. However, mesh sensitivity (for the meshes considered) does not have a significant effect on the characteristics of localization. Thus, the relatively fine mesh (12 x 60) will be used for the rest of the simulations.

5.3.1.2 Simulations of simple shear with specimens rotated at 0^0, 45^0 and 90^0 to the shearing axis

Results of planar simple shear simulations with the plane strain FE code will first be presented. From now on, simulations of planar simple shear with specimens rotated such that the rolling direction is at 0^0, 45^0 and 90^0 to the shearing axis will be referred to as the RD, 45^0 and TD simulations, respectively. For comparison, results obtained with the assumption of homogeneous simple shear are also included.

Figure 5.6 shows the overall shear stress responses for the RD simulations as predicted by the FE code analysis and from an analysis assuming homogeneous deformation. These curves are seen to be very close. For both calculations, the overall shear stresses reach a saturation value at a shear deformation of about 0.3, and neither the homogeneous deformation analysis nor the FE prediction show any significant softening effects.

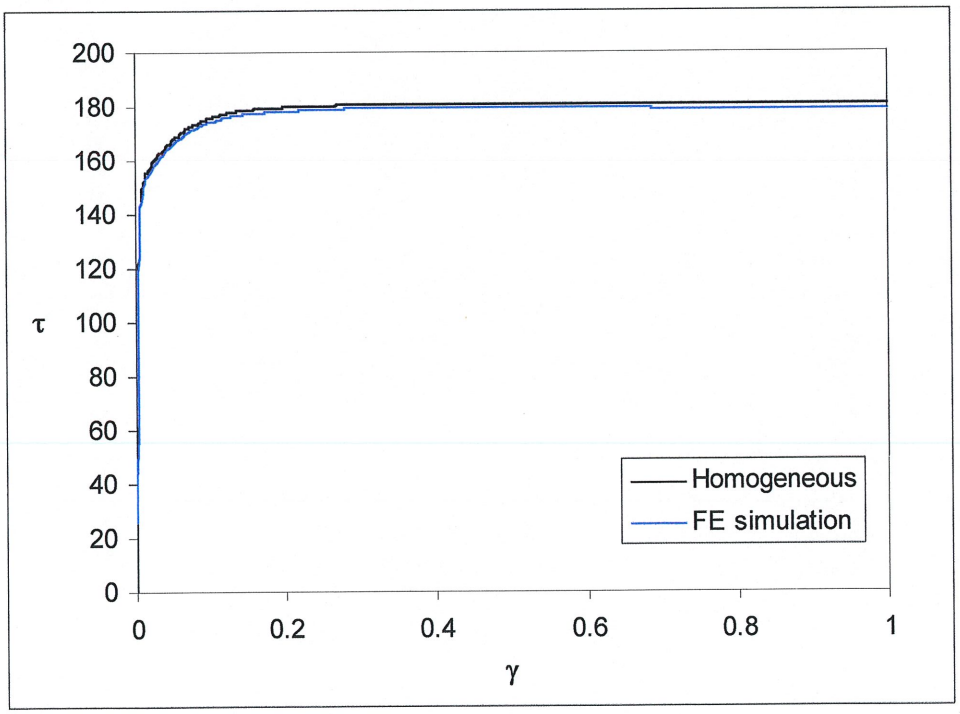

Figure 5.6 Predicted overall shear stress responses for the RD simulations

The 45° simulations (Fig. 5.7) show that the results from our FE code and the homogeneous deformation analysis are very close up to a shear deformation of about 0.25, where the overall shear stresses reach a maximum. With further shearing, softening is found in both the homogeneous deformation and FE analyses. Between shear deformations of about 0.25 and 0.45, the FE analysis shows more significant softening than the homogeneous deformation. After 0.45 shear deformation, both simulations exhibit more or less the same softening effect.

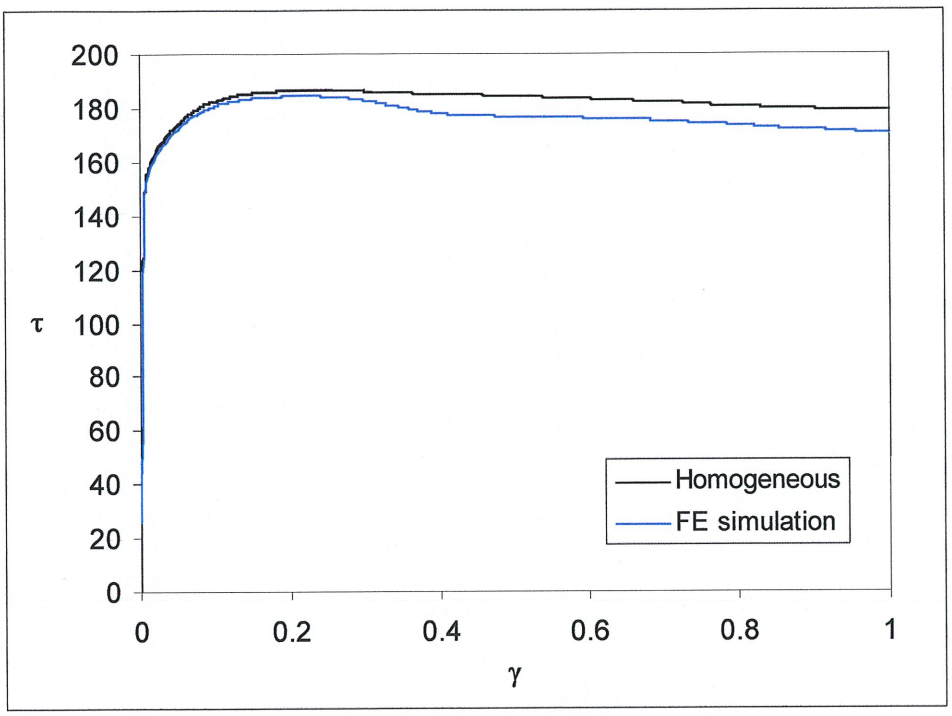

Figure 5.7 Predicted overall shear stress response for the 45° simulations

When the TD simulations are considered (Fig. 5.8), the results from the homogeneous deformation analysis and our FE code are very close again up to a shear deformation of 0.3, where they both reach a maximum. After about 0.4 shear deformation, softening occurs in both simulations. Although the homogeneous deformation continues with slight softening, the deformation pattern for the FE analysis is different; a strong softening effect up to 0.55 shear deformation is followed by a hardening up to a shear deformation of 0.8.

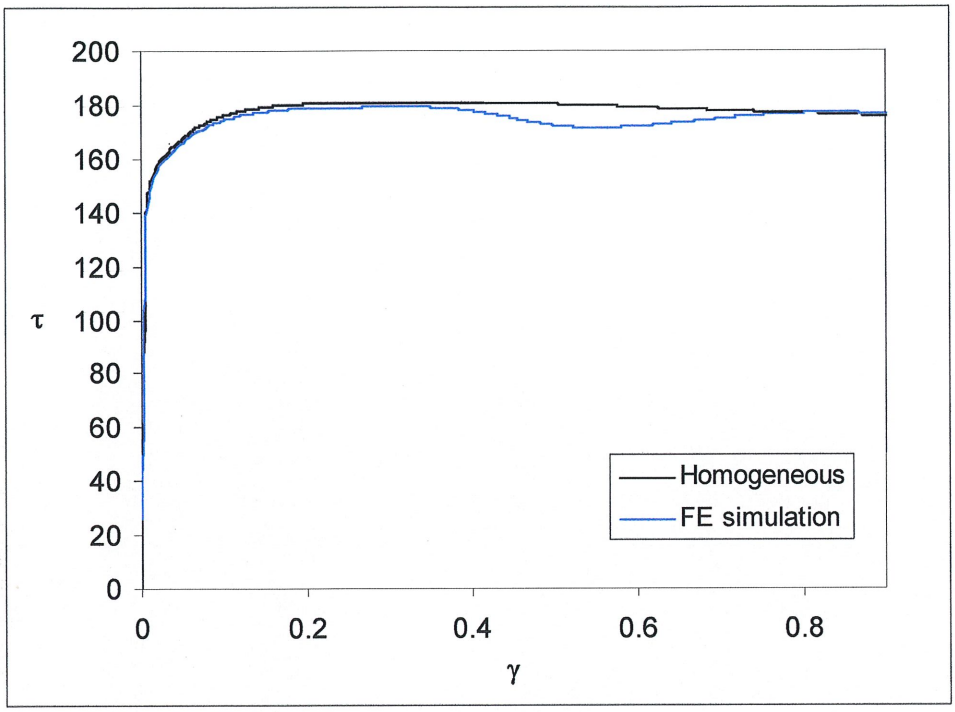

Figure 5.8 Predicted overall shear stress response for the TD simulations

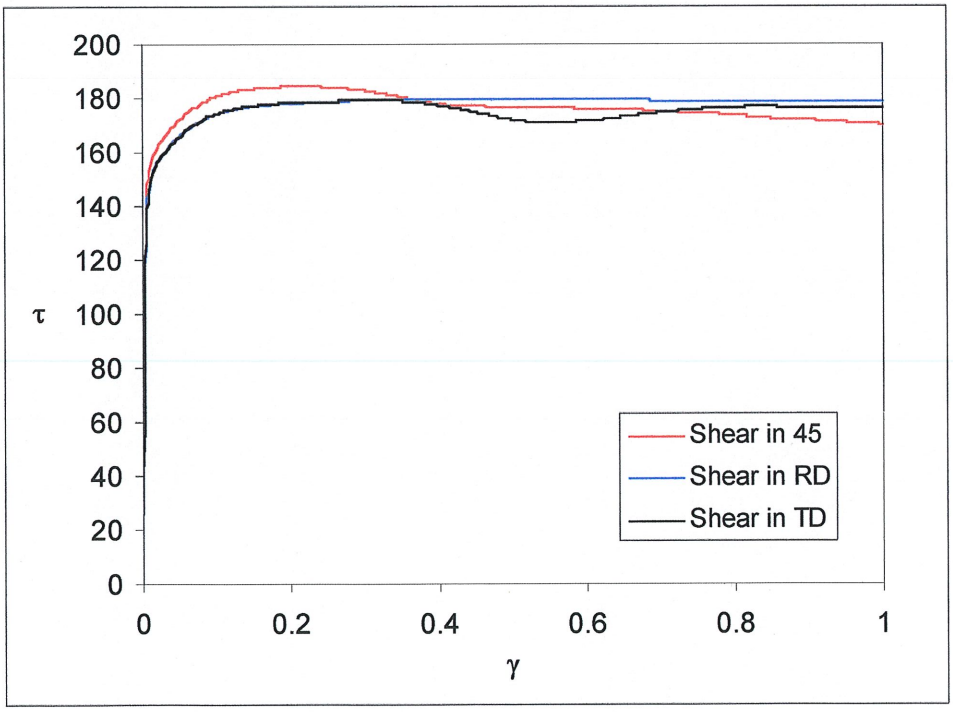

Figure 5.9 Predicted overall shear stress responses for the RD, 45° and TD simulations

To compare results from the RD, 45° and TD simulations, the overall shear stress responses obtained from the FE analyses are shown together in Fig. 5.9. The simulations show that all curves exhibit a rapid hardening followed by a decreasing hardening rate leading to a saturation of the flow stress. The maximum shear stress τ_{max} is higher for the 45° simulation (τ_{max}=184 MPa) than the RD (τ_{max}= 179 MPa) and TD (τ_{max}= 179 MPa) simulations. Although there is no softening effect in the RD simulation, significant softening effects are found both in the 45° and TD simulations.

In order to investigate the initiation and propagation of shear bands, we present in Figs. 5.10 – 5.13 contour plots of normalized equivalent plastic shear strain γ^p at different stages of

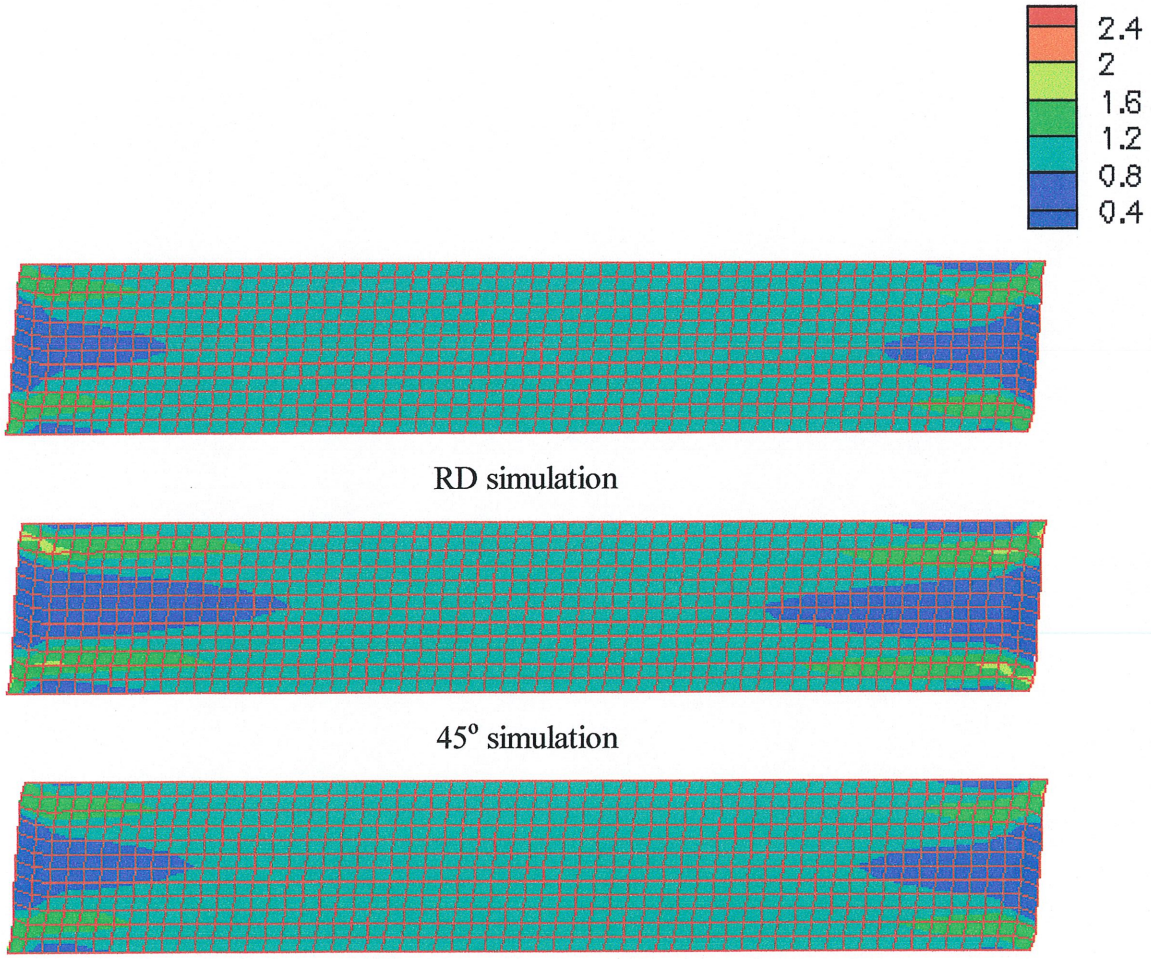

Figure 5.10 Contours of normalized equivalent plastic shear strain γ^p at $\gamma = 0.25$

the deformation. At a shear deformation of 0.25, four regions of enhanced shear appear at the corners of the specimen (Fig. 5.10). With further shearing, these regions gradually grow into two nearly parallel shear bands for the 45° and TD simulations at a shear deformation of 0.5.

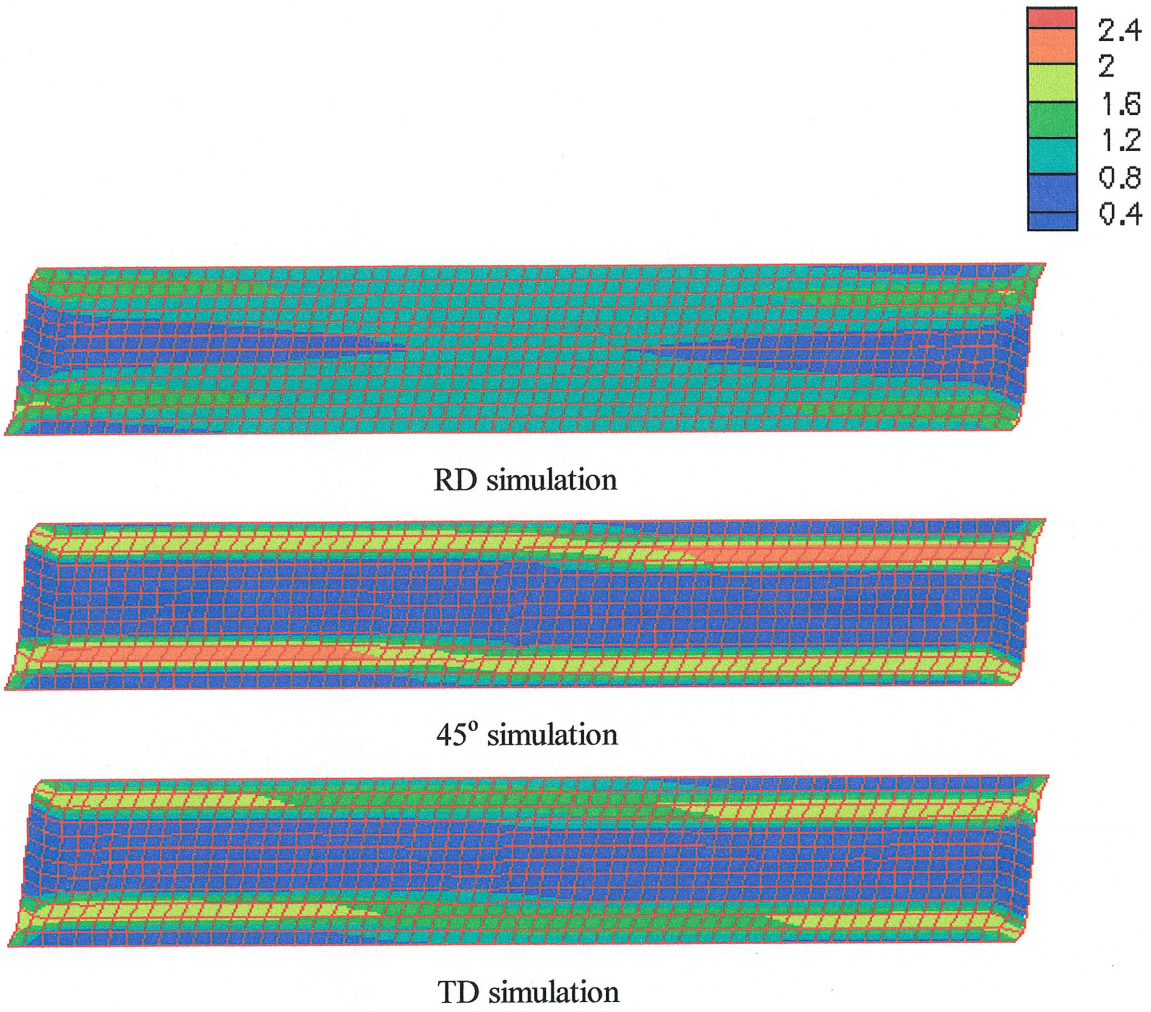

Figure 5.11 Contours of normalized equivalent plastic shear strain γ^p at $\gamma = 0.5$

However, for the RD simulation, there remain four shear bands, not linked to each other (Fig. 5.11). Once the shear bands are fully formed from end to end, the applied shear strain is mainly concentrated in these two shear bands which can be observed in Figs. 5.11 – 5.13. These simulations indicate that the locations of the shear bands are identical for all the shearing directions considered, with the strongest shear bands occurring in the 45° simulation and the weakest bands in the RD simulation.

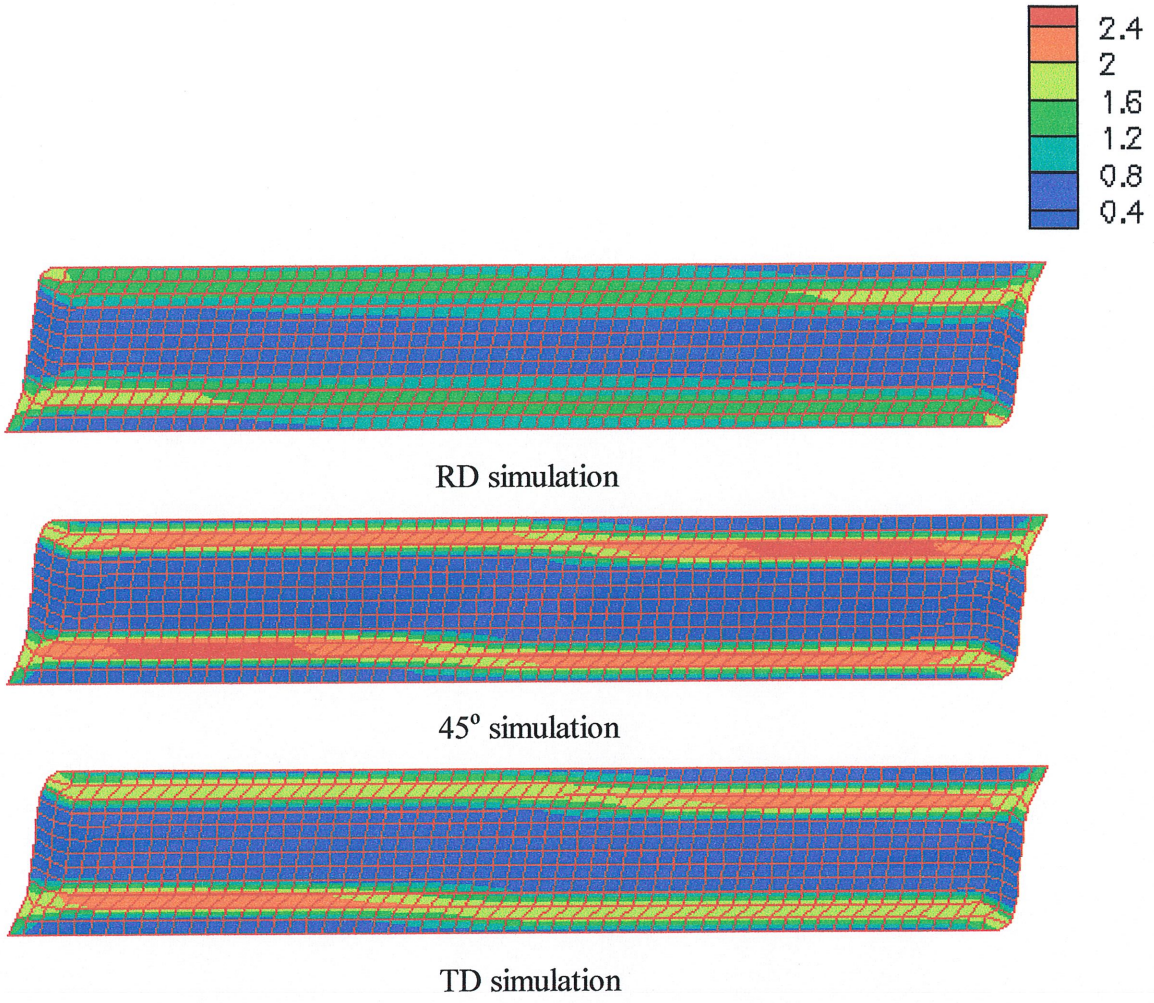

Figure 5.12 Contours of normalized equivalent plastic shear strain γ^p at $\gamma = 0.75$

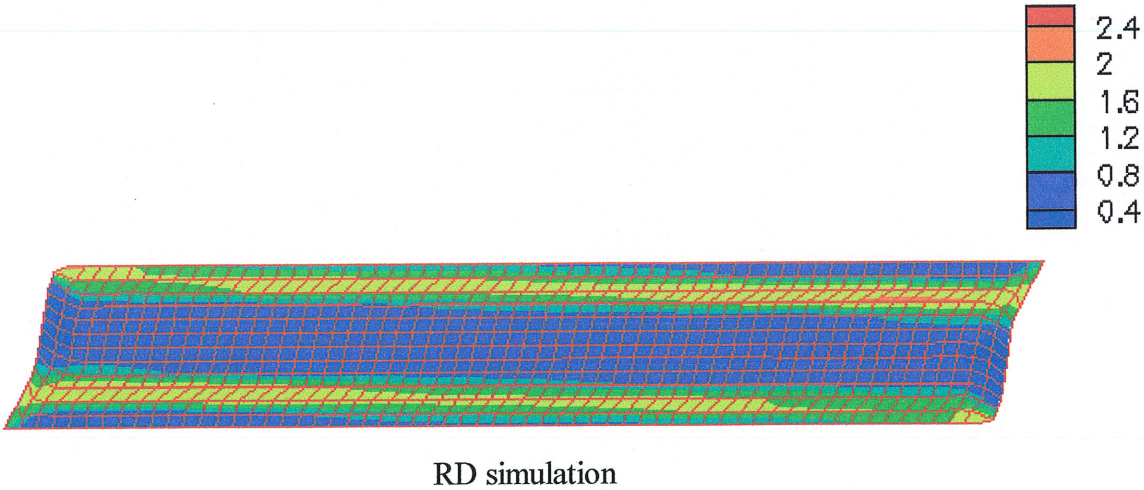

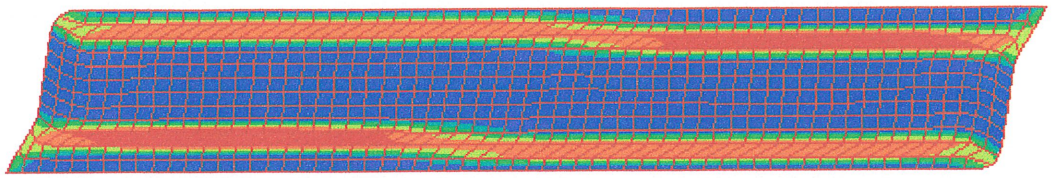

45° simulation

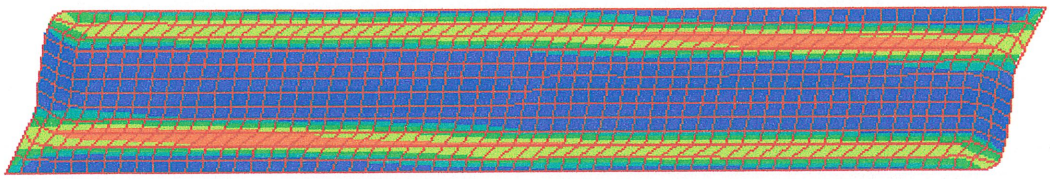

TD simulation

Figure 5.13 Contours of normalized equivalent plastic shear strain γ^p at $\gamma = 1.0$

There are some interesting observations that should be mentioned for the RD and TD simulations. There is no indication of localized deformation in the shear stress–shear deformation curve (Fig. 5.9) for the RD simulation. However the contour plots of normalized equivalent plastic shear strain γ^p (Figs. 5.10–5.13) show that shear bands occur during the RD simulations. This observation is in good agreement with the experimental results reported by Gaspérini et al. (1996).

The shear stress–shear deformation curve (Fig. 5.9) for the TD simulation indicates that the softening which occurs after 0.35 shear deformation is followed by a certain degree of hardening. However, when the contour plots of normalized equivalent plastic shear strain γ^p (Fig. 5.10) are investigated, there are no signs of this late stage hardening. The softening corresponds to the formation of the shear bands and once these shear bands are fully formed, very little deformation occurs outside these bands. Thus this late stage hardening observed in the TD simulation is not due to a change in the localized deformation mode. Instead, it might be explained as an effect of the finite element mesh used in the simulation.

Gaspérini et al. (1996) have provided detailed experimental data on the characteristics of localization for the aluminum can-body sheet AA3004 subjected to shearing. Their results

showed that, for the RD, 45° and TD simulations considered in this thesis, two narrow bands appear at the corners D and B (Fig. 5.1). These bands then rapidly progressed along the whole length of the specimen, and eventually coalesced. For the RD simulation, after a shear deformation of 0.2, new shear bands were formed parallel to the first so that the whole specimen was eventually filled with bands. For the 45° and TD simulation, the previously formed bands widened slightly, but the bands did not invade the specimen. In our simulations (for all three orientations of shearing) shear bands start from the four corners of the specimen, and they gradually grow into two nearly parallel shear bands. This disagreement between our simulations and the experimental observations is perhaps partly due to: the coarse mesh that we have used, the assumption of plane strain, and the basics underlying the Taylor-type polycrystalline model.

5.3.2 Plane stress simulations

In this section, the FE code developed for plane stress analyses is employed for 45° simulations. The numerical results are compared with the corresponding plane strain results and those from the homogeneous deformation analysis. For the plane stress simulations, the conventional nominal shear stress and normal stress (Fig. 5.1) are defined by $F_s/(Lt_0)$ and $F_n/(Lt_0)$ where t_0 is the initial thickness of the specimen.

The shear stress–shear deformation curves from the plane stress FE analysis, plane strain FE analysis, and homogeneous deformation analysis are compared in Fig. 5.14. It can be seen that the FE results obtained from the plane strain simple shear and plane stress simple shear codes are very close to each other. Both curves reach a maximum shear stress τ_{max} at a shear deformation of about 0.25, with the plane strain FE analysis predicting a slightly higher value. With further shearing, softening is found in both cases with the plane stress FE results exhibiting a slightly stronger softening.

Figures 5.15 a-c present contour plots of normalized equivalent plastic shear strain γ^p both for the plane stress and plane strain FE analyses. At a shear deformation of 0.25, it can be seen that the plane stress FE analysis also shows four regions of enhanced shear originating at the

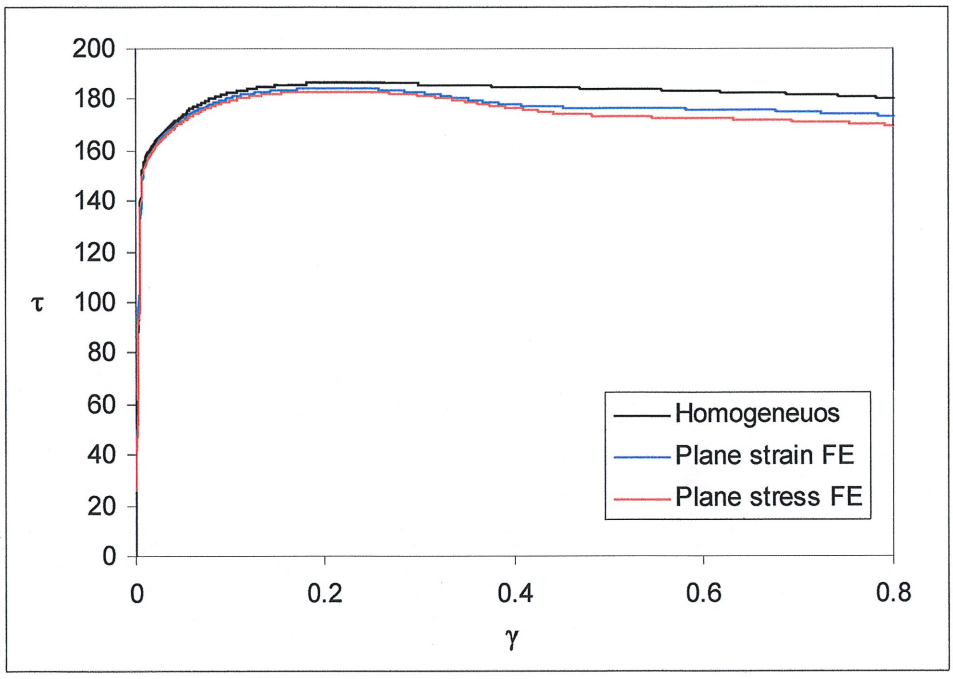

Figure 5.14 Predicted overall shear stress responses for the 45° simulations

corners of the specimen (Fig. 5.15a). However, corners A and C (Fig. 5.1) exhibit stronger localization than do the corners B and D. The enhanced shearing initiated from corners B and D have progressed further into the specimen while localization is mainly concentrated around the corners A and C.

When shear deformation has reached 0.5, it can be seen that two nearly parallel shear bands have formed just as in the plane strain FE analyses (Fig. 5.15b). The shear bands from the plane stress FE analysis are closer to the upper and lower edges of the specimen than those from the plane strain FE analysis, and the corners A and C exhibit stronger localization than the corners B and D. With further shearing, the strain concentrates in these two bands (Fig. 5.11c).

Some studies (e.g., G'Sell, 1986) have shown that variations in thickness during shear deformation are relevant only to second-order terms in the strain tensor and may thus be neglected to a first approximation. Our plane stress simulations show that this assumption is correct within the central parts of the specimen, but is not correct for the corners of the specimen

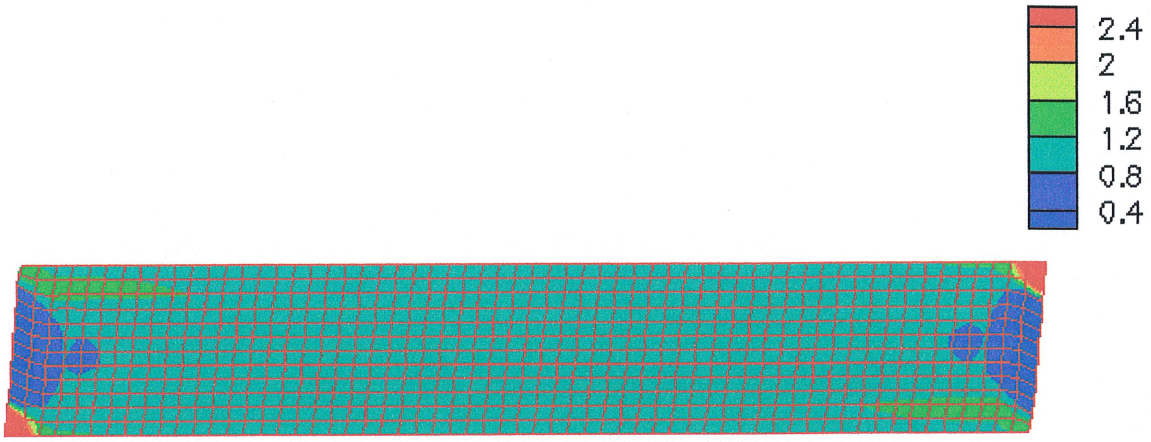

Plane stress FE analysis

Plane strain FE analysis

(a)

Plane stress FE analysis

Plane strain FE analysis

(b)

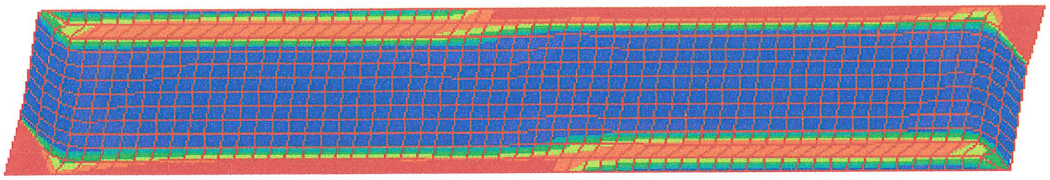

Plane stress FE analysis

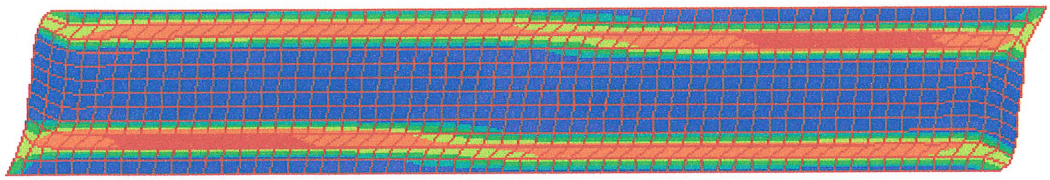

Plane strain FE analysis

(c)

Figure 5.15 Contours of normalized equivalent plastic shear strain γ^p at: (a) $\gamma = 0.25$, (b) $\gamma = 0.5$, and (c) $\gamma = 0.75$

since the thickness strains are not small enough to be neglected here (Fig. 5.16). While corners B and D are undergoing compression, corners A and C and mainly the rest of the specimen are undergoing tension at a shear deformation of 0.25 (Fig. 5.16a). This pattern changes with further shearing, at a shear deformation 0.5 (Fig. 5.16b) the centre of the top and the bottom edges of the specimen has changed its deformation mode from tension to compression. Furthermore, beginning at the corners B and D, compression is progressing towards the centre of the specimen. This compression initiated from corners B and D continues to progress towards the centre of the specimen with further shearing (Fig. 5.16c).

It has already been demonstrated that corners A and C were exhibiting stronger localization than corners B and D (Fig. 5.15). Note that the deformation modes are different for these two pairs of corners; stronger localization at corners A and C is accompanied by a deformation mode of tension, while corners B and D are undergoing compression.

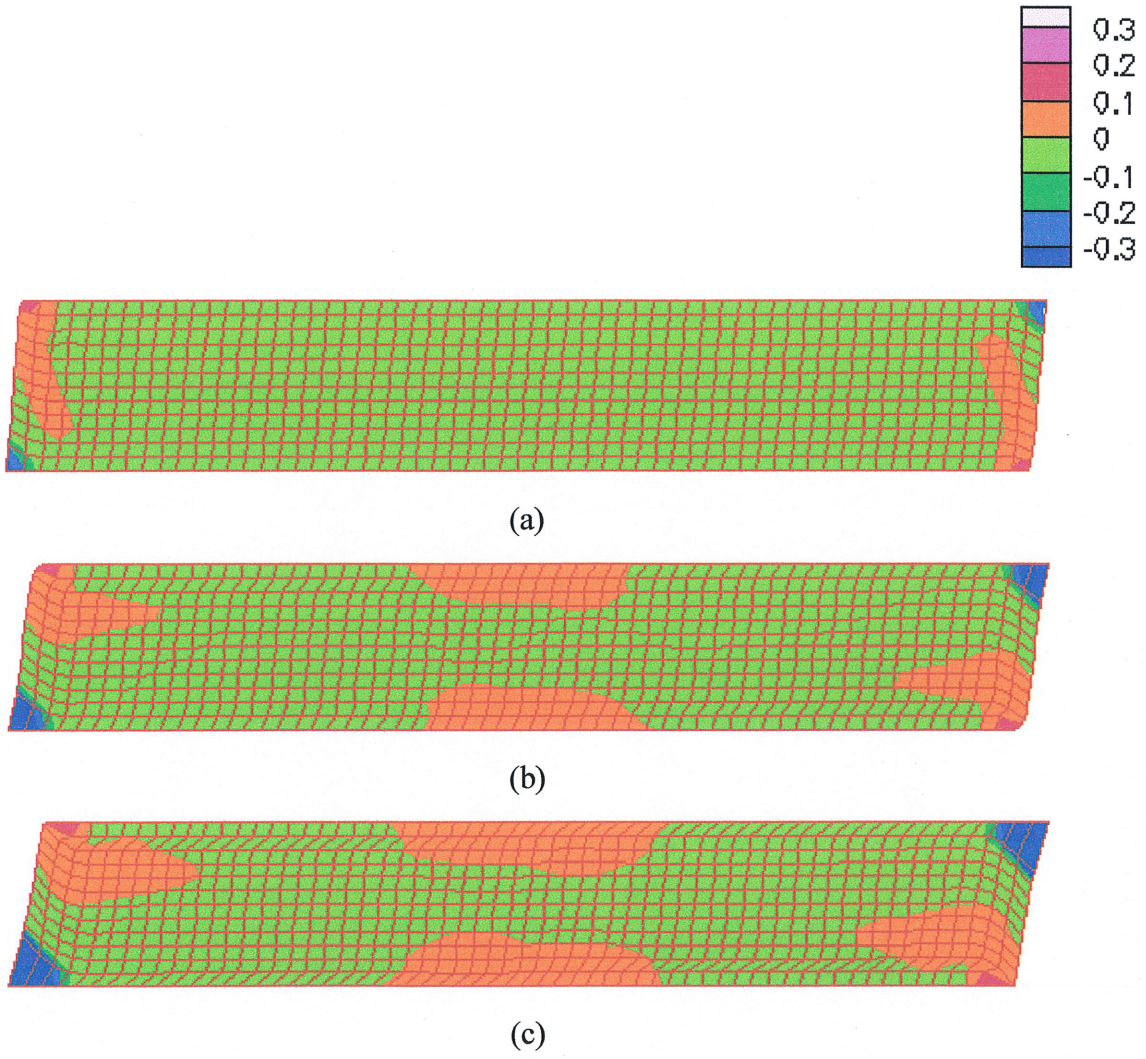

Figure 5.16 Contours of thickness strain ε_{33} at: (a) $\gamma = 0.25$, (b) $\gamma = 0.5$, and (c) $\gamma = 0.75$

5.4 Conclusion

In this chapter, the planar simple shear test has been simulated with both our plane strain and plane stress FE codes for the can-body sheet AA3004-H19. Simulations were performed for specimens rotated such that the rolling direction is at 0^0, 45^0 and 90^0 to the shearing axis. The initiation and evolution of shear bands were investigated.

The overall shear stress–shear deformation curves were found to be in good agreement with experimental results presented by Gaspérini et al. (1996). For the three orientations of

shearing considered, all curves presented a rapid hardening followed by a decreasing hardening rate, leading to the saturation of the flow stress. While softening occurred after this saturation for the 45° and TD simulations, no softening effect was observed for the RD simulation.

Our simulations based on both the plane strain and plane stress assumptions were able to predict localized deformations in the form of shear bands. Note that an imperfection was not necessary to initiate shear bands. Localized deformation started as four regions of enhanced shear appearing at the corner of the specimens. During continued deformation, these regions gradually grew into two nearly parallel shear bands for the three orientations of shearing that have been considered. It is important to mention that for the RD simulation, although the overall shear stress–shear deformation curve showed no signs of localized deformation, shear bands were nevertheless still predicted.

Experimental observations presented by Gaspérini et al. (1996) indicate that shear bands initiate from the two corners of the specimen that are undergoing compression, then they rapidly progress along the whole length of the specimen, and eventually merge. At this point, our numerical simulations are in disagreement with these experimental observations. However, this disagreement might be explained when the following numerical and theoretical concepts are considered:

- The mesh sensitivity analysis that has been performed indicated that there were no significant differences in the macroscopic features of localization for the three finite element meshes considered. Still, simulations with more than 2000 elements were not performed due to the limitations of our computers. It might be possible that refining the finite element meshes beyond the limits presented in this study might alter the macroscopic features of localized deformation.

- Our simulations have clearly indicated that neither the plane strain nor the plane stress assumption for modelling simple shear is valid at the corners of the specimen since the thickness stresses and strains are not small enough to be ignored for these assumptions, respectively. This is a very important observation and could profoundly

affect the macroscopic features of localization because shear bands initiate from the corners of the specimen. Furthermore, 3-D phenomena such as cracking and the drawing of the material from outside the gauge section, which significantly affect the overall response at large strains, cannot be taken into account in the 2-D analyses.

- The initial texture and the dislocation microstructure are important parameters governing the behaviour of materials undergoing large deformations. The polycrystal plasticity model employed in this work can account for the effects of the initial texture and its evolution on the deformation. However, it cannot account for the dislocation microstructure. Thus, the effects of some important concepts such as dense dislocation walls, microbands, or dislocation sheets are not included in our simulations.

The 2-D analyses presented in this chapter have provided a very good understanding of localized deformation occurring during simple shear. Important observations were made such as the sensitivity of the overall shear stress response and deformation distribution to the loading direction and the initiation and development of shear bands. However, the simple shear test is in fact a 3-D problem: consequently it is likely that a 3-D modelling will provide better correlation with experimental observations.

CHAPTER 6

SIMULATION OF EARING IN TEXTURED ALUMINUM SHEETS

6.1 Introduction

Ears which develop during the deep drawing of anisotropic sheets can cause major problems in the production of deep drawn containers. The cups must be trimmed to produce the correct container height and to permit the container ends to be attached properly. The trimming not only involves an extra operation, but it also creates additional scrap which must be handled and recovered. Better control and reduction of earing may eliminate these extra operations and would allow a greater yield from a sheet by permitting smaller blanks to be cut.

It is well known that these ears are initially caused by crystallographic texture; therefore many models based on the plastic slip of a single crystal or of a polycrystal have been developed. Tucker's model (1961) based on Schmid's law for a FCC single crystal, is in reasonable agreement with experiments. Later on, Kanetake et al. (1983) applied Tucker's approach for polycrystals.

Barlat et al. (1991) predicted earing for polycrystals with a model in which they analysed the flange. They made comparisons between plane strain and plane stress cases, and concluded that the plane strain assumption successfully explained the major trends of earing. Becker et al. (1993) simulated complete cup drawing for single crystals. They also predicted the initial phases of earing for polycrystals with a model involving only the flange.

Recently Balasubramanian and Anand (1998) provided results for the quantitative prediction of the punch force versus the punch displacement, the number of ears, their positions and their heights during the cup drawing of aluminum alloys. Yoon et al. (1998) studied the influence of initial back stress on the earing prediction of drawn cups for planar anisotropic aluminum sheets. Their earing predictions with initial back stress and yield function coefficients considering tensile and compressive material behaviour were in very good agreement with the experiments.

In this chapter, a finite element model for earing analysis is developed considering only the flange area of the sheet. Earing analyses are performed using the flange model, both with a

polycrystal (Chapter 3) and a phenomenological model (Barlat et al., 1991). The earing profiles are predicted for the aluminum alloys AA6111-T4 and AA5754-0 and these profiles are compared with experimental data. This work has been published in Inal et al. (2000a, 2000b).

6.2 Phenomenological constitutive model

The phenomenological yield function used in the earing simulations is that proposed by Barlat et al. (1991). They have developed a six component yield function in the form

$$\Phi = (3I_2)^{p/2}\left\{\left[2\cos\left(\frac{2\theta+\pi}{6}\right)\right]^p + \left[2\cos\left(\frac{2\theta-3\pi}{6}\right)\right]^p + \left[-2\cos\left(\frac{2\theta+5\pi}{6}\right)\right]^p\right\} \tag{6-1}$$

where

$$\theta = \arccos\left(\frac{I_3}{I_2^{3/2}}\right) \tag{6-2}$$

The stress deviator invariants in equation (6-2) take the following form

$$I_2 = \frac{\{fF\}^2 + \{gG\}^2 + \{hH\}^2}{3} + \frac{(aA-cC)^2 + (cC-bB)^2 + (bB-aA)^2}{54} \tag{6-3}$$

$$I_3 = \frac{(cC-bB)(aA-cC)(bB-aA)}{54} + fghFGH - \frac{(cC-bB)\{fF\}^2 + (aA-cC)\{gG\}^2 + (bB-aA)\{hH\}^2}{6} \tag{6-4}$$

where a, b, c, f, g and h are constants and, with the Bishop and Hill (1951a,b) notation for the stresses, the quantities A, B, C, F, G and H can be presented in the form

$$A = \sigma_{yy} - \sigma_{zz} \qquad B = \sigma_{zz} - \sigma_{xx} \qquad C = \sigma_{xx} - \sigma_{yy}$$

$$F = \sigma_{yz} \qquad G = \sigma_{zx} \qquad H = \sigma_{xy} \tag{6-5}$$

This anisotropic yield function is orthotropic and shall henceforth be referred to as yield function Yld91 (Barlat et al., 1997) in this chapter.

6.3 Flange model

Complete cup drawing simulations have shown that, once the sheet enters the die radius, very little additional earing deformations occur. This suggests that a simple model can be used to describe the initial phases of earing (Becker et al., 1993). Accordingly, a finite element model considering only the deformation in the flange area is employed in this chapter. Our model is based on the plane strain assumption, so that there is no change in the thickness of the sheet. In addition, the effects of friction are not accounted for. Figure 6.1 shows the actual cup drawing geometry.

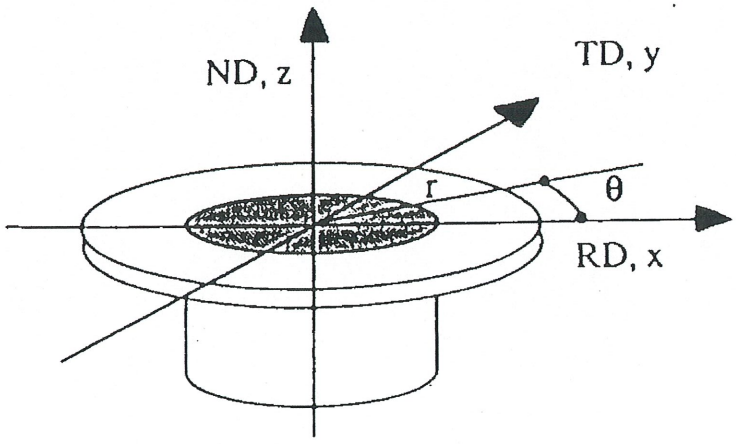

Figure 6.1 Cup drawing geometry

The finite element mesh used in the flange model simulations is presented in Fig. 6.2. Assuming orthotropic material symmetry, only one fourth of the circular blank is modelled with 15 rows of elements both radially and circumferentially. The initial ratio of the outer flange radius to the inner flange radius was taken as two, which corresponds to the experimental cases used later for comparison. Inward radial displacements on the inner ring of the nodes are

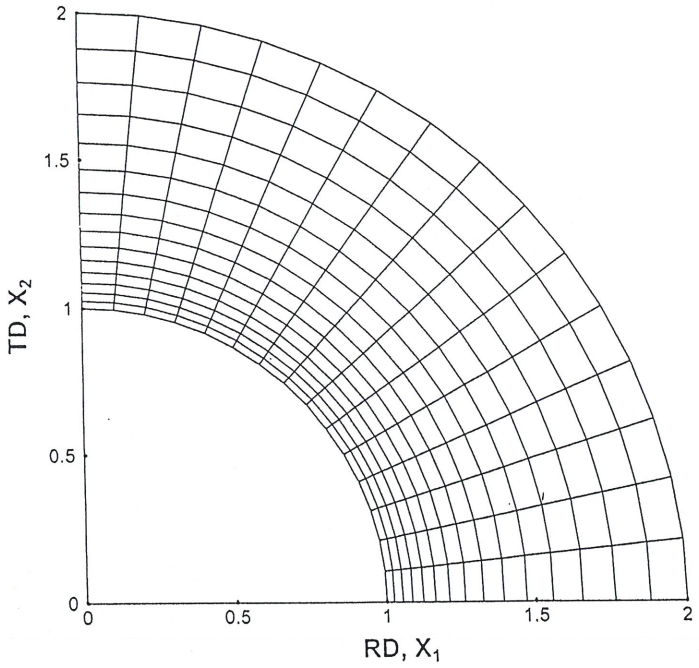

Figure 6.2 Finite element mesh

prescribed. Once a ring element has passed inside the die radius, these elements are removed from the analysis. The same boundary conditions are then applied to the nodes at the inside of the next ring of elements to continue the deformation process.

6.4 Results and discussion

Earing profiles were investigated for the aluminum alloys AA6111-T4 and AA5754-0. Figures 6.3 a-b present the initial textures of these alloys in terms of {111} stereographic pole figures, with 476 and 384 crystals respectively. Here X_1 and X_2 refer to the rolling and transverse directions of the sheet, respectively.

The single slip hardening law presented in (3.19) is used in the simulations, and the relevant material properties are given in Table 6.1. These properties were obtained by fitting the uniaxial stress–strain curve obtained by crystal plasticity to the uniaxial stress–strain curve measured experimentally (Wu *et al.*, 1998). The slip system reference plastic shearing rate $\dot{\gamma}_0$ and the slip rate sensitivity parameter m are taken as $\dot{\gamma}_0 = 0.001 s^{-1}$ and m = 0.002, respectively, for the two alloys.

Alloy	Crystal elastic constants (GPa)			Hardening parameters			
	C_{11}	C_{12}	C_{44}	τ_0 (MPa)	h_0/τ_0	n	q
AA6111.T4	230	132	60	47	30	0.230	1
AA5754.0	230	132	60	21	182	0.245	1

Table 6.1 Material constants for the crystal plasticity model.

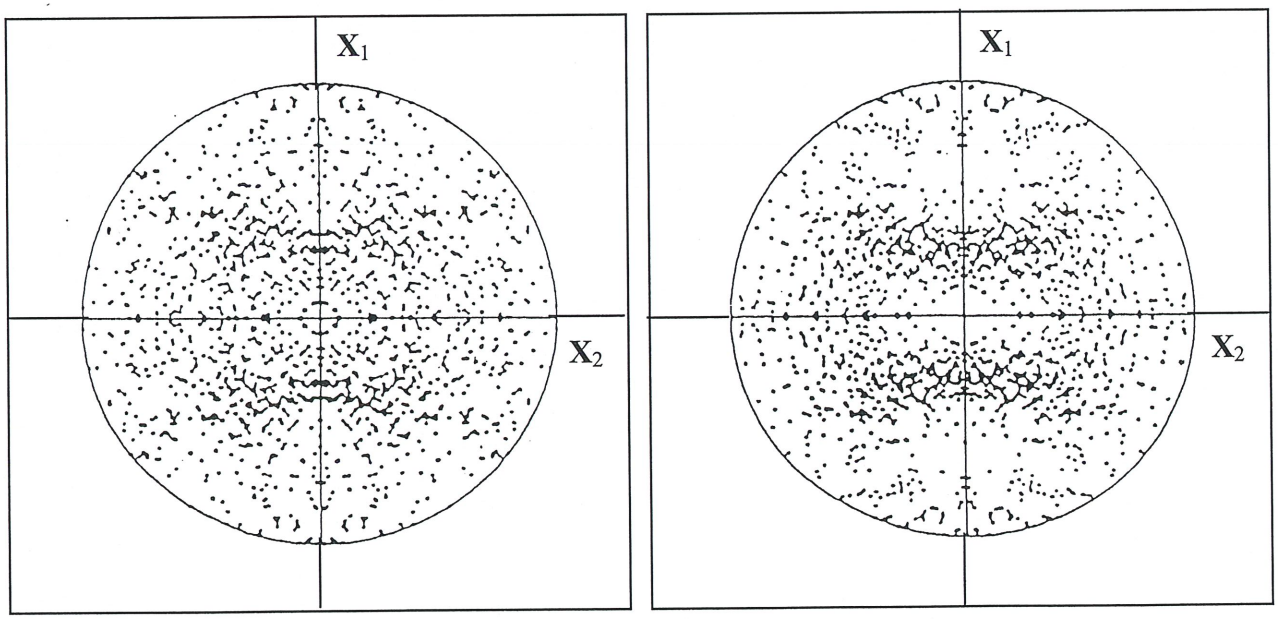

(a) (b)

Figure 6.3 Initial texture represented by {111} stereographic pole figure for : (a) AA6111-T4, and (b) AA5754-0

Numerical simulations for the alloys AA6111-T4 and AA5754-0 predict four ears at approximately 0 and 90 degrees to the rolling direction. Comparisons between the predicted earing profiles and the experimental earing profiles for these two alloys are presented in Figs. 6.4

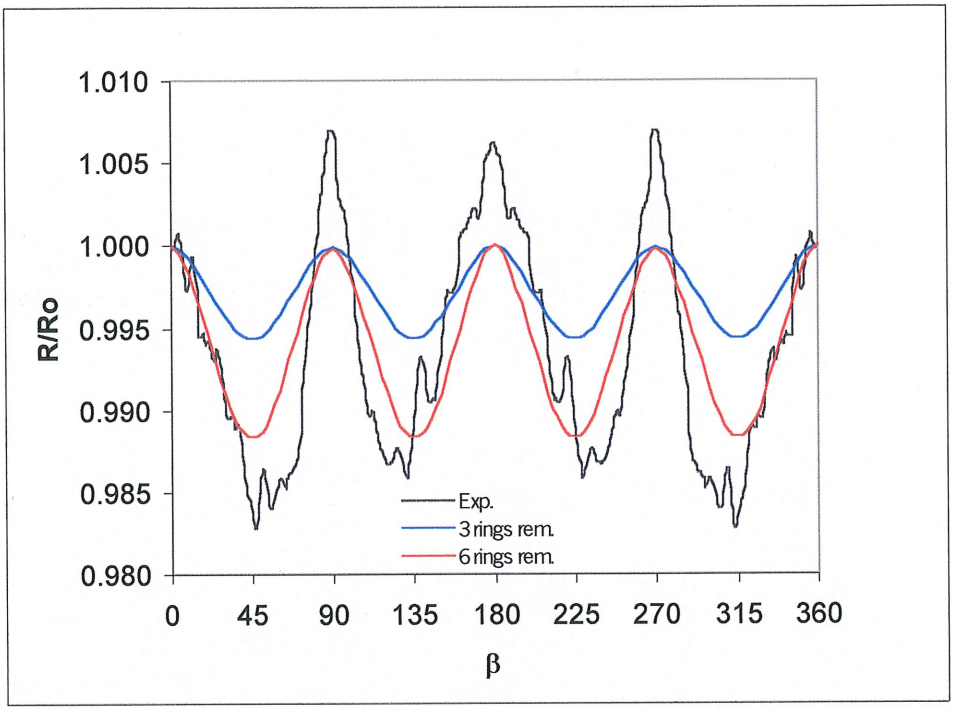

Figure 6.4 Comparison of the experimental and simulated (polycrystal model) earing profile for AA6111-T4

and 6.5 respectively, where ψ is the angle (in degrees) from the rolling direction and R/Ro is the ratio of the current flange radius at the angle ψ to the current flange radius in the rolling direction (0 degrees). All of these simulations were terminated after the sixth ring of elements was removed from the analysis.

The effect of texture evolution on the initial earing profile has also been investigated. Simulations show that texture evolution will not have a major effect in the initial phases of earing. This can be seen in the curves of Fig. 6.6, where a comparison between the earing profiles

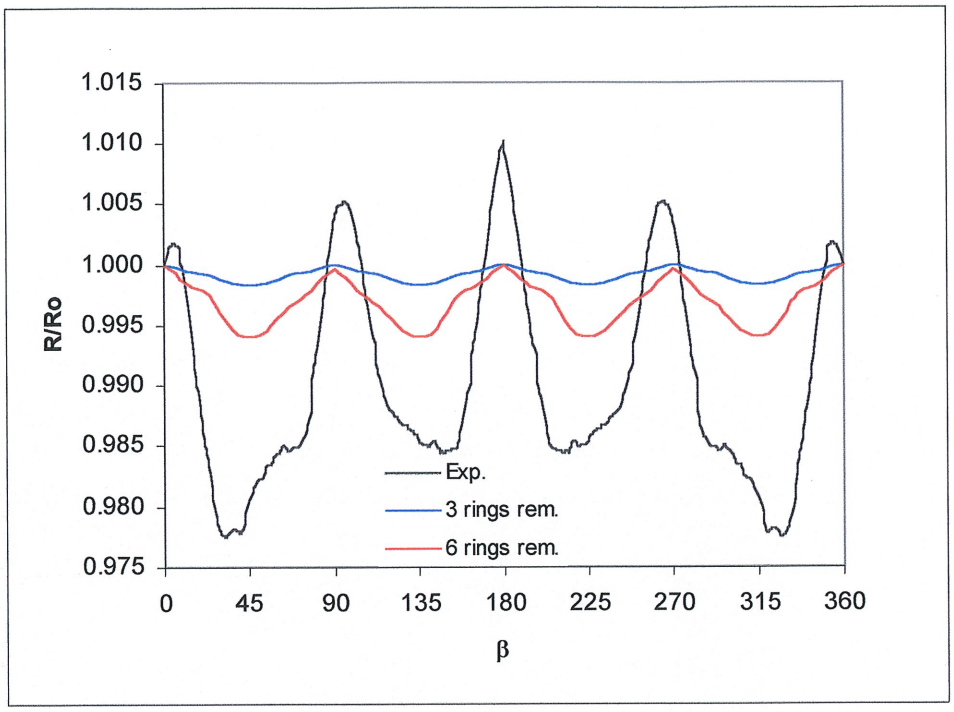

Figure 6.5 Comparison of the experimental and simulated (polycrystal model) earing profile for AA5754-0

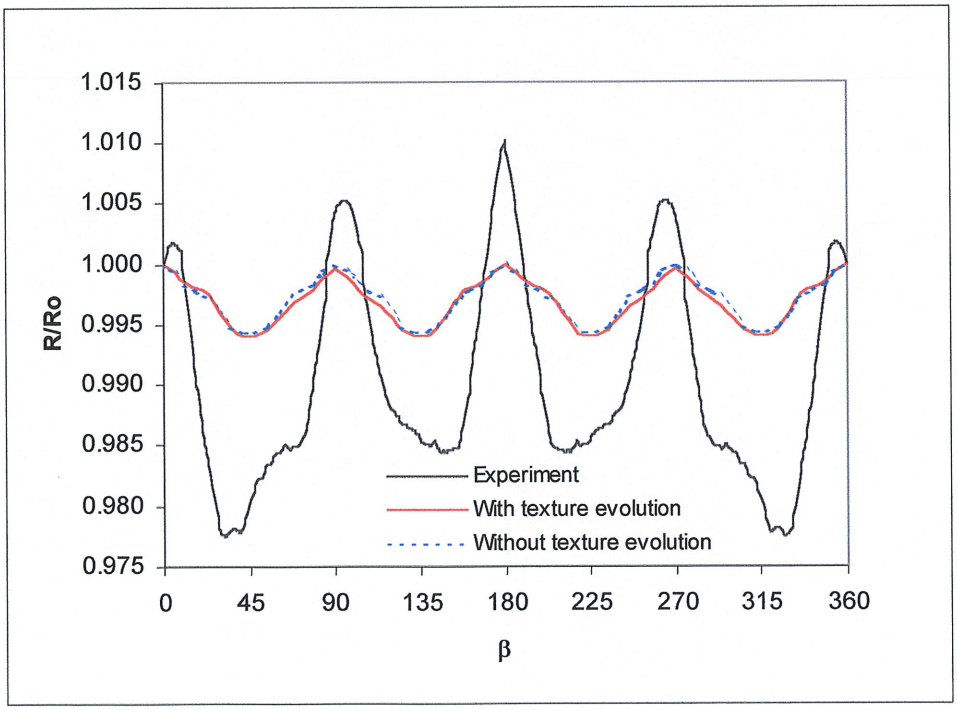

Figure 6.6 Comparison of the earing profile for AA5754-0 predicted by the polycrystal model with and without texture evolution

obtained by the polycrystal model with and without texture evolution is presented. Again the analysis was stopped when the sixth ring of elements was removed from the flange.

The yield function Yld91 has also been used for the earing simulations of the aluminum alloys AA6111-T4 and AA5754-0. Hayashida et al. (1995) used the ABAQUS FEM code in which the yield function Yld91 was implemented as a material user subroutine. They have simulated the drawing of a circular cup and predicted the cup height (earing) profile for an Al-5% Mg sheet sample. Their prediction was not in total agreement with the experiments. By contrast, the present flange model analysis with the yield function Yld91 was able to predict the initial phases of earing for the alloys AA6111-T4 and AA5754-0.

The material constants for the yield function Yld91 were determined by crystal plasticity and are presented in Table 6.2. The exponent p used in Equation (6.1) has been computed by fitting the yield surface obtained from the yield function Yld91 to the one obtained from crystal plasticity. Figures 6.7 and 6.8 show that good agreement was obtained when p was taken as 7.5 for the alloy AA6111-T4 and 8 for the alloy AA5754-0. For these alloys, our flange model based on the yield function Yld91 predicted correctly the four ears at approximately 0 and 90 degrees to the rolling direction, as shown in Figs. 6.9 and 6.10 respectively.

Alloy	p	A	b	c	f	g	h
AA6111-T4	7.5	1.06	1.003	0.9974	0.8385	0.8586	0.8805
AA5754-0	8	0.9802	1.008	0.9922	0.8786	0.88	0.8945

Table 6.2. Material constants for the yield function Yld91

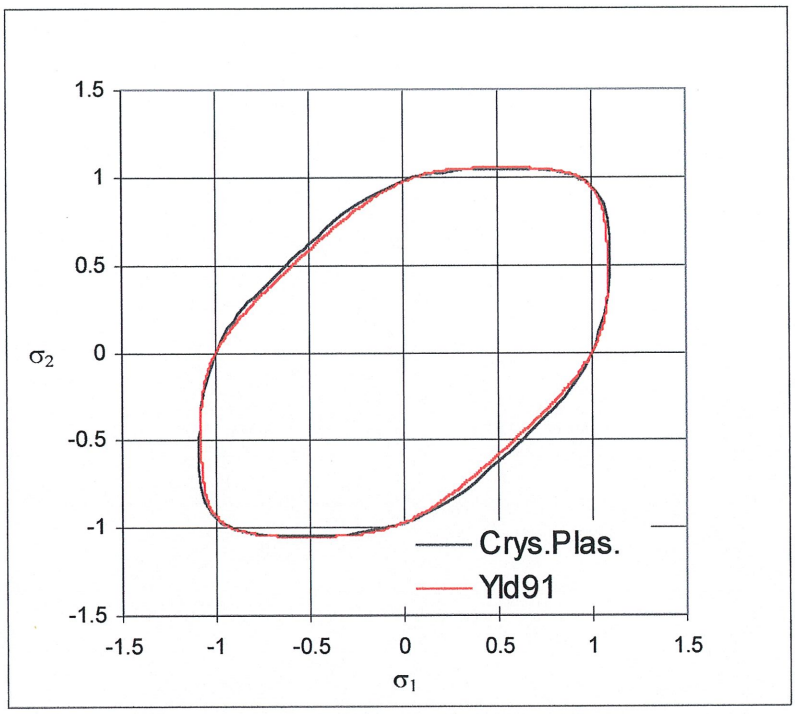

Figure 6.7 Comparison of yield surfaces for AA6111-T4 obtained by the yield function Yld91 and crystal plasticity

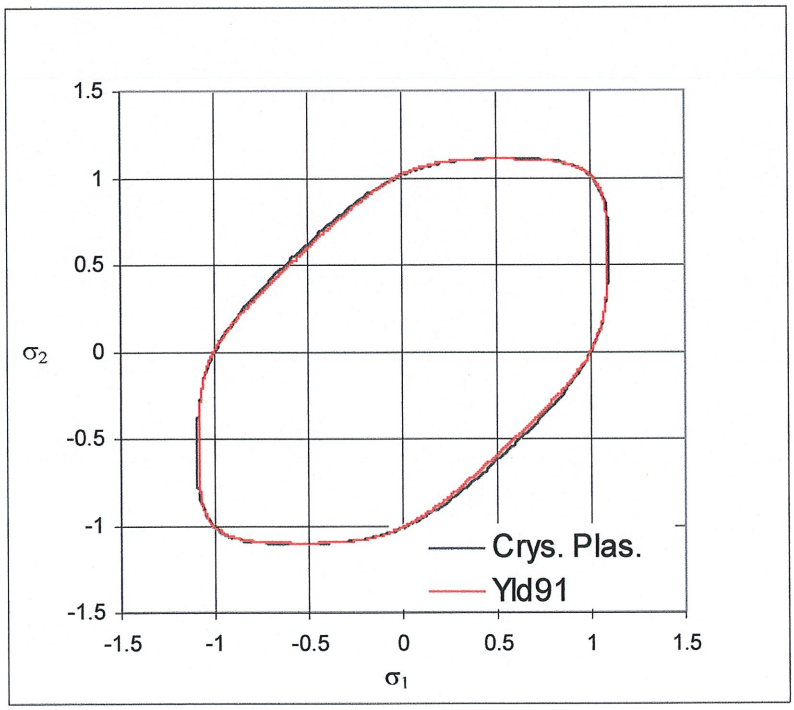

Figure 6.8 Comparison of yield surfaces for AA5754-0 obtained by the yield function Yld91 and crystal plasticity

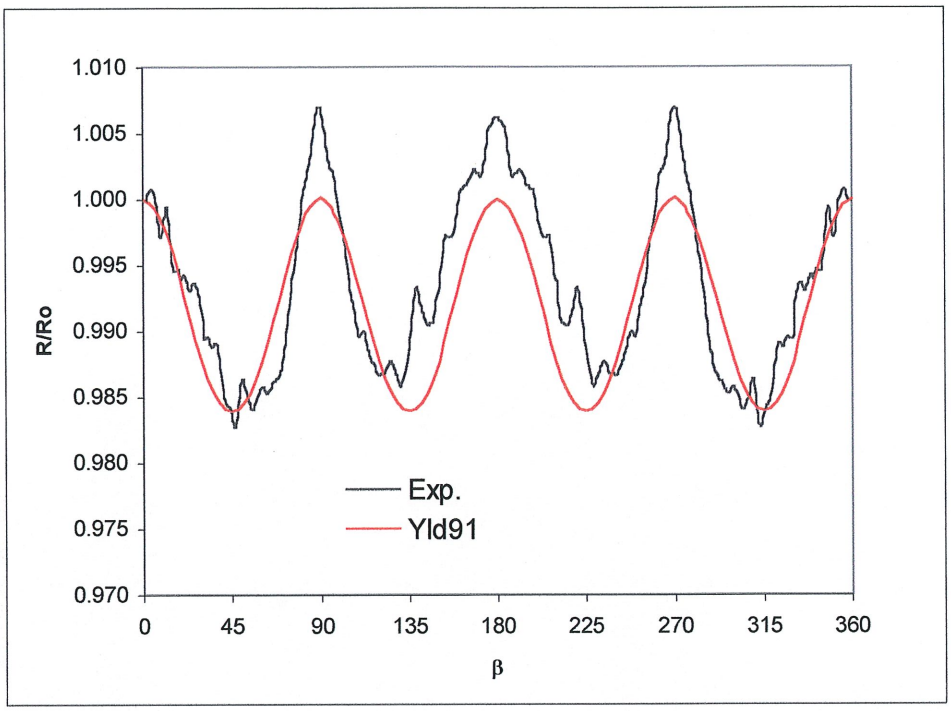

Figure 6.9 Comparison of the experimental and simulated (phenomenological model) earing profile for AA6111-T4

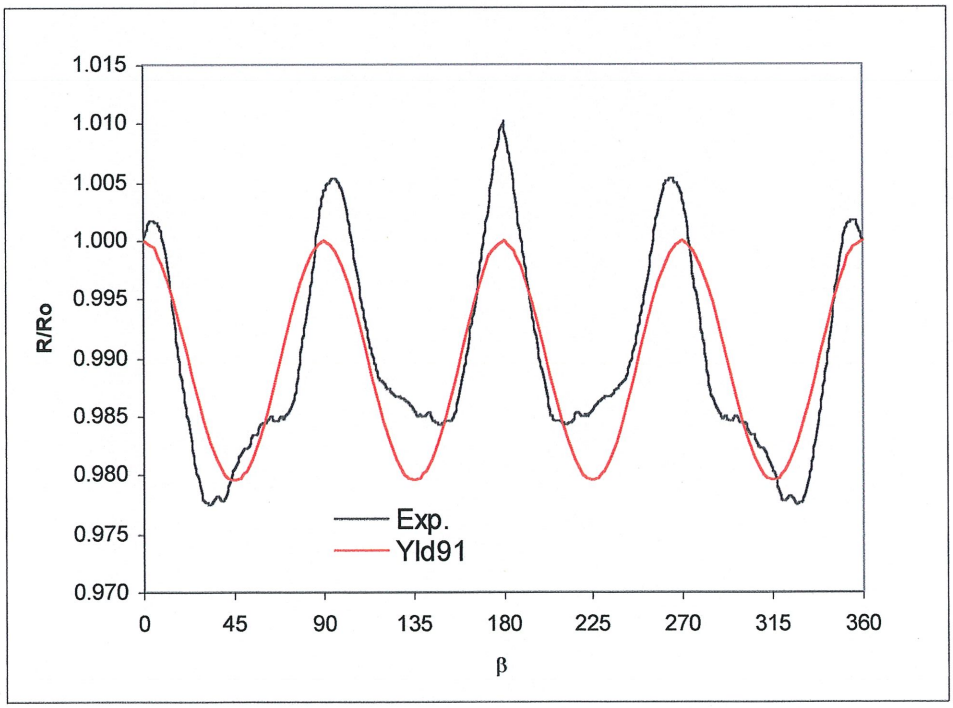

Figure 6.10 Comparison of the experimental and simulated (phenomenological model) earing profile for AA5754-0

6.5 Conclusion

In this chapter we have simulated earing for the aluminum alloys AA6111-T4 and AA5754-0. Accurate characterization of the material and of the drawing process is essential for predictive earing models. The flange model presented in this chapter is an adequate geometric model for earing simulations. The basic assumption underlying the flange model is that ears start to form in the flange, and the final positions of ears coincide with initial positions. This assumption is well supported by many experimental observations.

Earing analyses of the flange have been performed based on both the polycrystal and the phenomenological model (Yld91). Both models were able to successfully predict the number and position of ears for the aluminum alloys AA6111-T4 and AA5754-0. However, it is noteworthy to mention that results obtained using the phenomenological model were found to be somewhat inconsistent; when different values of the exponent p (Equation 6.1) were used (all providing yield surfaces with very good agreement to the yield surface obtained from crystal plasticity), completely different earing profiles were obtained.

The simulations showed that ears develop in the early phases of deformation. As these ears are caused mainly by the initial texture of the sheet, it was observed that the evolution of texture does not have a major effect on the initial earing profiles. Although texture evolution does not have a major effect on the positions of the ears, it has a prominent effect on the cup heights. As a result, it is obvious that accurate predictions of the cup heights must include the effect of texture evolution.

Even though the proposed flange model provides useful information for the initial phases of earing, it does not include some factors which could influence the earing, such as friction. The surface of the sheet is textured during the rolling process, and there is no reason to expect that friction conditions would be the same in the rolling and transverse directions. Thus, predictions could probably be improved with full cup drawing simulations including the anisotropic friction conditions. Also the effects of grain shapes, precipitates, and special inter-grain compatibility

arrangements could be included in the simulations since these kinematic restrictions may also affect earing predictions.

CHAPTER 7

GENERAL CONCLUSION

7.1 Finite element modelling of FCC polycrystals

The overall objective of this research was to incorporate the concepts of crystal plasticity into finite element models in order to more accurately simulate sheet metal forming processes and localized deformation phenomena. For this purpose, both plane strain and plane stress FE codes were developed based on crystal plasticity theory. These FE codes incorporate parallel computing algorithms so that simulations could be performed with models containing sufficiently large numbers of elements.

The numerical simulations presented in this thesis are based on a rate-sensitive Taylor type polycrystal model. The long standing problem of nonuniqueness in the choice of active slip systems in the rate independent analysis is overcome by using a rate dependent constitutive model. The Taylor model has been chosen to obtain the constitutive response of a polycrystal comprised of many grains since it is in reasonably good agreement with experiments for the evolution of texture and the overall stress–strain response of single-phase FCC metals. This model accounts for the initial texture, the evolution of the microstructure and microscopic properties, such as the slip-induced hardening and the crystallographic texture, and inherently includes the effects of deformation induced anisotropy.

The finite element method offers the capability to simulate deformations that are spatially heterogeneous, that are governed by nonlinear equations, and that are controlled by properties that evolve with deformation. Finite element formulations combined with polycrystal plasticity can provide powerful tools for simulations of complex forming processes. A major factor in the successful combination of polycrystal plasticity and the finite element method for sheet metal forming operations is the availability of modern computing resources. Algorithms developed to take advantage of parallel computing architectures render crystal plasticity based simulations feasible with realistic models. In general, Taylor type polycrystal models are ideally suited for the parallelization of the computational procedures. Especially, when CPU time is considered, the simulations fall in the category of "embarrassingly parallel" applications, and they provide significant computational improvements. However, such "embarrassingly parallel" (e.g., Sorensen and Andersen, 1996) applications are strictly feasible only if the total program size fits

within a single processor of the parallel computer. This was not the case for the simulations presented in this thesis. Data distributing parallel computing algorithms had to be developed in order to perform simulations with large models. These algorithms distributed grain level data between the processors, so that each processor was used to its maximum capacity. Thus, simulations could be performed using the total memory of all processors combined.

The deformation characteristics of single crystals and polycrystals were described first in this research. Various polycrystal deformation theories were reviewed and their advantages and disadvantages were discussed. Special attention was paid to the Taylor polycrystal model since our simulations were based on this model. Next the rate-sensitive polycrystal plasticity formulation proposed by Asaro and Needleman (1985) was presented in detail. This was followed by the development of both plane strain and plane stress FE codes based on a Lagrangian formulation of the field equations. Parallel computing algorithms developed to distribute grain level data were presented and both the rate-sensitive Taylor type polycrystal model and the parallel computing algorithms were implemented to the FE codes. These numerical models were used to simulate various sheet metal forming processes.

7.2 Instability and localization phenomena

The first application presented was an investigation of instability and localized deformation phenomena in the rolled aluminum sheet alloy AA3004-H19 under tension. Simulations were performed with both the plane strain and plane stress FE codes. For the plane strain analyses, an initial thickness imperfection was assumed to trigger localized deformation. No initial imperfection was considered for the plane stress analyses where localized deformation was triggered as a result of the so called "built-in" boundary conditions.

Mesh sensitivity studies were first performed. These studies (where finer meshes were used without changing the element aspect ratio) have shown that, for the meshes considered, mesh sensitivity did not have a significant effect on the overall stress–strain curves and deformation patterns. However, refining the meshes resulted in narrower and sharper shear bands with a stronger softening effect in the stress–strain curves.

Simulations of tension have showed that localization during tensile straining occurs in two modes. The initiation of a neck is the indication of localized deformation for both modes. For the rate dependent analysis considered, the onset of necking is defined by the attainment of the maximum stress at the end section of the specimen, away from the neck. Once a neck is initiated, either the deformation continues with strain localizing progressively in this neck, or it triggers the formation of shear bands. The attainment of the maximum stress at the centre of the specimen was taken as the onset of shear banding.

The studies presented in this thesis show that there are a number of factors contributing to the development of localization phenomena. Texture evolution is one of the most important factors in the prediction of localized deformation. When texture evolution was not included in the analysis, the "geometric softening" effect that lead to localized shearing did not occur. As a result, shear band formation was completely precluded from the localization mode. This observation explains the inability of phenomenological plasticity models with a smooth yield surface to predict shear bands at realistic strain levels (e.g., Tvergaard et al., 1981).

Another important factor in localized deformation is the slip-rate sensitivity. It is well known that increasing the slip-rate sensitivity increases the ductility as it will delay the formation of localization modes such as shear bands or necking. When slip-rate sensitivity was increased, not only was the formation of nonuniform deformation delayed, but increasing it to certain values also completely precluded shear banding.

Simulations have shown that strain softening behaviour is not necessarily required to predict instabilities and localized deformations as necking and shear banding were indeed predicted in the presence of strain hardening. However, the rate of strain hardening does play a key role in the determination of the localization mode; increasing the rate of strain hardening eventually leads to the disappearance of shear banding from the localization mode.

The loading direction did not have any effect on the localization mode; for all loading directions considered in this thesis, the localization mode was shear banding. However, the loading direction did have a significant effect on the overall stress response and the shear band

pattern. For example, two shear bands were predicted for uniaxial tension along the RD, while only a single shear band was predicted for uniaxial tension along 1^0 from the RD.

Understanding and characterizing the large strain behaviour of thin metals is crucial to the metal forming industry since many forming operations involve large strains. Recent experimental research has indicated that the planar simple shear test can be used to characterize the plastic behaviour of thin sheet metals at large to very large strains. Thus, one application considered in this thesis was the large strain behaviour of the rolled aluminum sheet alloy AA3004-H19 under planar simple shear.

Simulations were performed for shearing along the RD, 45° from the RD, and along the TD with both the plane strain and plane stress FE codes. The initiation and evolution of shear bands were investigated in detail. In the analysis, an initial imperfection was not necessary to initiate shear bands. For all orientations considered, localized deformation started as four regions of enhanced shear appearing at the corners of the specimens. With further shearing, these regions gradually grew into two nearly parallel shear bands. The shear bands predicted from the plane stress FE code were closer to the edges of the specimen than those predicted with the plane strain FE code.

The shearing direction relative to the RD affected the overall shear stress–strain curves and the sharpness of the shear bands. For the three orientations of shearing considered, all curves presented a rapid hardening followed by a decreasing hardening rate leading to saturation of the flow stress. Softening occurred after this saturation for shearing along 45° from the RD and TD indicating localized deformation. However, softening was not observed for shearing along the RD; nevertheless, localized deformation in the form of shear bands was still predicted.

7.3 Modelling of earing in textured aluminum sheets

The last application presented in this thesis was the prediction of earing during the deep drawing of textured aluminum sheets. A simple flange model was developed to simulate the early phases of earing. Earing simulations with the flange model were performed both with the

polycrystal model and the phenomenological model proposed by Barlat et al. (1991) for the rolled sheet aluminum alloys AA6111-T4 and AA5754-0. Simulations performed with both these models were able to correctly predict the initial phases of earing for the two rolled aluminum sheet alloys considered.

The numerical analyses showed that ears develop in the early phases of deformation. Texture evolution had no major effect on the number and positions of the ears; similar earing profiles were predicted from simulations where texture evolution was both included and excluded. It should be mentioned that the main purpose of the deep drawing simulations presented in this thesis was to predict the initial number and position of the ears, not to predict accurately the cup heights. It is obvious that accurate simulation of the final heights of the ears in the fully drawn cups require the modelling of the complete deep drawing process and the correct representation of the friction conditions.

7.4 Future work

The results presented in this thesis show that many sheet metal forming operations can be simulated by 2-D models. These models not only provide a better understanding of metal forming processes, but also provide information that can be used to control product quality. However, metal forming operations are in reality 3-D problems. For example, it is known that the state of stress at the neck area during stretching is triaxial. When simple shearing is considered, the cracking and the drawing of the material from outside the gauge section cannot be taken into account in the 2-D analysis. Thus, it is expected that metal forming modelling could be improved by simulations with 3-D models, and an immediate sequel to this thesis work would be the development of a 3-D FE model. Although all simulations presented in this thesis were performed with 2-D models, the constitutive model and computational procedures already incorporate the full 3-D slip structure of FCC crystals. Furthermore the parallel computer algorithms that have been developed need little modification for applications with 3-D models. As a first application of a 3-D FE code, the metal forming processes presented in this thesis could be re-simulated. The next step could be the modification of both the crystal plasticity constitutive law and numerical model to incorporate the effects of various features such as texture gradients,

back stresses, residual stresses, and friction. Finally, it should be mentioned that although the numerical analyses presented in this thesis were restricted to FCC polycrystalline metals, it is not difficult in principle to adopt these analyses to other types of polycrystals, such as BCC and HCP metals.

Bibliography

ACHARYA, A., BEAUDOIN, A. J. (2000): "Grain-size effect in viscoplastic polycrystals at moderate strains," *Journal of the Mechanics and Physics of Solids,* **48**, 2213-2230.

ACHARYA, A., BASSANI, J. L. (2000): "Lattice incompatibility and a gradient theory of crystals plasticity," *Journal of the Mechanics and Physics of Solids*, **48**, 1565-1595.

ANAND, L., KALIDINDI, S. R. (1994): "The process of shear band formation in plane strain compression of fcc metals: effects of crystallographic texture," *Mechanics of Materials*, **17**, 223-243.

ASARO, R. J. (1979): "Geometrical effects in the homogeneous deformation of ductile single crystals," *Acta Metallurgica*, **27**, 445-453.

ASARO, R. J., NEEDLEMAN, A. (1985): "Texture development and strain hardening in rate dependent polycrystals," *Acta Metallurgica*, **33**, 923-953.

BALASUBRAMANIAN, S., ANAND, L. (1998): "Polycrystalline plasticity: application to earing in cup drawing of A12008-T4 sheet," *ASME Journal of Applied Mechanics*, **65**, 268-271.

BARLAT, F. (1989): "Forming limit diagrams – predictions based on some microstructural aspects of materials," Forming Limit Diagrams : Concepts, Methods and Applications, R.H. Wagoner, K.S. Chan and S.P. Keeler, Editors, The Minerals, Metals and Materials Society, 275-301.

BARLAT, F. (1987): "Crystallographic texture, anisotropic yield surfaces and forming limits of sheet metals," *Materials Science and Technology*, **91**, 55-72.

BARLAT, F., MAEDA, Y., CHUNG, K., YANAGAWA, M., BREM, J. C., HAYASHIDA, Y., LEGE, D. J., MATSUI, K., MURTHA, S. J., HATTORI, S., BECKER, R. C., MAKOSEY, S. (1997): "Yield function development for aluminum alloy sheets," *Journal of the Mechanics and Physics of Solids*, **45**, 1727-1763.

BARLAT, F., LEGE, D. J., BREM, J. C. (1991): "A six-component yield function for anisotropic materials," *International Journal of Plasticity*, **7**, 693-712.

BARLAT, F., PANCHANADEESWARAN, S., RICHMOND, O. (1991): "Earing in cup drawing face-centered cubic single crystals and polycrystals," *Metallurgical Transactions*, **22A**, 1525-1534.

BARLAT, F., RICHMOND, O. (1987): "Prediction of tricomponent plane stress yield surfaces and associated flow and failure behaviour of strongly textured FCC polycrystalline sheets," *Materials Science and Technology*, **95**, 15-29.

BASSANI, J. L. (1994): "Plastic flow of crystals," *Advances in Applied Mechanics*, **30**, 191-258.

BASSANI, J. L., WU, T. (1991): "Latent hardening in single crystals – II: analytical characterization and predictions," *Proceedings of the Royal Society of London*, **A435**, 21-41.

BASSANI, J. L, HUTCHINSON, J. W., NEALE, K. W. (1979): "On the prediction of necking in anisotropic sheets," Metal Forming Plasticity, H. Lippman, Editor, Springer, 1-13.

BEAUDOIN, A. J., ACHARYA, A., CHEN, S. R., KORZEKWA, D. A. and STOUT, M. G. (2000): "Consideration of grain-size effect and kinetics in the plastic deformation of metal polycrystals," *Acta Materialia*, **48**, 3409-3423.

BEAUDOIN, A. J., DAWSON, P. R., MATHUR, K. K. and KOCKS, U. F. (1995): "A hybrid finite element formulation for polycrystal plasticity with consideration of macrostructural and microstructural linking," *International Journal of Plasticity*, **11**, 501-521.

BEAUDOIN, A. J., MATHUR, K. K., DAWSON, P. R., JOHNSON, G. C. (1993): "Three-dimensional deformation process simulation with explicit use of polycrystal plasticity models," *International Journal of Plasticity*, **9**, 833-860.

BECKER, R., SMELSER, R. E., PANCHANADEESWARAN, S. (1993): "Simulations of earing in aluminium single crystals and polycrystals," *Modelling and Simulation in Materials Science Engineering*, **1**, 203-224.

BERVEILLER, M., ZAOUI, A. (1979): "An extension of the self-consistent scheme to plastically flowing crystals," *Journal of the Mechanics and Physics of Solids*, **26**, 325-344.

BISHOP, J. F. W., HILL, R. (1951a): "A theory of the plastic distortion of a polycrystalline aggregate under combined stresses," *Philosophical Magazine*, **42**, 414-427.

BISHOP, J. F. W., HILL, R. (1951b): "A theoretical derivation of the plastic properties of a polycrystalline face centered metal," *Philosophical Magazine*, **42**, 1298-1307.

BRONKHORST, C. A., KALIDINDI, S. R., ANAND, L. (1992): "Polycrystalline plasticity and the evolution of crystallographic texture in fcc metals," *Philosophical Transactions of the Royal Society of London*, **A341**, 443-477.

BROWN, S., KIM, K., ANAND, L. (1989): "An internal variable constitutive model for hot working metals," *International Journal of Plasticity*, **5**, 95-130.

BUDIANSKY, B., WU, T. T. (1962): "Theoretical prediction of plastic strains of polycrystals," *Proceedings of the 4th U. S. National Congress of Applied Mechanics*, ASME, 1175-1185.

CANOVA, G. R., FRESSENGEAS, C., MOLINARI, A., KOCKS, U. F. (1988): "Effects of rate sensitivity on slip system activity and lattice rotation," *Acta Metallurgica*, **36**, 1961-1970.

CANOVA, G. R., KOCKS, U. F., JONAS, J. J. (1984): "Theory of torsion texture development," *Acta Metallurgica*, **32**, 211-226.

CHAN, K. S., KOSS, D. A., GHOSH, A. K. (1984): "Localized necking of sheet at negative minor strains," *Metallurgical Transactions*, **15A**, 323-329.

CHANG Y. W., ASARO, R. J. (1981): "An experimental study of shear localization in aluminum-copper single crystals," *Acta Metallurgica*, **29**, 241-254.

CHIN, G. Y., MAMMEL, W. L. (1969): "Generalisation and equivalence of the minimum work (Taylor) and maximum work (Bishop-Hill) principles for crystal plasticity," *Transactions of the Metallurgical Society of AIME*, **245**, 1211-1214.

CHOI, S.–H., BREM, J. C., BARLAT, F., OH, K. H. (2000): "Macroscopic anisotropy in AA5019A sheets," *Acta Materialia*, **48**, 1853-1863.

CONSIDÉRE, M. (1885): "L'emploi du fer et de l'acier dans les constructions", *Annales des Ponts et Chaussées*, **9**, 574-775.

DAWSON, P., BOYCE, D., MACEWEN, S. R., ROGGE, R. (1999): "Intercrystalline stresses in metal polycrystals: comparing simulations to diffraction experiments," *ICOTOM 12*, Montreal, NRC Research Press, **1**, 505-510.

DAWSON, P. R., MARIN, E. B. (1998) : "Computational mechanics for metal deformation processes using polycrystal plasticity," *Advances in Applied Mechanics*, **34**, 78-169.

ESHELBY, J. D. (1957): "The deformation behaviour of the elastic field of an ellipsoidal inclusion and related problems," *Proceedings of the Royal Society of London*, **A241**, 376-396.

FLECK, N. A., HUTCHINSON, J. W. (1997): "Strain gradient plasticity," *Advances in Applied Mechanics*, **33**, 296-361.

FLECK, N. A., HUTCHINSON, J. W. (1993): "A phenomenological theory for strain gradient effects in plasticity," *Journal of the Mechanics and Physics of Solids*, **41**, 1825-1857.

GASPÉRINI, M., PINNA, C., SWIATNICKI, W. (1996): "Microstructure evolution and strain localization during shear deformation of an aluminum alloy," *Acta Materialia*, **10**, 4195-4208.

G'SELL, C. (1986): "Plastic deformation of glassy polymers: constitutive equations and macromolecular mechanisms," Strengths of Metals and Alloys, H. J. McQueen et al., Editors, Pergamon Press, 1943-1982.

HARREN, S. V., LOWE, T. C., ASARO, R. J., NEEDLEMAN, A. (1989): "Analysis of large-strain shear in rate-dependent face-centred cubic polycrystals: correlation of micro- and macromechanics," *Philosophical Transactions of the Royal Society of London*, **A328**, 443-500.

HARREN, S. V., DÈVE, H. E., ASARO, R. J. (1988): "Shear band formation in plane strain compression," *Acta Metallurgica*, **9**, 2435-2480.

HILL, R. (1965): "Continuum micro-mechanics of elasto-plastic polycrystals," *Journal of the Mechanics and Physics of Solids*, **13**, 89-101.

HILL, R. (1952): "On discontinuous plastic states, with special reference to localized necking in thin sheets," *Journal of the Mechanics and Physics of Solids*, **1**, 19-30.

HILL, R., RICE, J. R. (1972): "Constitutive analysis of elastic-plastic crystals at arbitrary strain," *Journal of the Mechanics and Physics of Solids*, **20**, 401-403.

HONNEFF, H., MECKING, H. (1978): "A method for the determination of the active slip systems and orientation changes during single crystal deformation," *Proceedings of ICOTOM 5*, Aachen, Springer-Verlag, **1**, 265-275.

HORSTEMEYER, M. F., MCDOWELL, D. L. (1998): "Modelling effects of dislocation substructure in polycrystal elastoviscoplasticity," *Mechanics of Materials*, **27**, 145-163.

HUTCHINSON, J. W., MILES, J. W. (1974): "Bifurcation analysis of the onset of necking in an elastic-plastic cylinder under uniaxial tension," *Journal of the Mechanics and Physics of Solids*, **22**, 61-77.

HUTCHINSON, J. W., NEALE, K. W., (1978a): "Sheet necking – II. Time-independent behaviour," Mechanics of Sheet Metal Forming, D.P. Koistinen and N.M. Wang, Editors, Plenum Press, 127-153.

HUTCHINSON, J. W., NEALE, K. W., (1978b): "Sheet necking – III. Strain-rate effects," Mechanics of Sheet Metal Forming, D.P. Koistinen and N.M. Wang Editors, Plenum Press, 269-285.

HUTCHINSON, J. W., NEALE, K. W. (1977): "Influence of strain-rate sensitivity on necking under uniaxial tension," *Acta Metallurgica*, **25**, 839-846.

HUTCHINSON, J. W., NEALE, K. W., NEEDLEMAN, A. (1978): "Sheet necking – I. Validity of plane stress assumptions of the long-wavelength approximation," Mechanics of Sheet Metal Forming, D.P. Koistinen and N.M. Wang Editors, Plenum Press, 111-126.

INAL, K., WU, P. D., NEALE, K. W. (2001a): "Instability and localized deformation in polycrystalline solids under plane strain tension," *International Journal of Solids and Structures*, (in press).

INAL, K., WU, P. D., NEALE, K. W. (2001b): "Finite element analysis of localized deformation in fcc polycrystals under plane stress tension," *International Journal of Solids and Structures*, (in press).

INAL, K., WU, P. D., NEALE, K. W. (2001c): "Large strain behaviour of aluminum sheets subjected to in-plane simple shear," (submitted to *Modelling and Simulation in Materials Science and Engineering*).

INAL, K., WU, P. D., NEALE, K. W. (2000a): "Simulation of earing in textured aluminium sheets," *International Journal of Plasticity*, **16**, 635-648.

INAL, K., WU, P. D., NEALE, K. W., MACEWEN, S. R. (2000b): "Numerical simulation of large deformation polycrystalline plasticity," Mathematical Modelling in Metal Processing and Manufacturing – COM2000, P. Martin, S. MacEwen, Y.Verreman, W.Lui, J. Goldak, Editors, Ottawa.

INAL, K. (1998) : "Modélisation numérique de l'aluminium à grandes déformations plastiques: applications au calcul parallèle," *M.A.Sc. Thesis*, Département de génie civil, Université de Sherbrooke, Sherbrooke, Québec, Canada.

KALIDINDI, S. R., BRONKHORST, C. A., ANAND, L. (1992): "Crystallographic texture evolution in bulk deformation processing of fcc metals," *Journal of the Mechanics and Physics of Solids*, **40**, 537-569.

KANETAKE, N., TOZAWA, Y. and OTANI, T. (1983): "Calculations from texture of earing in deep drawing for fcc metal sheets," *International Journal of Mechanical Sciences*, **25**, 337-345.

KEELER, S. P. (1961): "Plastic instability and fracture in sheets stretched over rigid punches," *Ph.D Thesis*, Massachusetts Institute of Technology, Cambridge, Massachusetts.

KOCHENDROFER, A. (1941): Plastiche Eigenschaften von Kristallen und Metallischen Werkstoffen, Springer, Berlin.

KOCKS, U. F. (1975): "Constitutive relations for slip," Constitutive Equations in Plasticity, A. S. Argon, Editor, MIT Press, 81-115.

KOKCS. U. F. (1970): "The relation between polycrystal deformation and single crystal deformation," *Metallurgical Transactions*, **1**, 1121-1143.

KOCKS, U. F., CANOVA, G. R. (1981): "How many slip systems and which?," Deformation of Polycrystals, N. Hansen et al., Editors, Riso National Laboratory, Roskilde, Denmark, 35.

KOCKS, U. F., STOUT, M. G., ROLLETT, A. D. (1988): "The influence of texture on strain hardening," Strength of Metals and Alloys, P. O. Kettunen, Editor, Pergamon Press, Oxford, 25-34.

KRÖNER, E. (1958): "Berechnung der elastischen konstanten des vielkristalls aus den konstanten des einkristalls," *Zeitschrift für Physik*, **151**, 504-518.

KUHLMANN-WILSDORF, D. (1989): "Theory of plastic deformation: properties of low energy dislocation structures," *Materials Science and Engineering*, **A113**, 1-41.

LEBENSOHN, R. A., TOMÉ, C. N. (1994): "A self-consistent visco-plastic model: prediction of rolling textures of anisotropic polycrystals," *Materials Science and Engineering*, **A175**, 71-82.

LEBENSOHN, R. A., TOMÉ, C. N. (1993): "A self-consistent anisotropic approach for the simulation of plastic deformation and texture development of polycrystals," *Acta Metallurgica et Materialia*, **41**, 2611-2624.

LEFFERS, T. (1992): "A model for rolling the deformation with the grains subdivided into cell blocks," *Proceedings of the 13th Riso International Symposium on Material Sciences*, 7.

LEGE, D. J., BARLAT, F., BAUDELET, B. (1989): "Characterization and modelling of the mechanical behaviour and formability of a 2008-T4 sheet sample," *International Journal of Mechanical Sciences*, **31**, 549-563.

LEGRESY, J. M., RAUCH, E. F., RICHARD, J. P. (1997): "Improvement of the scoring process for easy open ends: from the industrial issue to simple shear tests," *La Revue de Metallurgiecit*, **94**, 1509-1515.

MA, Q., CLARKE , D. R. (1995): "Size dependent hardness of solver single crystals," *Journal of Material Resistance*, **10**, 853-863.

MARCINIAK, Z., KUCZYNSKI, K., POKORA, T. (1973): "Influence of the plastic properties of a material on the forming limit diagram for sheet metal in tension," *International Journal of Mechanical Sciences*, **15**, 789-805.

MARCINIAK, Z., KUCZYNSKI, K. (1967): "Limit strains in processes of stretch-forming sheet metal," *International Journal of Mechanical Sciences*, **9**, 609-620.

MATHUR, K. K., DAWSON, P., KOCKS, U. F. (1990): "On modelling anisotropy in deformation processes involving textured polycrystals with distorted grain shape," *Mechanics of Materials*, **10**, 183-202.

MATHUR, K. K., DAWSON, P. (1989): "On modelling the development of crystallographic texture in bulk forming processes," *International Journal of Plasticity*, **5**, 69-94.

MCMEEKING, R. M. (1982): "The finite strain tension torsion test of a thin-walled tube of elastic-plastic material," *International Journal of Solids and Structures*, **18**, 199-204.

MINDLIN, R. D. (1965): "Second gradient of strain and surface tension in linear elasticity," *International Journal of Solids and Structures*, **1**, 417-438.

MINDLIN, R. D. (1964): "Micro-structure in linear elasticity," *Archives of Mechanical Analyses*, **16**, 51-78.

MINDLIN, R. D. (1963): "Influence of couple-stresses on stress concentrations," *Experimental Mechanics*, **3**, 1-7.

MOLINARI, A., CANOVA, G. R., AHZI, S. (1987): "A self-consistent approach of the large deformation polycrystal viscoplasticity," *Acta Metallurgica*, **35**, 2983-2994.

MUGHRABI, H. (1983): "Dislocation wall and cell structures and long range internal stresses in deformed metal crystals," *Acta Metallurgica et Materialia*, **31**, 1367-1379.

NEALE, K. W. (1981): "Phenomenological constitutive laws in finite plasticity," SM Archives, **6**, 79-127.

NEEDLEMAN, A. (1988): "Material rate dependence and mesh sensitivity in localization problems," *Computer Methods in Applied Mechanics and Engineering*, **67**, 69-85.

NEEDLEMAN, A. (1972): "A numerical study of necking in circular cylindrical bars," *Journal of the Mechanics and Physics of Solids*, **20**, 111-127.

NEEDLEMAN, A., TVERGAARD, V. (1992): "Analysis of plastic flow localization in metals," *ASME Applied Mechanics Review*, **45**, S3-S18.

NEEDLEMAN, A., TVERGAARD, V. (1984): "Finite element analysis of localization in plasticity," Finite Elements – Special Problems in Solid Mechanics, J. T. Oden and G.F. Carey, Editors, Prentice Hall, 94-157.

PEIRCE, D., ASARO, R. J., NEEDLEMAN, A. (1983): "Material rate dependence and localized deformation in crystalline solids," *Acta Metallurgica*, **31**, 1951-1976.

PEIRCE, D., ASARO, R. J., NEEDLEMAN, A. (1982): "An analysis of nonuniform and localized deformation in ductile single crystals," *Acta Metallurgica*, **30**, 1087-1119.

PEIRCE, D., ASARO, R. J. and NEEDLEMAN, A., 1981: "Elastic plastic constitutive laws for single crystals," *Brown University Report*, MRL E-130.

RAUCH, E. F., G'SELL, C. (1989): "Flow localization induced by a change in strain path in mild steel," *Materials Science and Engineering*, **A111**, 71-80.

RASHID, M. M., NEMAT-NASSER, S. (1990): "A constitutive algorithm for rate dependent crystal plasticity," *Computer Methods in Applied Mechanics and Engineering*, **94**, 201-228.

RICE, J. R. (1971): "Inelastic constitutive relations for solids: an internal-variable theory and its applications to metal plasticity," *Journal of the Mechanics and Physics of Solids*, **19**, 433-455.

SACHS, G. (1928): "Zur ableitung einer filebedingung," *Zeitschrift des Vereines Deutscher Ingenieure*, **72**, 734-736.

SARMA, G. B., DAWSON, P. (1996a): "Texture predictions using a polycrystal plasticity model incorporating neighbor interactions," *International Journal of Plasticity*, **12**, 1023-1054.

SARMA, G. B., DAWSON, P. (1996b): "Effects of interactions among crystals on the inhomogeneous deformation of polycrystals," *Acta Metallurgica et Materialia*, **44**, 1937-1953.

SAVOIE, J., JAIN, M., CARR, A.R., WU, P. D., NEALE, K.W., ZHOU, Y., JONAS, J. J. (1998): "Predictions of forming limit diagrams using crystal plasticity models," *Materials Science and Engineering*, **A257**, 128-133.

SCHMID, E. (1924): "Neuere Untersuchungen Metallkristallen," *Proceedings of the 1st International Congress of Applied Mechanics*, C. B. Biezeno and J. M. Burgers, Editors, Delft, The Netherlands, 342-353.

SHRIVASTAVA, S. C., JONAS, J. J., CANOVA, G. (1982): "Equivalent strain in large deformation torsion testing: theoretical and practical considerations," *Journal of the Mechanics and Physics of Solids*, **30**, 75-90.

SHU, J. Y., BARLOW, C. Y. (2000): "Strain gradient effects on microscopic strain field in a metal matrix composite," *International Journal of Plasticity*, **16**, 563-591.

SHU, J. Y., FLECK, N. A. (1998): "The prediction of a size effect in micro-indentation," *International Journal of Solids and Structures*, **35**, 1363-1385.

STELMASHENKO, N. A., WALLS, M. G., BROWN, L. M., MILMAN, Y. V. (1993): "Microindentations on W and Mo priented single crystals: an STM study," *Acta Metallurgica et Materialia*, **41**, 2855-2865.

STÖREN, S., RICE, J. R. (1975): "Localized necking in thin sheets," *Journal of the Mechanics and Physics of Solids*, **23**, 421-441.

TAYLOR, G. I. (1938): "Plastic strain in metals," *Journal of the Institute of Metals*, **62**, 307-324.

TAYLOR, G. I. (1934): "The mechanism of plastic deformation of crystals," *Proceedings of the Royal Society of London*, **A165**, 253-257.

TAYLOR, G. I., ELAM, C. F. (1923): "The distortion of an aluminium crystal during a tensile test," *Proceedings of the Royal Society of London*, **A102**, 643-661.

TOMÉ, C., CANOVA, G. R., KOCKS, U. F., CHRISTODOULOU, N., JONAS, J. J. (1984): "The relation between macroscopic and microscopic strain hardening in fcc polycrystals," *Acta Metallurgica*, **32**, 1637-1653.

TOTH, L. S., MOLINARI, A. (1994): "Tuning a self-consistent viscoplastic model by finite element results – II: application to torsion textures," *Acta Metallurgica et materialia*, **42**, 459-2476.

TOUPIN, R. A. (1962): "Elastic materials with couple stresses," *Archives of Mechanical Analyses*, **11**, 385-414.

TUCKER, G. E. G. (1961): "Texture and earing in deep drawing of aluminium," *Acta Metallurgica*, **9**, 275-286.

TUGCU, P. (1991): "Tensile instability in a round bar including the effect of material strain-rate sensitivity," *Computer Methods in Applied Mechanics and Engineering*, **93**, 335-351.

TUGCU, P., NEALE, K. W. (1988): "Analysis of neck propagation in polymeric fibres including the effects of viscoplasticity," *Journal of Engineering Materials and Technology ASME*, **110**, 395-400.

TVERGAARD, V., NEEDLEMAN, A., LO, K. K. (1981): "Flow localization in the plane strain tensile test," *Journal of the Mechanics and Physics of Solids*, **29**, 115-142.

VAN DER GIESSEN, E., NEEDLEMAN, A. (1995): "Discrete dislocation plasticity: a simple planar model," *Modelling and Simulation in Materials Science Engineering*, **3**, 689-735.

VAN DER GIESSEN, E., NEALE, K. W. (1993): "Analysis of the inverse swift effect using a rate-sensitive polycrystal model," *Computer Methods in Applied Mechanics and Engineering*, **103**, 291-313.

VOYIADJIS, G. Z., HUANG, W. (1996): "A modelling of single crystal plasticity with backstress evolution," *European Journal of Mechanics, A/Solids*, **15**, 553-573.

WU, P.D., INAL, K., NEALE, K.W., KENNY, L.D., JAIN, M. et MACEWEN, S.R. (2001) : "Large Strain Behaviour of Very Thin Aluminium Sheets Under Planar Simple Shear," *Journal de Physique IV*, **11**, 229-236.

WU, P. D., JAIN, M., SAVOIE, J., MACEWEN, S. R., TUGCU, P., NEALE, K. W. (2001): "Evaluation of anisotropic yield functions for aluminum sheets," *International Journal of Plasticity*, (in press).

WU, P. D., NEALE, K. W., VAN DER GIESSEN, E., JAIN, M., MAKINDE., MACEWEN, S. R. (1998): "Crystal plasticity forming limit diagram analysis of rolled aluminum sheet," *Metallurgical and Materials Transactions*, **29A**, 527-535.

WU, P. D., NEALE, K. W., VAN DER GIESSEN, E. (1997): "On crystal plasticity FLD analysis," *Proceedings of the Royal Society of London*, **453**, 1831-1848.

WU, P. D., NEALE, K. W., VAN DER GIESSEN, E. (1996): "Simulation of the behaviour of FCC polycrystals during reversed torsion," *International Journal of Plasticity*, **12**, 1199-1219.

WU, P. D., VAN DER GIESSEN, E. (1996): "Computational aspects of localized deformations in amorphous glassy polymers," *European Journal of Mechanics*, **A/Solids 15**, 799-823.

ZHOU, Y., NEALE, K. W. (1995): "Predictions of forming limit diagrams using a rate-sensitive crystal plasticity model," *International Journal of Mechanical Sciences*, **37**, 1-20.

ZHU, Z. G., BATRA, R. C. (1993): "Analysis of dynamic shear bands in an FCC single crystal," *International Journal of Plasticity*, **9**, 653-696.

ZIKRY, M. A., NEMAT-NASSER, S. (1990): "High strain-rate localization and failure of crystalline materials," *Mechanics of Materials*, **10**, 215-237.